Department of Physics and Astronomy
University of Heidelberg

Master Thesis in Physics
submitted by

Ralf Arne Klemt

born in Heidelberg

2016

Many-body correlations in a quasi-two-dimensional, ultracold atomic Fermi gas

This Master Thesis has been carried out by Ralf Arne Klemt at the
Physikalisches Institut Heidelberg
under the supervision of
Prof. Dr. Selim Jochim

Abstract

In this thesis, many-body correlations in a two-component ultracold atomic ^{6}Li Fermi gas are studied in a quasi-two-dimensional geometry. A general toolbox for the application of second order momentum space correlations, so-called noise correlations, is developed and applied to a gas both with and without an additional two-dimensional lattice trap. In particular, the implications of studying two-dimensional low density systems are discussed. Furthermore, fermionic many-body pair correlations are probed in the normal phase of the strongly interacting ^{6}Li gas by means of spatially resolved radio frequency spectroscopy. Pairing above the critical temperature for superfluidity in a many-body regime is observed.

Zusammenfassung

Diese Arbeit befasst sich mit Vielkörperkorrelationen in einem zweikomponentigen atomaren ^{6}Li Fermigas in einer quasi-zweidimensionalen Geometrie. Um Korrelationen zweiter Ordnung im Impulsraum, sogenannte Noise-Korrelationen, untersuchen zu können, wird eine allgemeine Auswertungsmethode entwickelt. Diese wird auf ein Gas sowohl mit als auch ohne ein zusätzliches zweidimensionales Gitterpotenzial angewendet. Ein Hauptaugenmerk wird auf Besonderheiten von zweidimensionalen Systemen mit niedriger Dichte gelegt. Zusätzlich werden Vielkörper-Paarkorrelationen von stark wechselwirkeden Fermionen bei Temperaturen oberhalb der kritischen Temperatur einer suprafüssigen Phase mit Hilfe von ortsaufgelöster Radiofrequenzspektroskopie untersucht. Hier kann Paarbildung in einem von Vielkörperphysik dominierten Regime gezeigt werden.

Contents

1 Introduction

A many-body quantum system is fully described by the complete set of all correlation functions up to infinite order [Pes95]. In a realistic experiment, it is of course completely impractical to measure all of them. Luckily, distinct systems are oftentimes characterised by a distinct pattern in (only) one of these orders.

In this thesis, we are concerned with (quasi-)two-dimensional and strongly correlated atomic Fermi gases. Here, in particular the direct and indirect observation of first order correlations marked by phase coherence leveraged the whole field of ultracold atomic gases with the first realisation of an atomic Bose-Einstein condensate [And95, Bra95, Dav95] and interference experiments with superfluid clouds [And97]. In a Bose-Einstein condensate, one single-particle state is macroscopically occupied and thus the system is described by a single macroscopic wave function showing phase coherence. Consequently, in momentum space, Bose-Einstein condensates manifest themselves by a strong peak at zero momentum and interference experiments show behaviour in terms of interference fringes similar to respective optical experiments with lasers [And97]. Most importantly, all the phenomena related to phase coherence can be lead back to single-particle coherence to be described by first order correlation functions.

There are, however, also important strongly correlated systems that can be (and in parts have been) realised with ultracold atomic gases, that cannot be described in terms of single-particle matter waves alone, as they show additional complex order and non-trivial correlations [Alt04]. As an example, consider a system of atoms localised in a lattice potential. For strong repulsive interactions, the transport of the atoms in the lattice is afflicted with an energy cost, such that the system becomes insulating. A transition from a Bose-Einstein condensate with (full) phase coherence into this so-called Mott insulator phase without any phase coherence has been realised for bosons in [Gre02]. These systems consequently have to be described by higher order correlations, especially if even more complexity in terms of the spin degree of freedom is introduced.

This thesis is concerned with two-component Fermi systems. More precisely, we focus on two important classes of systems that cannot be described only by phase coherence: The first class is given by fermions paired into many-body momentum space pairs, as given most famously by Cooper pairs. Only by a pairing mechanism, a Fermi gas of two different (pseudo-)spin components is allowed to condense into a superfluid, as the Pauli principle otherwise prohibits any macroscopic occupation of a single state. The single-particle momentum distribution, however, does not show any clear signature of the pairing, even if the paired system is condensed.

The other class comprises all systems with atoms localised in a lattice potential, as given for example by the Mott insulator. Despite being ordered, these systems do not show any phase coherence. In particular, for two-component fermionic systems even additional complex order can evolve by antiferromagnetic correlations, which are nevertheless not visible when studying only first order coherence.

The above considerations are of special importance in the case of two-dimensional (Fermi) gases as considered in our group. Two-dimensional atomic systems are of major interest for both fundamental and, as their low-temperature behaviour might be linked to the physics of unconventional high-temperature superconductivity [Blo12], also technological reasons: Two dimensions are considered marginal [Lev15] in the sense that quantum fluctuations destroy any long range order (in the first order correlation function) for any finite temperature, but nevertheless some notion of quasi-long range order, induced by interactions, persists [Ber72, Kos73]. Those systems are especially hard to treat theoretically, as perturbative treatments are bound to fail in the strongly correlated regime. Thus, insight may be provided by experimentally realising the Hamiltonians of interest, and therefore realising analogue quantum simulations [Blo12]. Experimentally, it is possible to tune the interaction strength in a broad range and also reach the limit of strongly correlated Fermi gases. They may provide insight into the highly complex and, as of now, not fully understood high-temperature superconductivity of layered cuprate structures with again strong correlations among the electrons [Nor11, Lev15].

The emergence of a superfluid phase has already been shown for a broad range of interactions in a bulk gas, where the fermions pair up in either many-body Cooper-type pairs or two-body dimers and then condense [Rie15a]. But not only the superfluid phase is of interest. High-temperature superconductors show fermionic many-body pairing already in the normal phase, referred to as the pseudogap region. This in stark contrast to conventional superconductors, where pairing and superfluidity happen at the same temperature, and is up to now not well understood. A similar pseudogap region might exist in a strongly interacting atomic Fermi gas as well and could be studied there. By including a lattice system, more complex pairing mechanisms (most importantly d-wave pairing) might be experimentally realisable in addition to ordered Mott insulator phases. In the latter system, very low-entropy Fermi gases in a lattice are expected to show complex (antiferromagnetic) order.

Indeed, all these strongly correlated systems of interest have in common that the single-particle momentum distribution shows no distinct features characterising the complex correlations, such that other signatures have to be found. For the superfluidity of a strongly interacting Fermi gas, (some) phase coherence is present; however, not in the single-particle, but in the paired states. Here, the pair momentum distribution can be considered instead of the single-particle one [Rie15a, Mur15b]. Systems completely without any phase coherence, especially when studying the emergence of pairing in the normal phase and characterising a Mott insulator state, (in the fermionic limit possibly even with antiferromagnetic complex order,) defy such a description. Here, other methods have to be found.

In this thesis, two important of these methods to detect many-body higher order correlations are studied with their respective application:

One of the methods is based on radio frequency spectroscopy, a well-established method to probe single-particle energy shifts, and in particular binding energies. Here, the difference between single-particle energy states is probed, and therefore the existence of pairing in addition to the pairing energy gap may be studied. In this thesis, the method will be used to probe the existence of fermionic (s-wave) pairing in the normal phase of a strongly interacting Fermi gas.

Radio frequency spectroscopy is, however, insensitive to the exact type of pairing. In particular, it might be interesting to directly distinguish two-body dimers from many-body Cooper-type pairs. Furthermore, more complex pairing mechanisms, as for example d-wave pairing, have to be identified on the route to understanding high-temperature superconductors. In addition, systems with (complex) order, as given for example by the bosonic and especially the fermionic Mott insulator, possibly with some antiferromagnetic correlations, cannot be probed directly by radio frequency spectroscopy.

All these examples are characterised by atom-atom, or more in general density-density, correlations. Therefore it seems natural to consider second order correlation functions. Here, instead of directly probing the momenta, the fluctuations in the momentum distribution are studied. Consequently, these types of correlations are also called noise correlations. While similar correlations have been known from optics and nuclear physics for roughly 60 years, where the so-called Hanbury Brown and Twiss correlations lead for example to photon bunching [Bro56b], the application to atomic systems is still relatively new [Alt04]. Nevertheless, noise correlations have already found several applications, for example in showing bosonic bunching and fermionic anti-bunching [Jel07] as well as characterising a bosonic Mott insulator in three dimensions [Föl05].

In this thesis, the application of noise correlation methods on two-dimensional systems are discussed, where additional hurdles have to be overcome. In addition to studying systems already realised in our group, (which are in particular thermal gases with and without an additional lattice potential), a general toolbox for noise correlation experiments will be developed, which allows to probe and characterise also more complex strongly correlated Fermi systems in the future.

Outline

The thesis is structured as follows: Chapter 2 covers the most important theoretical results needed for understanding the preparation as well as the analysis of strongly correlated two-dimensional atomic Fermi systems. Thereafter the basic principles of the noise correlation analysis method are presented in chapter 3.

Chapter 4 gives an overview over the experimental set-up and procedures. Of special importance for both the noise correlation measurements and the pairing measurements with radio frequency spectroscopy is a detailed imaging and noise characterisation which will be presented in chapter 5. Chapter 6 is dedicated to noise correlation measurements. In addition to a detailed overview over the general procedure, the applications to a two-dimensional bulk as well as lattice system are discussed. Because the correlation method turns out to be not in general suited for the analysis of two-dimensional atomic clouds with low densities, in particular also limitations of a noise correlation experiments are discussed. Apart from noise correlations measurements, also a radio frequency spectroscopy analysis is conducted to probe pairing in the normal phase of a strongly interacting Fermi gas. First results from the ongoing analysis are presented in chapter 7. Finally, chapter 8 gives a summary and conclusion of the methods and results presented in this thesis, and in addition provides an outlook to possible or already planned further steps towards understanding strongly correlated two-dimensional Fermi gases.

2 Theory

This chapter briefly reviews the main theoretical results needed for understanding the preparation and analysis of strongly correlated Fermi systems in a quasi-two-dimensional geometry in the vicinity of a so-called broad Feshbach resonance.

The general features and implications of ultracold quantum gases are presented in section 2.1, where the properties of bosons and fermions at extremely low temperatures are investigated. This includes in particular low energy interactions and methods to tune them, as well as the emergence of a condensed phase. A special focus is put on the influence of dimensionality and the notion of a quasi-two-dimensional quantum system is introduced.

As it is possible in an ultracold quantum gas of ^{6}Li to smoothly change its character between an effectively fermionic and a bosonic ensemble, an appropriate theoretical model by means of the so-called BEC-BCS crossover is introduced and motivated in section 2.2. In this context the concept of the pseudogap is introduced as well.

Parts of the experiments described in this thesis are performed in a lattice geometry. The periodic structure of a lattice has important implications due to the discrete translation symmetry introduced. Therefore, the final section 2.3 is dedicated to the basic properties of particles in periodic potentials. Here, the important Hubbard model is introduced, which despite its relatively simplistic nature, shows highly non-trivial low-temperature phases.

2.1 Ultracold quantum gases

In a many-body system, the quantum regime is entered as soon as the de Broglie wavelength of the particles, given by $\lambda_{dB} = h/p$, where h is Planck's constant and p the momentum of the particle, reaches the order of the inter-particle spacing. While in a typical many-body system in condensed matter, the electron density is high and the system shows quantum behaviour up to relatively high or even room temperatures, atomic systems, as considered here, are much more dilute, and therefore require ultracold temperatures around 100 nK. This sections is concerned with general properties of ultracold quantum gases such as their scattering as well as condensation behaviour, with a special focus on two-dimensional systems explored in our group.

2.1.1 Quantum statistics

Identical particles in the quantum regime, i.e. particles with a significant wave function overlap, are indistinguishable, meaning that

$$|P_{\mu\nu}\Psi|^2 = |\Psi|^2, \tag{2.1}$$

where Ψ is the full many-body wave function and $P_{\mu\nu}$ an operator exchanging two identical particles labelled by μ and ν. Since $P^2 = \mathbb{1}$ is required to hold, all particles may be categorised according to the two possible eigenvalue classes corresponding to the eigenvalues (chosen without loss of generality to be real) ±1 with respect to the exchange operator [Sak11][1].

Fermions Fermions are the antisymmetric subclass with $P_{\mu\nu}\Psi = -\Psi$ and carry half-integer spin. The antisymmetry requirement has the consequence that no state can be occupied by more than one particle. This is known as the Pauli principle. The occupation of states with energy E is given for a fermionic system by the Fermi-Dirac distribution:

$$f^F(E) = \frac{1}{e^{\frac{E-\mu}{k_B T}} + 1} \tag{2.2}$$

Here, T denotes the temperature, μ the chemical potential and k_B the Boltzmann constant. For $T \to 0$ the distribution function approaches a step function and the particles populate - according to the Pauli principle - all available states up to the so-called Fermi energy E_F exactly once. For a homogeneous non-interacting system in two dimensions with density n, the Fermi energy can be evaluated to be

$$E_F = \frac{\hbar^2}{2m}(4\pi n). \tag{2.3}$$

In this limit, the Fermi energy corresponds to the chemical potential $E_F = \mu(T = 0)$. Even though the clear interpretation of the Fermi temperature in terms of the maximum occupied energy in the system is only valid in the zero-temperature and non-interacting limit, it still always gives a typical energy scale of the system. In a similar fashion, also the Fermi temperature $T_F = E_F/k_B$ and the Fermi wave vector $k_F = \sqrt{2mE_F}/\hbar$ are defined. It is important to stress that the Fermi-Dirac distribution, and equivalently also the Pauli principle, prohibits any macroscopic occupation of the ground state.

---

[1] This ignores one subtlety arising in two dimensions (or for massless particles), where in addition so-called anyons may exist. For details see for example [Wil90].

Bosons Bosons are the symmetric subclass with $P_{\mu\nu}\Psi = \Psi$ and carry integer spin. For bosons, a restriction of occupation numbers in analogy to the Pauli principle does not exist and in general the single-particle occupation of states with energy E is given by the Bose-Einstein distribution:

$$f^B(E) = \frac{1}{e^{\frac{E-\mu}{k_B T}} - 1} \tag{2.4}$$

The total number of particles for non-interacting bosons is thus given by

$$N(\mu) = \sum_{\alpha} f^B(E_\alpha), \tag{2.5}$$

where α indexes the different energy eigenstates with energy E_α, where without loss of generality $E_\alpha \geq 0$ and for the ground state $E_0 = 0$ was assumed. When lowering the temperature, the total weight of the distribution function decreases, which has to be counterbalanced by an increasing chemical potential, acting as a Lagrange multiplier here, in order to remain at a fixed particle number. Note however, that the chemical potential in equation 2.4 is restricted from above to zero for the Bose-Einstein distribution in order to be well-defined. Therefore, below a critical temperature T_C even $\mu = 0$ does not suffice to keep the distribution function for $\alpha > 0$ large enough to accommodate all particles such that the remaining particles macroscopically occupy the ground state [Alt10]. This phenomenon is called Bose-Einstein condensation and was directly observed first in a dilute gas of alkali atoms in 1995, leading to the nobel price for Cornell, Ketterle and Wieman in 2001 [Nob]. While the dimensionality of the system was not directly accounted for in the simple heueristic arguments above, one obtains for a homogeneous (non-interacting) system in three dimensions a finite T_C, while for the same system in two dimensions Bose-Einstein condensation is only possible at zero temperature as is shown in detail for example in [Pet02].
Condensation and corresponding mechanisms in two dimensions will be discussed in more detail in subsection 2.1.5.

2.1.2 Interactions

In this section, interactions in a dilute cold gas are introduced. The considerations are based, unless stated otherwise, on [Sch13].
In order to describe the elastic scattering process in a cloud of ^{6}Li atoms in full detail, the exact form of the scattering potential V_{int} has to be known. For a spherical symmetric potential and sufficiently low density[2], such that only two-body scattering has to be

---

[2] More precisely, in addition also no resonantly enhanced three- or many-body scattering process is allowed.

taken into account, the process is described in the centre of mass frame by the (time-independent) Schrödinger equation

$$\left[\frac{p^2}{2m_r} + V_{int}(r)\right]\Psi(r) = E\Psi(r) \tag{2.6}$$

with the reduced mass m_r of the scatterers. Even for the relatively easy case of an alkali-metal like ^{6}Li , a full solution of the scattering problem is neither possible nor needed; especially in the context of ultracold gases. As illustrated below, the scattering potential may be well accounted for by a single parameter and equivalently by replacing the full scattering potential by an effectively zero range pseudo-potential. This simple form of the interactions is one of the key aspects in favour of using ultracold atoms for the purpose of realising fundamental theoretical models.

Low energy scattering in a 3D geometry Equation 2.6 may be solved for asymptotically large radii and elastic scattering by the superposition of an incoming plain wave and a scattered spherical wave,[3]

$$\Psi_{\vec{k}}(\vec{x}) = e^{ikz} + \frac{e^{ikr}}{r} f_{\vec{k}}(\theta), \tag{2.7}$$

where the wave vector of the incoming wave with modulus k defines the z-direction and the angle θ is defined with respect to the wave vector. The scattering amplitude $f_{\vec{k}}(\theta)$ depends on the details of the potential and determines the (differential) cross section in terms of the solid angle Ω via [Sak11]

$$\frac{d\sigma}{d\Omega} = \begin{cases} |f_k(\theta)|^2 & \text{for distinguishable particles} \\ |f_k(\theta) - f_k(\theta+\pi)|^2 & \text{for identical fermions} \\ |f_k(\theta) + f_k(\theta+\pi)|^2 & \text{for identical bosons.} \end{cases} \tag{2.8}$$

The spherical symmetric potential allows for an expansion in partial waves, that is Legendre polynomials P_l, such that the scattering amplitude is asymptotically given by

$$f_k(\theta) = \frac{1}{k}\sum_{l=0}^{\infty}(2l+1)e^{i\delta_l}\sin\delta_l P_l(\cos\theta), \tag{2.9}$$

where each partial wave merely acquires a phase shift δ_l in the scattering process. For very low energy scattering, only a few terms in this sum contribute, since the centrifugal barrier hinders the wave function to enter the effective range of the potential. In the

---

[3] In the following we will always assume a reasonably continuous potential that falls off to zero faster than a Coulomb potential [Sch13].

limit of ultracold gases, it is sufficient to assume only s-wave, i.e. l=0, scattering. This results in [Blo08]

$$f(k) = \frac{1}{\cot \delta_0(k) - ik}. \tag{2.10}$$

An important consequence is that in the limit of only s-wave scattering contributing, identical ultracold fermions are effectively non-interacting, as $\frac{d\sigma}{d\Omega} = 0$.
The scattering length a is defined as the limit $f(k \to 0) = -a$, such that up to order k^2 the scattering amplitude is given by

$$f(k) = -\frac{1}{a^{-1} - k^2 R^*/2 + ik}, \tag{2.11}$$

with the effective range of the scattering potential given by R^*. This simplifies even further to

$$f(k) = -\frac{1}{a^{-1} + ik} \tag{2.12}$$

in the limit of $|R^*|k \ll 1$, which is well fulfilled for ^{6}Li and typical experimental parameters, where there are two important limits for

$$f = \begin{cases} -a & \text{for } k|a| \ll 1 \qquad \text{(weakly interacting regime)} \\ \frac{i}{k} & \text{for } k|a| \gg 1 \qquad \text{(unitary regime).} \end{cases} \tag{2.13}$$

If the range of the potential is not resolved, it may be furthermore replaced by a zero-range pseudo potential

$$V_{eff}(r) = g\tilde{\delta}(r), \tag{2.14}$$

where the coupling strength is proportional to the scattering length and $\tilde{\delta}(r) = \delta(r)\frac{\delta}{\delta r}r$ denotes a renormalised delta function [Gio08]. On a mean field level for a homogeneous density n, the interaction energy is given by

$$E_{int}(a) = gn = \frac{4\pi\hbar^2 n}{m}a, \tag{2.15}$$

such that $a > 0$ leads to repulsive mean field interactions while $a < 0$ corresponds to attractive ones.
In three dimensions, s-wave interactions support a dimer bound state for any positive scattering length with a binding energy of [Gio08]

$$E_B = \frac{\hbar^2}{2m_r a^2}. \tag{2.16}$$

According to equation 2.16, the binding energy becomes large for a small scattering length a. As a consequence, the typical size of the molecules decreases until it is finally too small to be resolved by the typical momenta of the system (this is in the limit of $E_B \ll E_F$). In this limit, the dimers may be described by effective point-like bosons with an atom-dimer scattering length of $a_{ad} \approx 1.18a$ [Gio08] and a dimer-dimer scattering length of $a_{dd} \approx 0.6a$ [Pet04].

Low energy scattering in a 2D geometry Scattering in two dimensions may be described in a similar fashion as in 3D [Lev15]. In a partial wave expansion, the scattering amplitudes

$$f_l(k) = \frac{-4}{\cot \delta_l(k) - i} \tag{2.17}$$

are obtained with the differential cross section (for distinguishable particles) now given by

$$\frac{d\sigma}{d\theta} = \frac{|f(k)|^2}{8\pi k}. \tag{2.18}$$

Considering again only the s-wave channel and low energy scattering, the phase shift can be simplified to be

$$\cot \delta_0(k) = -\frac{2}{\pi} \ln(1/ka_{2D}) + \mathcal{O}(k^2) \tag{2.19}$$

with a positive 2D scattering length a_{2D}. With the typical momentum scale k_F for a Fermi gas, the above formula suggests the dimensionless parameter $\ln(k_F a_{2D})$ as the relevant interaction parameter. In an intuitive picture, the interaction parameter gives the (logarithm of the) ratio between scattering length and inter-particle spacing given by $\frac{\sqrt{4\pi}}{k_F}$.

As before, s-wave scattering supports two-body bound states now for all values of a_{2D} with the energy [Lev15]

$$E_B = \frac{\hbar^2}{2m_r a_{2D}^2}. \tag{2.20}$$

Low energy scattering in quasi-2D geometry In our group we are interested in exploring the physics of two-dimensional systems. However, the space we live in is of course three-dimensional, and thus the notion of a 2D space is in principle of pure theoretical nature. Nevertheless, it is possible to reduce the density of states to an effective 2D one by introducing a strong confinement in one of the spatial dimensions. If all energy scales are (much) smaller than the first excitation level in this direction, only the ground state is populated and the motion of the particles restricted to two dimensions. Still, the range of the interaction parameter is typically smaller than the confinement length scale (e.g. the harmonic oscillator length $l_z = \sqrt{\hbar/(m\omega)}$) such that the scattering process is strongly influenced by the third dimension. This can be accounted for by an effective re-normalisation of scattering length and dimer binding energy [Lev15]. Keeping this in mind, it is therefore possible to explore effective two-dimensional systems, referred to here as quasi-2D[4].

While the interaction parameter in quasi-2D is still given by $\ln(k_F a_{2D})$, both the scattering length and the bound state energy are given in terms of 3D parameters via [Lev15]

$$a_{2D} = l_z \sqrt{\frac{\pi}{A}} e^{-\sqrt{\frac{\pi}{2}\frac{l_z}{a}}}, \tag{2.21}$$

with $A \approx 0.905$, $l_z = \sqrt{\hbar/m\omega_z}$ the harmonic oscillator length and a the 3D scattering length and

$$\frac{l_z}{a} = \int_0^\infty \frac{du}{\sqrt{4\pi u^3}} \left(1 - \frac{e^{\frac{-E_B}{\hbar\omega_z}u}}{\sqrt{\frac{1}{2u}\left(1 - e^{-2u}\right)}} \right). \tag{2.22}$$

The binding energy in the quasi-2D case is displayed in figure 2.1 in comparison with the 3D and 2D case. As opposed to the three-dimensional case, in two dimensions a bound state exists for all interaction strengths. For a negative 3D scattering length, the bound state may therefore be considered to be confinement-induced, resulting from an effective upward shift of the continuum by the ground state energy $0.5\hbar\omega_z$ of the third dimension. In the limit of large binding energies, corresponding to a scattering length much smaller than the z-confinement, the size of the dimer is much smaller than l_z and thus approaches the 3D value. In the other limit of a dimer size large compared to the confinement, the (small) binding energy correspondingly agrees with the 2D value.

2.1.3 Feshbach resonances

In order to reach a regime where, despite the diluteness of the gas, the system can be considered strongly interacting, the scattering length has to be resonantly enhanced. This can be achieved by means of a Feshbach resonance. In general, a Feshbach resonance results from the residual coupling of a bound state in a closed scattering channel (that is, its continuum energy is larger than the energy of the incoming particles) with the open (actual) scattering channel. In case of the virtual bound state energy close to the

---

[4] This nomenclature is not unique within the literature. Sometimes, quasi-2D refers to a system where not only the ground state, but a few discrete energy levels in the strongly confined direction can be populated.

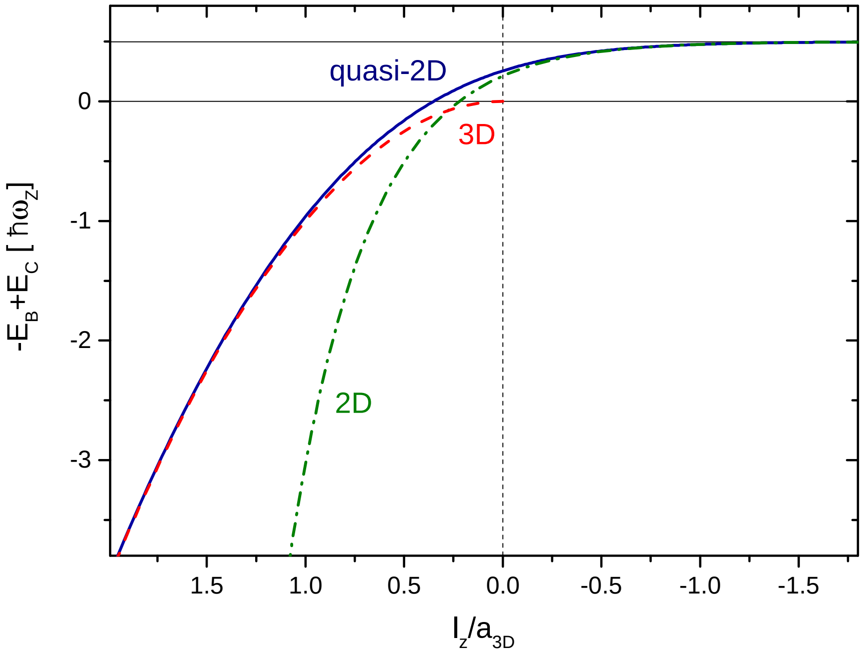

Figure 2.1: Binding energy of the two-body dimer in a 2D, quasi-2D and 3D geometry as a function of the inverse (3D) scattering length scaled by the vertical confinement. While the 3D dimer becomes unbound above the resonance at $l_z/a_{3D} = 0$, 2D dimers stay bound for all interactions due to a confinement-induced shift of the continuum by $0.5\hbar\omega_z$. For better comparability, the continuum shift is added to both the 2D and the quasi-2D binding energies in the plot. In the limit of large binding energy, and thus small dimer sizes, the quasi-2D energy approaches the 3D energy, while in the opposite limit, when the dimer size is much larger than the confinement scale, the binding energy is effectively given by the 2D formula.

continuum of the open channel, an additional diverging phase factor is acquired and thus the scattering length resonantly enhanced [Blo08]. The situation is depicted in a simple two-channel model in figure 2.2. Atoms scatter (predominantly) in a fixed spin configuration with a corresponding interaction potential sketched in black in figure 2.2. For concreteness, let this be a triplet state. The asymptotic energy at large distances r of the other spin configuration (in this case the singlet sketched in red) is larger than the initial energy of the incoming particles, such that it can be populated only virtually in an elastic scattering process. Since for a large but finite magnetic field, there is always a small admixture of the singlet state in the open channel, there is residual coupling at short distances between the open and the closed channel. If there is now a virtual bound

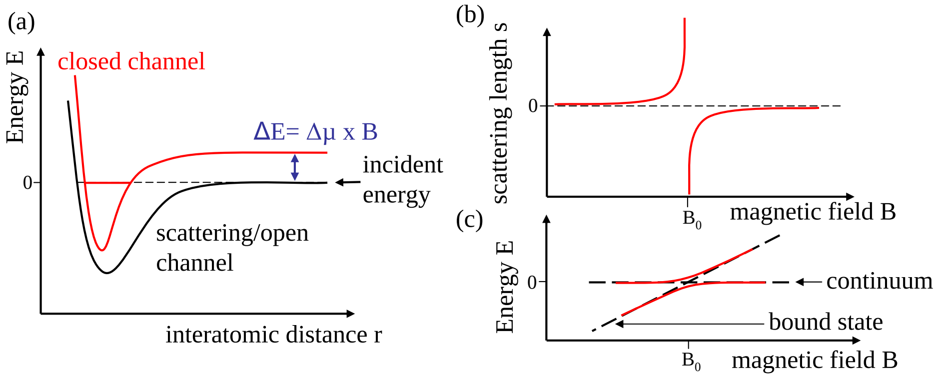

Figure 2.2: (a) Sketch of the potentials of open (black) and closed (red) channel as a function of the inter-atomic distance. While the asymptotic energy of the closed channel is too large to be populated permanently, the relative energies may be tuned, such that a bound state energy of the closed channel is close to the incident energy. Residual coupling between the two channels then leads to a resonantly enhanced scattering length. (b) Resulting scattering length as a function of the magnetic field as described by equation 2.23. (c) Energy levels of bound and continuum states. The residual coupling leads to an avoided crossing. Taken from [Wen13].

state at a nearly degenerate energy, this resonantly enhances the scattering amplitude. Furthermore, the open and the closed channel have different magnetic moments, such that the relative energy of the channels may be shifted by varying the magnetic offset field, thus controlling the scattering length. Phenomenologically the dependence of the scattering length on the magnetic field may be modelled to be [Gio08]

$$a(B) = a_{bg}\left[1 - \frac{\Delta_B}{B - B_0}\right], \tag{2.23}$$

with the background scattering length a_{bg}, the width of the resonance Δ_B and its position B_0. Of special interest in experiments are the so-called broad Feshbach resonances, where the assumption of a negligible effective range of interactions used above in describing the scattering process holds and furthermore Δ_B is large, such that small fluctuations in the offset magnetic field do not have a too strong influence on the scattering length.

2.1.4 ^{6}Li

In our experiments, the fermionic isotope of lithium, ^{6}Li , is used. It is an alkali atom with an electronic spin of $S = 1/2$ and a nuclear spin of $I = 0$. For the relatively high magnetic fields of 600 G to 1400 G used in the experiments, electronic and nuclear spins mostly decouple. The different Zeeman states are therefore characterised by the magnetic quantum numbers of nuclear and electronic spins. The projection of the total spin on the z-axis m_f remains a good quantum number for all fields and can be used to label the different hyperfine states as illustrated in figure 2.3a. The high field seeking states

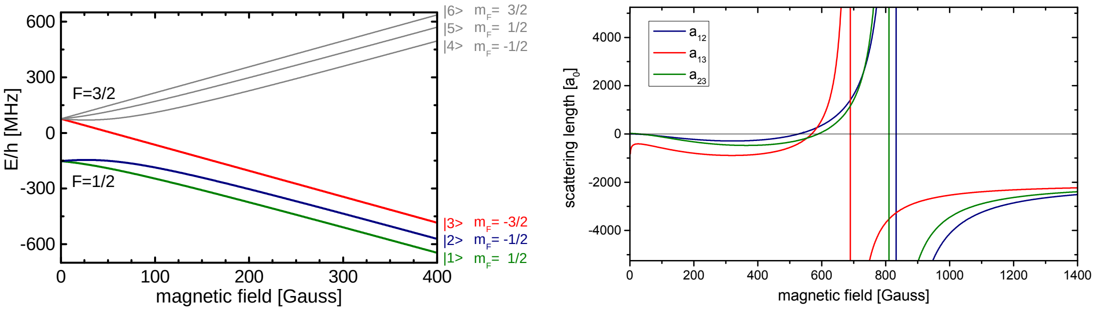

(a) Hyperfine manifold

(b) Feshbach resonances

Figure 2.3: (a) Hyperfine manifold of the ^{6}Li $2^2\mathrm{S}_{1/2}$ electronic ground state as a function of the magnetic offset field. Experiments are performed at high magnetic fields ($\gtrsim 600\,\mathrm{G}$) where nuclear and electronic spin mostly decouple. Experimentally accessible are the three high field seeking states with $m_s = -1/2$. Taken from [Wen13]. (b) Scattering lengths in units of the Bohr radius as a function of the magnetic offset field for the three possible mixtures of two hyperfine states. Used in this thesis are the $|1\rangle - |2\rangle$ mixture with a resonance at 832.2 G and the $|1\rangle - |3\rangle$ mixture with a resonance at 689.7 G. The Feshbach resonances where characterised in [Zür13]. Taken from [Zür12].

$|1\rangle - |3\rangle$ are collisionally stable and thus experimentally available. The states have an energy difference of around $h{\cdot}80\,\mathrm{MHz}$ and may be coupled to each other by radio frequency (RF) pulses. In order to have an interacting Fermi gas, at least two different states are needed. For most of the experiments, a balanced mixture of either state $|1\rangle$ and $|2\rangle$ or state $|1\rangle$ and $|3\rangle$ is used. All measurements are performed in the vicinity of the broad Feshbach resonances at 832.2 G and 689.7 G for the $|1\rangle - |2\rangle$ and the $|1\rangle - |3\rangle$ mixture, respectively. The magnetic field dependence of the scattering length is plotted in figure 2.3b.
A two-component gas of ^{6}Li is stable towards three-body losses for sufficiently large scattering lengths. Therefore it is possible to perform experiments in a range of approximately $|a| \gtrsim 2000 a_0$.

2.1.5 Condensation

Two-dimensional systems are oftentimes referred to show 'marginal' behaviour in the sense that although ordered phases are more robust in higher dimensions and quantum fluctuations play a much more pronounced role in 2D, nevertheless some sort of quasi-long range order is possible [Had09, Lev15]. In this section, the possibility and mechanism of superfluidity in a two-dimensional Bose gas are briefly discussed. For a more in-depth discussion, the reader is referred to the literature; for a comprehensive review see for example [Had09], which this section is mostly based on.

A Bose-Einstein condensate (BEC) in three dimensions (and a homogeneous system) is characterised by long range order (LRO), meaning that the system shows finite coherence for arbitrary large distances within the system. This may be quantified by the first order correlation function g_1

$$g_1(\vec{r}) = \frac{1}{n} \langle \hat{\Psi}^\dagger(\vec{r})\hat{\Psi}(0)\rangle \,, \tag{2.24}$$

where $\hat{\Psi}^\dagger(\vec{r})$ ($\hat{\Psi}(\vec{r})$) denotes the creation (annihilation) operator of a particle at position r, and n is the particle density. A phase transition into long range order corresponds to a spontaneously broken symmetry of the Hamiltonian. For the BEC, this is the phase ϕ of $\hat{\Psi}$ which is arbitrarily chosen such that $\hat{\Psi} = \sqrt{n}e^{i\phi}$[5]. Correspondingly, the g_1-function takes the form

$$g_1(\vec{r}) = 1, \tag{2.25}$$

indicating that the phase is constant throughout the condensate. In two dimensions and a non-interacting system, fluctuations destroy phase coherence beyond the thermal de Broglie wavelength λ_{dB}. As a consequence, first order coherence in a 2D gas in its normal phase decays even in the degenerate limit at least exponentially (for larger r) in the form [Had09]

$$g_1(r) \approx e^{-r/l}, \tag{2.26}$$

where l is directly related to the thermal de Broglie wavelength[6]. This absence of long range order can be calculated directly using the 2D density of state, or may be concluded on more general grounds from the famous Mermin-Wagner theorem, stating that in one or two dimensions LRO at finite temperature is not possible for a system with short range interactions and a Hamiltonian showing a continuous symmetry in the thermodynamic limit [Mer66]. Note that for a finite system and a finite coherence length, the system might still be fully ordered if the coherence length is larger than the system size. On the other hand, introducing (repulsive) interactions introduces another length scale given by the healing length $\xi = \frac{\hbar}{\sqrt{mgn}}$ in terms of the interaction strength g and the density n. Since the interaction energy may be minimised by minimising density fluctuations, for

---

[5] The operator $\hat{\Psi}$ is in this case a classical $\mathbb{C}$ field

[6] In a thermal non degenerate gas g_1 would even decay with a gaussian of with $\lambda/\sqrt{\pi}$. This still describes the short distance behaviour in a degenerate gas

length scales larger than the healing length density fluctuations are strongly suppressed as soon as the interaction energy is on the same order as the thermal energy.
Despite the absence of true long range order, and correspondingly a phase transition caused by spontaneous symmetry breaking, in two dimensions a topological phase transition as described for example by the Berezinskii-Kosterlitz-Thouless (BKT) mechanism leading to algebraically decaying correlations is still possible [Ber72, Kos73]. This is referred to as quasi-long range order and is described by a g_1-function of the form

$$g_1(r) = r^{-\eta}, \tag{2.27}$$

with $\eta = \frac{1}{4}$ for a homogeneous system.
For small temperatures, density fluctuations are already strongly suppressed as stated above. Thus, in a simple heueristic model, a superfluid wave function of the form

$$\Psi_s(\vec{r}) = |\Psi_s(\vec{r})|\, e^{i\phi(\vec{r})} = \sqrt{n_s} e^{i\phi(\vec{r})}, \tag{2.28}$$

with n_s being the superfluid density, may be constructed [Had09]. In this approximation, all interactions can only affect the phase. These are first of all low energy phononic excitations corresponding to a smooth variation of the phase, and secondly vortex excitations corresponding to a phase circulation of 2π in either positive or negative sense of rotation around a zero density vortex core. The latter excitation is possible due to the phase being single valued. Note that the vortex is of the size of the healing length, such that the density fluctuations take place at length scales $r < \xi$. Assuming only smooth phase fluctuations, an effective Hamiltonian of the form

$$H_\theta = \frac{\hbar^2}{2m} n_s \int d^2r (\nabla\theta)^2 \tag{2.29}$$

may be used for describing the system[7] and the g_1-function $g_1(r) = \frac{1}{n_s} \langle \hat{\Psi}^\dagger(\vec{r})\hat{\Psi}(\vec{0})\rangle = \langle e^{i\left(\theta(\vec{r})-\theta(\vec{0})\right)}\rangle$ can be calculated to be [Had09]

$$g_1(r) = \left(\frac{r}{\xi}\right)^{-1/(n_s\lambda_{dB}^2)}, \tag{2.30}$$

thus showing quasi-long range order (QLRO) in the form of algebraically decaying correlations. Correspondingly, the BKT transition is driven by vortex excitations. This may be seen from noting that the free energy needed to create a vortex excitation changes sign at $n_s\lambda = 4$ [Had09]. As a consequence, for large phase space densities, vortex excitations cost energy and vortices of different circulation $\pm\pi$ pair up, suppressing phase fluctuations for length scales larger than their pairsize of order ξ. On the other hand, for

---

[7] Vortices may be re-introduced by considering a UV cutoff at small distances naturally given by the healing length.

small phase space densities, the system minimises its energy by creating free vorticies, 'scrambling' the phase.
Due to the topological nature of vortices, the BKT transition is an example of a topological phase transition and thus not prohibited in 2D by the Memin-Wagner theorem. More quantitative expectations for the BKT transition temperature T_C may be obtained from quantum Monte Carlo (QMC) calculations. Furthermore, it is important to note that both in a trap and for a finite system, true long range order is possible for finite temperatures, however at lower temperature scales than the BKT transition. The existence of a BKT-type transition into QLRO was experimentally shown for a strongly interacting 2D gas in our group in previous works [Mur15b] and the main results are shown in figure 2.4. Furthermore, the BKT mechanism can explain in a similar fashion

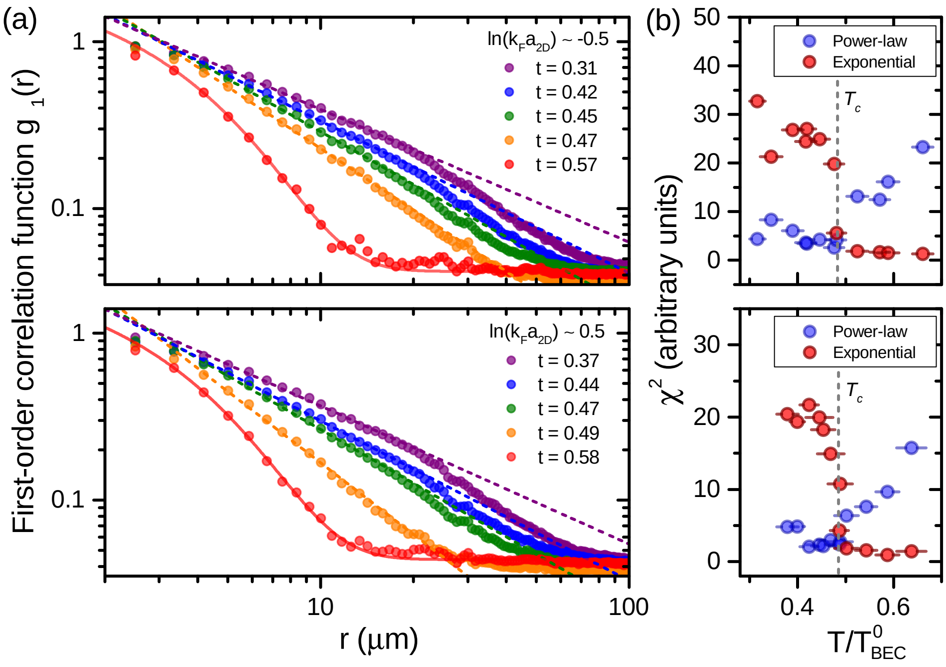

Figure 2.4: Observation of the BKT transition into a superfluid phase in a strongly interacting 2D Fermi gas. Shown in (a) is the first order correlation function obtained from a Fourier transform of the momentum space distribution for different temperatures and different interaction strengths. For low enough temperature, the g_1-function changes character from an exponential to an algebraically decaying function. To obtain the transition temperature, both functions are fitted to the data and the likelihood of the fit is recorded in form of the χ^2-value in (b). Taken from [Mur15b].

as described above a normal to superfluid phase transition in a fermionic system which involves (similar to the 3D case), 'Cooper' many-body pairing [Mur15b].

2.2 BEC-BCS crossover

In this section, the concept of the BEC-BCS crossover smoothly linking the limits of a molecular Bose-Einstein condensate and an atomic Bardeen-Cooper-Schrieffer (BCS) phase will be introduced. While it is strictly speaking limited in application to three-dimensional systems, a similar crossover exists also in 2D, as will be illustrated below in subsection 2.2.2.

2.2.1 The 3D BEC-BCS crossover

The broad Feshbach resonances of ^{6}Li allow for tuning the scattering length over a wide range, and thus accessing both the regime of weakly attractive fermions and the regime of deeply bound and thus effectively bosonic molecules with repulsive mean field interactions. Like their atomic counterparts, bosonic molecules condense into BECs [Gre03, Joc03, Zwi03] at sufficiently low temperatures, while weakly attractive interacting fermions are well described by BCS theory where the Fermi surface becomes unstable towards Cooper pairing at arbitrarily weak interactions [Bar57]. Experimentally, it is possible to smoothly transfer the one limit into the other by varying the magnetic offset field in the vicinity of the Feshbach resonance. For this reason, this regime is referred to as the BEC-BCS crossover. It was theoretically studied several decades ago ([Eag69, Leg80]) and realised later on ([Reg04, Zwi04]) in an ultracold atomic system. Note that there is no sharp phase transition between a bosonic and a fermionic regime, but that there is rather a smooth crossover around the resonance - the so-called unitary regime - where the system has to be described by both bosonic and fermionic degrees of freedom (for a schematic illustration see figure 2.5). The unitary system is characterised by $k_F|a| \gtrsim 1$, that is by the condition that the scattering length is larger than the typical inter-particle distance. Since furthermore this distance is much larger than the range of the scattering potential, the unitary regime is an example of the unusual case of a system which is both dilute and strongly interacting. It is called unitary because the scattering amplitude assumes the form $f_0(k) = \frac{i}{k}$ and thus becomes independent of the scattering length. Therefore, the only relevant length scales remaining are the inverse Fermi wave vector and the thermal de Broglie wavelength, and accordingly all thermodynamic quantities are expressions of E_F and T/T_F only. Although no complete theoretical description of the unitary regime is available, it is well believed to be stable and show superfluidity at some temperature [Gio08].

Despite the missing analytic solution for the many-body problem across the whole BEC-BCS crossover, there are several approximate but qualitatively correct models, which allow to smoothly switch between the different regimes. For example, it is possible to

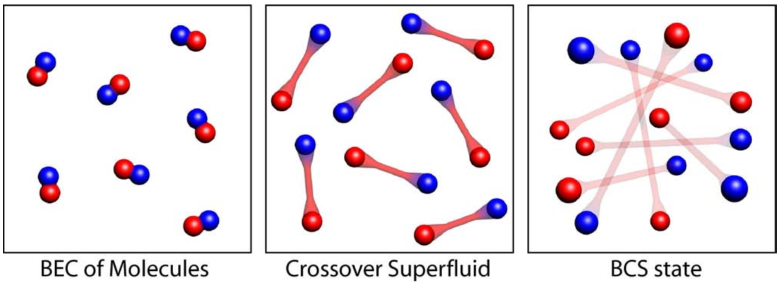

Figure 2.5: Schematic illustration of the BEC-BCS crossover. At low temperatures in the BEC limit, the two spin states ('red' and 'blue') pair up into tightly bound molecules, while in the BCS limit, they form de-localised Cooper pairs. In the intermediate regime, the system exhibits both bosonic and fermionic behaviour. Taken from [Ket08].

extend the standard BCS mean field theory over the whole crossover (at least for zero-temperature; for finite-temperature it is crucial to include quantum fluctuations as well) [Eag69, Leg80]. In zero-temperature BCS mean field theory, for example the well-known expression

$$E_k = \sqrt{\Delta^2 + \eta_k^2} \tag{2.31}$$

for the spectrum of the elementary excitations can be obtained, where Δ is the (position dependent) order parameter, and $\eta_k = \frac{\hbar^2 k^2}{2m} - \mu$ [Gio08]. In the weak coupling limit on the fermionic side with $\mu = E_F$, the standard BCS result of the gap, $\Delta_{Gap} = \Delta$, with a minimum of the excitation spectrum at $k = k_F$ is recovered. The minimum shifts towards $k = 0$ when approaching the unitarity limit and is exactly zero when the chemical potential changes sign on the BEC side. As for the energy, also for the ground state one recovers the familiar result

$$|BCS\rangle = \prod_k (\cos\theta_k - \sin\theta_k \hat{a}^\dagger_{k\uparrow}\hat{a}^\dagger_{-k\downarrow})\,|0\rangle\,, \tag{2.32}$$

with θ_k given by $\sin\theta_k = \sqrt{(1 - \eta_k/E_k)/2}$, where the wave function of the N-particle sub-state[8] may also be expressed in terms of pair orbitals of the form [Gio08]

$$\Psi_{BCS}(r_1, \ldots, r_N) = \hat{A}\left[\psi(r_{1\uparrow 1\downarrow}) \ldots \psi(r_{N\uparrow N\downarrow})\right], \tag{2.33}$$

---

[8] The BCS state itself has no fixed particle number.

where $\hat{A}$ is the antisymmetrisation operator. The pair function $\psi(r) \propto \int dk \tan\theta_k e^{ikr}$, depending on the relative coordinate $r_{i\uparrow i\downarrow} = |r_{i\uparrow} - r_{i\downarrow}|$ of the particle pair i, reduces to the simple molecular wave function $\psi(r) \propto \frac{e^{-\frac{r}{a}}}{\sqrt{2\pi a r}}$ in the deep BEC regime, and thus describes the bosonic pairing properly. With more detailed studies, it is possible to extract general equations of state in the full crossover region from the mean field analysis, resulting in a - at least - qualitative understanding of the BEC-BCS crossover in three dimensions. More quantitative results may be obtained in addition for example by QMC methods.

2.2.2 The 2D BEC-BCS crossover

As elaborated before, condensation into a state with true long range order is prohibited in two dimensions for any finite temperature. Nevertheless, it is possible to transfer the system smoothly from a regime where it is described in terms of bosonic degrees of freedom into a fermionic system similar to the 3D case by means of a Feshbach resonance. In analogy to the three-dimensional case, this crossover region is therefore again referred to as (2D) BEC-BCS crossover even for finite temperatures, where the mechanisms of Bose-Einstein and BCS condensation have to be replaced by their respective BKT analogues now.

In two dimensions, the relevant quantity characterising the crossover is given by $\ln(k_F a_{2D})$. The BCS limit is correspondingly given by $\ln(k_F a_{2D}) \gg 1$, where the pair size is much larger than the inter-particle spacing, and thus many-body effects have an important impact on the pairing mechanism. In the BEC limit given by $\ln(k_F a_{2D}) \ll -1$, on the other hand, the pair size is much smaller such that the system is well described in terms of bosonic molecules (compare again figure 2.5). Note again that, unlike in the 3D case, in 2D a two-body bound state exists for any scattering length. The form of the parameter $\ln(k_F a_{2D})$ implies that it is possible to reach different regimes in the crossover by either changing the scattering length or the density (and therefore the Fermi wave vector).

First qualitative insights into the 2D BEC-BSC crossover may be again obtained by (zero-temperature) BCS mean field theory. However, it is important to keep in mind that mean field results are, due to the increased role of fluctuations, in general not expected to show good agreement with the exact results in two dimensions. Similar to before, the quasi-particle excitation energies are given by

$$E_k = \sqrt{\Delta^2 + \eta_k^2}, \tag{2.34}$$

with the order parameter Δ and $\eta_k = \frac{\hbar^2 k^2}{2m} - \mu$ as before [Lev15]. The chemical potential takes the form of $\mu = E_F - E_B/2$ and evolves from E_F in the BCS to $-E_B/2$ in the BEC limit. The order parameter is given by $\Delta^2 = 2E_F E_B$, such that the minimum energy to break a pair is given in the BEC limit for a negative μ by $\Delta_{Gap} = E_B$, as expected for a molecular BEC. Note furthermore that when perturbing away from the 2D limit to $E_F \approx \omega_z$, mean field theory predicts an increased order parameter Δ [Lev15]. More quantitative results may be obtained for example by perturbative calculations in the limiting cases of $\ln(k_F a_{2D}) \gg 1$ or $\ll -1$, and subsequently extending the range of the calculations by interpolation or QMC methods [Lev15].

Similar to the unitary regime in 3D, the strongly interacting region where $|\ln(k_F a_{2D})| \lesssim 1$ is of special interest. However, the crossover point cannot be defined by a sign change of the scattering length a_{2D} as in the 3D case, since it is always positive. It is rather natural to define it by a sign change of the chemical potential, since - from a mean field perspective - this crossover point marks the change from the minimum of the gap at finite momentum to a minimum gap at zero momentum. This means that the fermionic regime is defined by still showing remnants of a Fermi surface. Within mean field theory, the crossover point therefore corresponds to $\ln(k_F a_{2D}) = 0$. More accurate QMC calculations suggest the crossover point to be at significantly larger values of $\ln(k_F a_{2D}) \simeq 0.5$ [Lev15]. The relation between μ and the quasi-particle dispersion is in general far from trivial when going beyond the simple mean field picture, such that the naive interpretation of the crossover point given above is not strictly valid. However, a negative μ still corresponds to strong deviations from fermionic behaviour and the definition of the crossover point remains meaningful.

True long range order exists in the 2D BEC-BCS crossover only for zero temperature. For small finite temperatures, quasi-long range order is preserved up to a critical temperature T_C where it is destroyed by the BKT mechanism. The critical temperature may be calculated in the limiting cases of a weakly interacting Bose gas and the BCS limit, and subsequently interpolated to obtain an estimate in the whole crossover. For $\ln(k_F a_{2D}) \ll -1$, T_C is given by

$$\frac{T_C}{T_F} = \frac{1}{2}\left[\ln\left(\frac{\mathcal{B}}{4\pi}\ln\left(\frac{4\pi}{k_F^2 a_{2D}^2}\right)\right)\right]^{-1} \tag{2.35}$$

with $\mathcal{B} \approx 380$, while for $\ln(k_F a_{2D}) \gg 1$ the Thouless criterion (including additional corrections due to particle-hole fluctuations)

$$\frac{T_C}{T_F} = \frac{2e^{\gamma}}{\pi k_F a_{2D}} \tag{2.36}$$

is obtained [Lev15]. A schematic phase diagram interpolating the above limits is shown in figure 2.6a. Note that a maximum of the transition temperature is expected to occur in the strongly interacting regime. The phase diagram across the crossover regime has been measured in our group [Rie15a] and the BKT type of the transition has been shown as well [Mur15b]. The phase diagram is depicted in figure 2.6b. Note again that an increase of T_C is expected when perturbing away from the 2D limit.

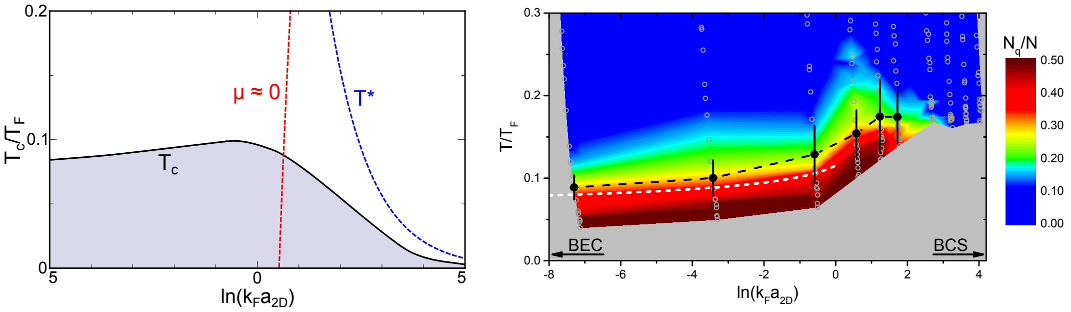

(a) Schematic phase diagram

(b) Measured phase diagram

Figure 2.6: (a) Schematic phase diagram of the 2D BEC-BCS crossover. The critical temperature is indicated by a solid line, while the dashed red line corresponds to $\mu \approx 0$. Furthermore, the expected crossover temperature T^* for the occurrence of a pseudogap (see subsection 2.2.3), as obtained from the Thouless criterion, is indicated by the blue dashed line. Taken from [Lev15]. (b) Experimental phase diagram. The transition temperature is determined for different interaction parameters by a sudden increase in the peak zero momentum density in the pair momentum distribution. The results are indicated by the black datapoints (the dashed black line is solely a guide to the eye). In a colour scale, the non-thermal fraction is indicated as well. Note that it is non-zero even above the transition temperature due to Bose-enhancement. Taken from [Rie15a].

2.2.3 Pseudogap

In a two-component Fermi gas with (arbitrary) weak attractive interactions below a critical temperature T_C, BCS theory describes the emergence of a superfluid phase with many-body Cooper pairing and a gapped excitation spectrum. Therefore, in a BCS superfluid a minimum energy of Δ_{gap} is required to place an excitation into the system by breaking a pair, where the notion of a gap refers to the vanishing weight in the density of states at the Fermi surface. In BCS theory, both pairing and phase transition happen at the same temperature T_C, as the phase transition is indicated by an instability of the Fermi surface towards pair formation [Alt10].

More generally, allowing for stronger interactions as well, fermionic pairing and superfluidity are still closely related, yet distinct phenomena [Bau14]. Most prominently in high-T_C cuprates, there exists a so-called pseudogap region for a finite doping factor and a finite temperature above T_C [Din96], where there is already fermionic pairing but no long range order in the phase. As the origin and the mechanisms leading to a pseudogap as well as its implications are not yet well understood, studying pairing above T_C on a fundamental level is of great interest.

A pseudogap region might be observable in a strongly interacting atomic Fermi gas [Bau14, Lev15]. It is important to specify, however, that with a definition of a pseudogap as 'pairing above T_C in a Fermi gas', such a regime may be reached trivially by considering the BEC side of the BEC-BCS crossover, where the two-component Fermi gas is paired up into molecules even significantly above T_C. Therefore, in this thesis a more restrictive definition as in [Lev15] with a pseudogap only for true fermionic many-body paring is used. Thus, a pseudogap is defined by a reduced spectral weight at the Fermi surface above T_C implying in particular

- many-body pairing above the critical temperature T_C
- a gapped excitation spectrum above T_C with a minimum at a finite momentum k
- the presence of (at least) remnants of a Fermi surface resulting most importantly in $\mu > 0$. In particular, slightly above the resonance, strong interactions can destroy any Fermi surface such that $\mu > 0$ is only given for $\ln(k_F a_{2D}) \gtrsim 0.5$ [Lev15].

In a simplified qualitative picture, the emergence of a pseudogap might be illustrated by considering a complex order parameter of the form $\Delta(\vec{x}) = |\Delta(\vec{x})|e^{i\theta(\vec{x})}$ [Fel11]. Below the critical temperature T_C, a gapped BKT superfluid forms, resulting in $\langle\Delta(\vec{x})\rangle \equiv \Delta_{sf}(\vec{x}) > 0$. However, above the critical temperatures, thermal and quantum phase fluctuations destroy (quasi) long range order and thus $\langle e^{i\theta(\vec{x})}\rangle = 0 = \langle\Delta(\vec{x})\rangle$. Nevertheless, the modulus of the order parameter may remain finite up to a crossover temperature T^*, $\langle|\Delta(\vec{x})|\rangle \equiv \Delta_{pseudogap} > 0$, resulting in a pseudogap region between T^* and T_C. The mechanisms leading to a pseudogap are still little understood. It is expected, however, that the region is more prominent in 2D as the enhanced quantum fluctuations lower T_C, while not directly influencing $\langle|\Delta(\vec{x})|\rangle$.

Pairing above the critical temperature for superfluidity in a quasi-2D system has been observed in the BEC-BCS crossover region [Fel11, Som12], however up to now not in an unambiguously fermionic regime, where the pairing cannot be explained by two-body correlations alone anymore [Lev15].

2.3 Particles in periodic potentials

By means of optical dipole traps, where atoms are confined in the intensity maxima of a red detuned laser (or the minima of a blue detuned laser), nearly arbitrary potential landscapes may be constructed, which are in addition, as opposed to periodic potentials in condensed matter systems, nearly free of defects and very well controllable. For example, by interfering a laser beam with a counter-propagating copy of itself, a standing wave, corresponding to a one-dimensional lattice trap, is created. In a similar fashion, by superimposing two or three of these standing waves (with the polarisation and respective laser frequency chosen such that interference between different lattice arms is avoided), two- or three-dimensional lattices may be created. This section deals with the most important implications of particles in periodic potentials and introduces the Hubbard model, widely used in condensed matter physics and in the context of ultracold gases to describe many-body physics in deep lattices.

2.3.1 Non-interacting particles and band structure

The motion of a particle in a (for simplicity) one-dimensional periodic potential $V(x) = V(x+d)$ is described by the Schrödinger equation

$$\left(\frac{\hat{p}^2}{2m} + V(x)\right)\Psi = E\Psi. \tag{2.37}$$

The important addition is that the periodic potential breaks the continuous translation symmetry of the Hamiltonian and replaces it with a discrete one. One consequence is the so-called Bloch theorem, stating that the eigenfunctions of the above Hamiltonian may be written in the form

$$\Psi_{nq}(x) = e^{iq\cdot x}u_{nq}(x), \tag{2.38}$$

where $u_{nq}(x+d) = u_{nq}(x)$ is a function with the same periodicity as the potential, n denotes different energy levels (more precisely energy bands), and q is a quasi-momentum vector such that $\Psi(x+d) = e^{iqx}\Psi(x)$ holds [Ash76]. Due to the periodicity, u_{nq} may be expanded in a discrete Fourier series

$$u_{n,q}(x) = \sum_{l=-\infty}^{\infty} c_{n,q}^{(l)} e^{ilk_l x}, \tag{2.39}$$

$$\Psi_{n,q}(x) = \sum_{l=-\infty}^{\infty} c_{n,q}^{(l)} e^{i(lk_l+q)x}, \tag{2.40}$$

where k_L is the reciprocal lattice vector, and the quasi-momentum can be restricted to the range $q \in \left(-\frac{k_L}{2}, \frac{k_l}{2}\right]$. Therefore, the solutions for the wave functions are simply given by the sum of plane waves with momenta differing by multiples of the lattice momentum. For a simple model potential

$$V(x) = V_0 \sin^2\left(\frac{\pi x}{d}\right), \tag{2.41}$$

the band structure may be solved by including only a finite number of terms in the Fourier sum in equation 2.39. Consider first the weak potential limit: In this case only the terms with $l = -1, 0, 1$ have to be considered. Without any potential (however keeping the discrete translation symmetry), the energies corresponding to $l = 0, 1$ ($l = -1, 0$)

are degenerate for $k = k_l/2$ $(-k_l/2)$. Introducing a weak coupling leads to an avoided crossing at this quasi-momentum and a band gap opens up where the density of states is zero, while near $k = 0$ the dispersion relation is still quadratic, however with a slightly increased effective mass. More generally, the results of numerical calculations of the band structure for the above model potential are shown in figure 2.7. A common feature for all lattice depths is the band gap. Therefore, if all available states in one band are filled by fermionic particles, a certain energy, given by the gap, is needed to create an excitation and the system becomes insulating. This is referred to as a band insulator. In the limit of a very deep lattice, the dispersion relation in the lower bands is approximately flat and the system may be described by an array of independent (decoupled) confining wells. For low lying states near the bottom, the wells may be approximated by a harmonic potential with frequency $\hbar\omega_{on-site} = 2\sqrt{VE_R}$, where $E_R = \frac{\hbar^2 k^2}{2m}$ is the recoil energy which gives the energy gained by a particle of mass m scattering one lattice phonon.

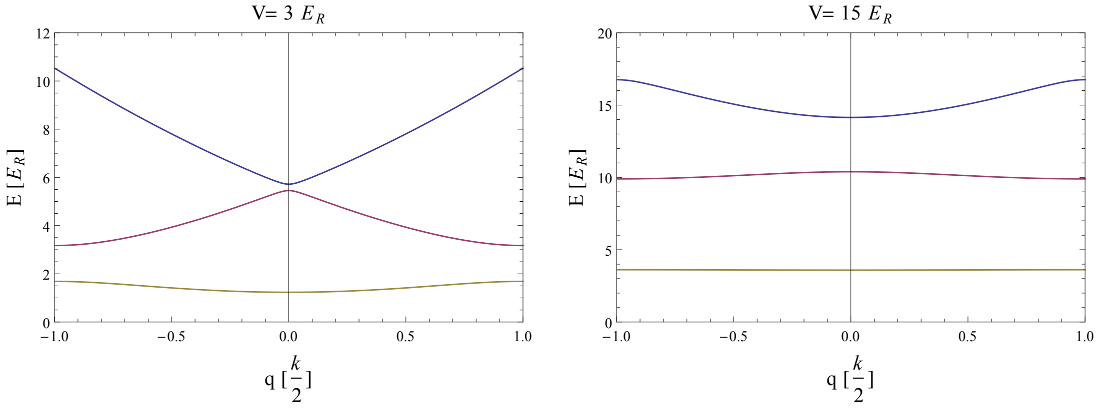

(a) Shallow lattice

(b) Deep lattice

Figure 2.7: Numerically calculated band structure of a 1D lattice. The lowest three bands are shown for (a) $V = 3E_R$ and (b) $V = 15E_R$. For a deeper lattice, the effective mass of the low momentum particles increases and thus the bands become flatter and the band gap larger. Taken from [Bay15].

The considerations done here may be extended to higher dimensions in a straightforward manner, since the dimensions are separable (for a square lattice). However, it is important to keep in mind that bands in different directions may overlap and not all band gaps 'survive'. For the 2D square lattice systems considered in this thesis, the band gap between the first and second band persists.

2.3.2 Tight binding approximation and Hubbard model

For a weak lattice, delocated Bloch waves are a suitable basis to describe the particle wave functions. However, for deeper lattices, a change of perspective towards particle states localised at specified lattice sites becomes adequate. A suitable basis is given by the Wannier states, defined as the discrete Fourier sum of the Bloch wave functions [Ash76]:

$$w_n(x - x_i) = \frac{1}{\sqrt{N}} \sum_q e^{-iqx_i} \Psi_{n,q}(x) \tag{2.42}$$

Here, N is the number of lattice sides and n denotes again the band index. The band index is dropped in the following, since for all experiments described in this thesis, it is made sure that all energy scales are smaller than the band gap to the second band. Nevertheless, excitations in the direction perpendicular to the lattice cannot be excluded. Therefore, as stated before, in the limit of a deep lattice a model of weakly coupled 1D tubes is the better picture to describe the system with.

In the basis of the Wannier states, the operator destroying a particle at point $\vec{x}$ may be written in the form[9]

$$\hat{\Psi}(\vec{x}) = \sum_i w(\vec{x} - \vec{x}_i)\hat{a}_i, \tag{2.43}$$

where $\hat{a}_i$ is the operator annihilating a Wannier state centred around x_i. Still neglecting interactions, the Hamiltonian describing the free motion in a periodic lattice may then be written in the tight binding form [Blo08]

$$H = \sum_{i,j} J(x_i - x_j)\hat{a}_i^\dagger \hat{a}_j. \tag{2.44}$$

Here, J is the hopping matrix element describing tunneling and thus connecting different lattice sites, and may be calculated by

$$J(x_i - x_j) = \int d^3x \Psi(x - x_i) \left(\frac{\hbar^2 \nabla^2}{2m} + V(x) \right) \Psi(x - x_j). \tag{2.45}$$

Zero range interactions may be included by an additional on-site interaction energy

$$U = \int d^3x \frac{4\pi\hbar^2}{m} a |\Psi(x)|^4. \tag{2.46}$$

---

[9] More precisely, instead of the Wannier function used here, for a 2D lattice the product of Wannier functions in x- and y-direction as well as the corresponding wave function in the direction perpendicular to the lattice could be used.

Since furthermore, for a reasonably deep lattice, only next neighbour tunnelling has to be considered, the system is described by the so-called Bose-Hubbard Hamiltonian [Blo08]

$$H = -J \sum_{\langle i,j \rangle} a_i^{\dagger} a_j + U \sum_i n_i(n_i - 1) + \sum_i (E_i - \mu) n_i, \tag{2.47}$$

where the first term describes next neighbour hopping (assumed to be independent of the lattice sites) with $\langle i, j \rangle$ indicating summation over only next neighbours. The second term accounts for on-site interactions, where n_i is the number of particles at position x_i. With the last term, the chemical potential as well as a possible site dependent energy offset E_i (for example introduced by an overall harmonic confinement) are included. A schematic illustration is shown in figure 2.8 The Hubbard model is one of the most simple non-trivial lattice models. Nevertheless, the two competing energy scales of the tunnelling and the on-site interactions result in two distinct low-temperature phases to be briefly discussed below. It is interesting to note that the Hubbard model may be realised nearly without approximations in a cold atom system due to effectively zero range s-wave interactions and well-controlled optical lattices[10]. On the other hand, it describes typical condensed matter systems, where interactions are typically long range and lattices imperfect, only in a very crude approximation.

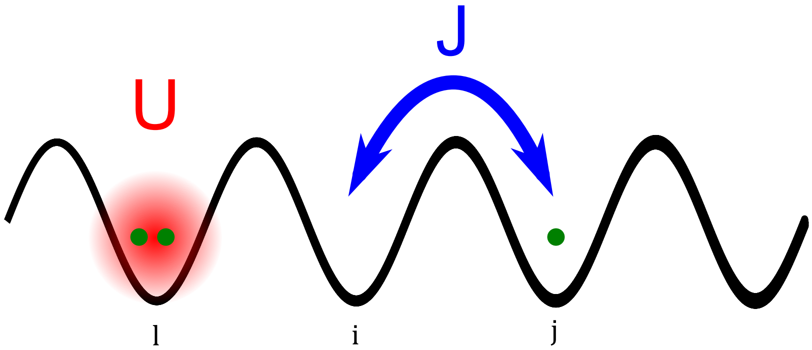

Figure 2.8: Schematic illustration of the Hubbard model which is characterised by two competing energy scales. The next neighbour tunnelling amplitude J describes tunnelling between any two lattice sites i and j and favours delocalisation, while the on-site interaction energy U adds an energy penalty for any two particles at any lattice site l and thus favours localisation.

The zero-temperature ground state of the Hubbard model changes with the ratio of U/J. For small interaction energies, tunnelling dominates and the system minimises its energy

---

[10] The experiments described here are however not aimed at a perfect simulation of the Hubbard model. Nevertheless, it helps to identify the different phases to be expected.

by delocalisation. In the extreme limit of zero interactions, all particles occupy the $k = 0$ Bloch state and the system condenses into a superfluid, with a fixed phase to minimise the kinetic energy. A fixed phase automatically results in a maximally fluctuating particle number and the occupation on each lattice site is described by [Blo08]

$$|\Psi_{SF}\rangle = \frac{1}{\sqrt{N!}} \left(\frac{1}{\sqrt{N_L}} \sum a_i^\dagger \right)^N |0\rangle \,, \tag{2.48}$$

where N and N_L are the particle and the lattice site number. In the other extreme limit for negligible tunnelling, considering first the case of unity filling, i.e. $N = N_L$, each lattice site is occupied exactly once. The ground state then takes the form of a product of Fock states [Blo08]

$$|\Psi_{N=N_L}\rangle_{J=0} = \left(\prod_i \hat{a}_i^\dagger \right) |0\rangle \,. \tag{2.49}$$

This state corresponds to an insulator, since it takes a finite energy U to introduce an excitation. In contrast to the band insulator described before, the mechanism here is however based on the strong repulsion localising the atoms. This phase is called a Mott insulator (MI). It is important to stress however, that a Mott insulator phase persists even for finite (yet large) U/J, where the ground state is no longer a simple product state. Therefore, rather the incompressibility requirement $dn/d\mu = 0$ is a suitable defining property for the insulating Mott state.

A zero-temperature schematic phase diagram for the (homogeneous) Bose-Hubbard model is drawn in figure 2.9 as a function of J/U, where the density is controlled by the chemical potential (again in units of U). In addition to the unity filling Mott insulator described above, MI phases are possible for other integer fillings as well, while for any non-integer filling the system is in a superfluid state, due to the highly mobile excessive atoms. Within mean field theory, the critical value for a transition from a Mott insulator to a superfluid is given by $U/J = 23.2$ for a 2D square lattice, while QMC calculations suggest a smaller value of $U/J = 16.2$ [Wes04].

In complete analogy to the Bose-Hubbard Hamiltonian, fermions on a lattice may be described by a Hubbard Hamiltonian as well. The Fermi-Hubbard model is obtained by introducing fermionic (anti-)correlation relations in equation 2.47.

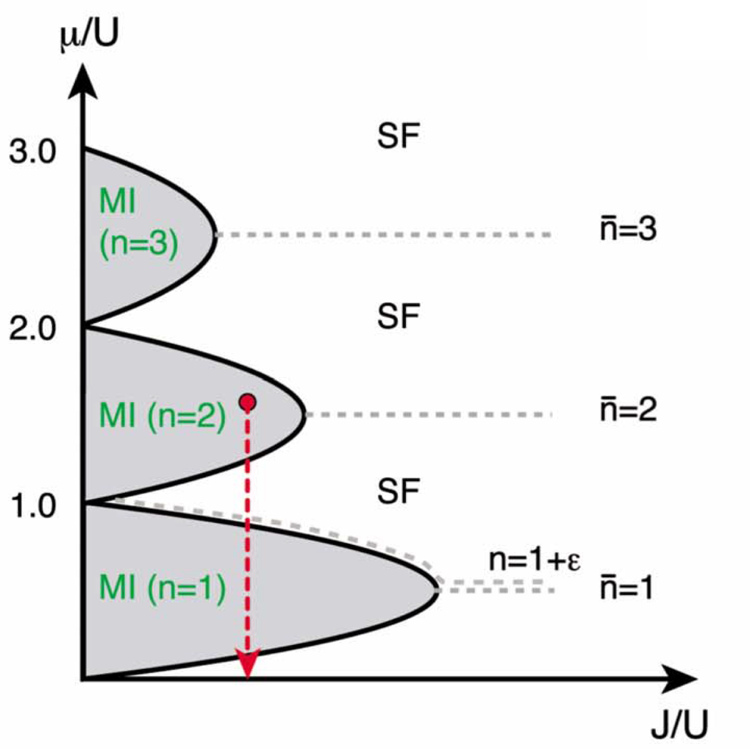

Figure 2.9: Schematic zero-temperature phase diagram of the homogeneous Bose-Hubbard model. The chemical potential controls the density and dashed lines indicate integer filling factors of 1, 2 and 3 corresponding to the three Mott lobes shown. Note that by controlling the chemical potential at a fixed J/U, the phase boundary between superfluid and Mott insulator may be crossed, while for a fixed non-integer filling, by varying J/U, the chemical potential adapts such that the system is alway superfluid as indicated by a dashed line for a filling of $n = 1 + \epsilon$. Taken from [Blo08].

3 Principles of noise correlation experiments

One of the two methods for studying many-body correlations used in this thesis is based on extracting momentum space density-density or noise correlations. As soon as a system is described by single-particle wave functions and phase coherence, studying the momentum distribution allows access to the coherence properties. Among the best known examples are interference experiments with atomic BECs, where interference fringes indicate coherence [And97]. These methods fail, however, as soon as a description of the many-body system by single-particle matter waves is no longer possible. For such a system the momentum distribution is featureless. Nevertheless, these systems can have higher order correlations, for example in the form of fermionic pairing or real space density correlations in a lattice system, as pointed out before. As will be illustrated in this chapter, it is possible to access these correlations by studying the density fluctuations in momentum space instead of the momentum density itself.

This chapter aims at giving an overview over the basic principles and applications of a noise correlation analysis for various systems of interest. While the idea of using noise correlation measurements for atomic systems is relatively new [Alt04], it is based on the Hanbury Brown and Twiss effect, well known from quantum optics since 60 years [Bro56b]. The chapter is structured as follows: First the Hanbury Brown and Twiss effect is reviewed briefly in section 3.1 as a motivation to then study second order correlations for atomic systems in more detail in section 3.2

3.1 Hanbury Brown and Twiss experiment

In the 1950s, the astronomers Hanbury Brown and Twiss were interested in measuring the diameter of stars. The established method at that time was based on the Michelson stellar interferometer [Bro54, Fox06]. Here, the spatial coherence, i.e. the first order correlation function, of starlight in the far field is probed by observing the visibility of interference in a Young double slit experiment. The degree of spatial coherence of the initially incoherent starlight is given by the spread of angles of the light arriving at the interferometer[1]. Thus, assuming the star to be described by incoherent light passing

---

[1] Note to this end that it is possible to increase the degree of spatial coherence of in- or partially coherent light (at the cost of reducing its intensity) by letting it pass through a small aperture (see e.g. [Sal91]).

through a circular aperture with the radius of the star, interference is visible up to a slit distance of $d = 1.22\frac{\lambda}{\delta\theta}$. This result may be obtained by a Fourier transform of the aperture function [Sal91]. To resolve the small angles of typical stars, long baselines up to several km are needed and the signal has to be guided and interfered while conserving the phase information, which is technologically challenging. Hanbury Brown and Twiss suggested to replace the slits by square law detectors and measure the second order correlation function instead of the first order one. The striking result is that with this much simpler setup (and a suitable definition of the second order correlation function g_2), the same correlation signature in the g_2-function as before in the first order correlation function is recovered. Although this result may be obtained already with a classical treatment of light, it was controversially debated at that time and lead to a number of follow-up papers (see e.g. [Bro56a]).

In order to get some intuition, note that the important measured quantity is the correlation signal $G_2 = \langle \Delta I_1(d) \Delta I_1(d + \Delta d)\rangle$, where d and $d + \Delta d$ are the positions of the two detectors and $\Delta I_{1,2}(d)$ are the fluctuations on the measured mean intensity. These fluctuating intensities are caused by the randomness, i.e. an additional random phase, of the starlight which is assumed to be chaotic. In the far field, however, the light is again partially coherent, and as long as the light impinging on the detectors is within the coherence length d_C, the intensity fluctuations will be correlated, leading to a non-zero G_2. For the one extreme case of $\delta d = 0$, one arrives at the mean square fluctuations $G_2 = \langle \delta I^2(d)\rangle > 0$ (while $\langle \delta I(d)\rangle = 0$ per definition), and for the other extreme $d \gg g_C$ at $G_2 = \langle \delta(I(d)I(d + \Delta d))\rangle = \langle \delta I(d)\rangle \langle \delta I(d + \Delta d)\rangle = 0$.

The considerations up to now were based on classical (fluctuating) fields. It is however possible to find a description in terms of quantum operators as well. This might be used to explain HBT experiments with single photon sources as well [Fox06]. Furthermore, there is no reason to restrict the applicability of the HBT effect to massless bosonic photons. More generally, also massive quantum particles of both bosonic and fermionic statistics might be considered. These atomic noise correlations are described in the following section in some detail.

3.2 Atomic noise correlations

When probing coherence properties of ultracold atomic gases, first order correlations were considered in the previous sections. With their help, it is possible to probe single-particle coherence, since the first order correlation function g_1 contains exactly the same information as the single-particle reduced density matrix.

The g_1-function is therefore well suited to probe (real or quasi-) long range order in the phase and an important tool for probing condensed states of matter. Nevertheless, there are strongly correlated systems to be realised with ultracold atoms which withstand a description in terms of single-particle matter waves. Think for example of a Mott insulator: In a (zero-temperature, $J = 0$) Mott insulator state, each site of a lattice is populated by exactly one atom, but there is no phase coherence between different lattice sites whatsoever. This results in the mean momentum distribution of the system being simply the incoherent sum of all the different atomic momentum distributions, and therefore being effectively featureless, as illustrated in figure 3.1. Thus, no information

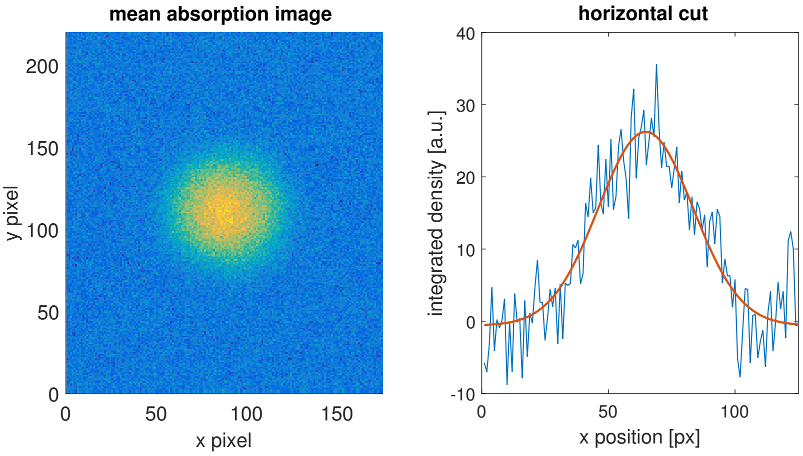

Figure 3.1: On the left hand side the measured mean momentum distribution of an atomic cloud is shown. The overall shape of the cloud is effectively featureless and takes the form of a Gaussian. On the right hand side a horizontal cut through the momentum distribution of a single shot is shown together with a Gaussian fit of the cloud shape. On top of the mean distribution fluctuations are clearly visible. Note that they are, as illustrated in section 5.3, partly caused by photonic noise too. Note furthermore that the momentum distribution shown is not that of an actual Mott insulator, but of a thermal gas in a deep lattice, where the momentum distribution is expected to be qualitatively the same.

can be extracted from the g_1-function, which assumes a constant value of 0. In contrast, a Mott insulator is characterised by perfect density correlations, since the atoms are maximally localised. The first order correlation function g_1 is a second order function in the field operators and therefore to first order in the density. Hence, it is by construction not suited to study density coherence. The proper object to study is rather the density-density correlation function g_2, which is to second order in the density (and a fourth order function in the field operators).

The following paragraphs give some intuition on the principles and applications of density-density or noise correlations. A more rigorous derivation of the relevant quantities will be given in subsection 6.3.1. These next paragraphs are based on the original proposal paper by E. Altman, E. Demler and M. D. Lukin [Alt04] as well as a comprehensive review paper by S. Fölling [Föl14].

3.2.1 General idea

In figure 3.1, a typical absorption image expected from the momentum distribution of a Mott insulator state[2] was already shown. It shows no distinct features. In addition, figure 3.1 shows a cut through the measured momentum distribution of a single image. Again, the overall shape of the cloud is clearly visible, however significantly 'blurred out' by additional noise on top of it. This is not surprising, even if any noise caused by the imaging process is neglected, since the particle number on a camera pixel is a discrete object and therefore naturally afflicted with (in the easiest case) Poissonian noise. The crucial point is now that this noise contains information on density correlations of the sample. To illustrate this, consider first the toy model of two indistinguishable particles fixed at two different sites of a lattice separated by a distance a, as illustrated in figure 3.2. In the far field, there are two identical detectors at positions x_1 and x_2 separated by a distance d. They measure the probabilities $P(x_1)$ and $P(x_2)$ of detecting a particle as well as the combined coincidental probability $P(x_1|x_2)$ of finding one of the particles in each of the detectors. The normalised second order correlation function is now defined as

$$g_2 = \frac{P(x_1|x_2)}{P(x_1)P(x_2)}. \tag{3.1}$$

For classical or distinguishable particles, the combined probability $P(x_1|x_2)$ separates into $P(x_1) \cdot P(x_2)$ and therefore g_2 assumes the constant value of 1. This is not the case for indistinguishable particles, though. Here it has to be taken into account that the different paths (as indicated in the figure) leading to coincidental detection may interfere constructively (destructively) for bosons (fermions). This leads to an oscillation in the g_2-function with a period proportional to the inverse spacing of the two atoms, such that coincidental detection for zero distance d is effectively one (zero)[3]. Analogously, by filling each lattice site with one atom each, all possible distances of atom pairs are realised (with corresponding relative frequencies of occurrence). The combined g_2-signal therefore takes the form of the reciprocal lattice, i.e. the discrete Fourier transform of the lattice. In contrast to the same signal you would obtain for the g_1-function if all atoms interfered coherently, this is a true many-body interference effect. In order to understand these atomic 'HBT type' experiments in more detail, it is instructive to switch into a second quantised picture at this point:
Let $\hat{a}_{i\alpha}$ be the bosonic or fermionic annihilation operator of state α at position x_i.

---

[2] The momentum distribution can be accessed by time of flight methods as elaborated later on.

[3] To compare to the above example plots, the role of the featureless momentum distribution would be assumed by the probabilities of detection at 'pixel' x_i, $P(x_i)$, while, due to the combined probability $P(x_1|x_2)$ not separating, the fluctuations of $P(x_i)$ are correlated.

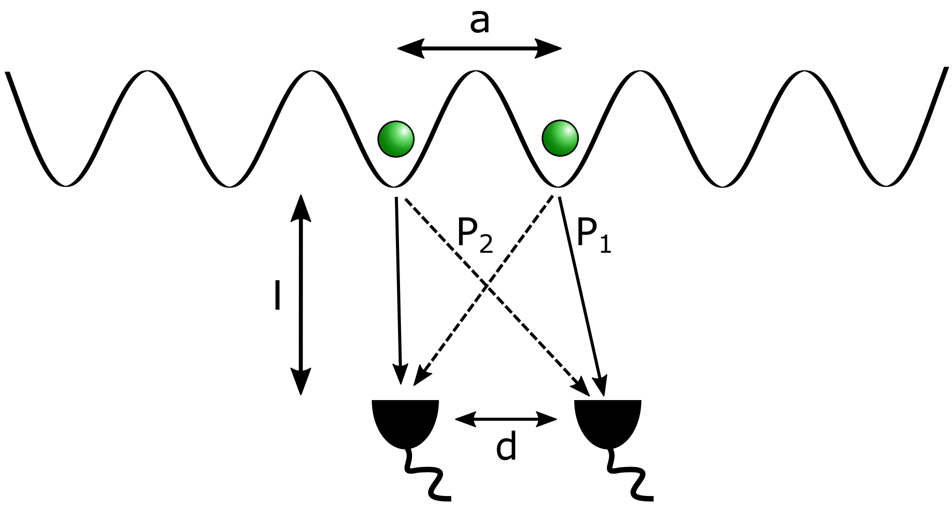

Figure 3.2: Toy model of HBT correlations for two particles in a lattice. The two particles are prepared at fixed positions with a spacing of a and no significant wave function overlap. Subsequently, the particles are recorded in the far field by two equal but independent detectors with separation d. Far field might either mean that the wave functions are allowed to evolve freely (i.e. without the lattice) for an asymptotically large time, or they are imaged in some way and the imaging signal is recorded in the far field. When measuring coincidence events, it is important to consider the interference between the two possible paths P_1 and P_2 leading to joint detection for identical particles. This leads to correlations for bosons and anti-correlations for fermions.

Assuming that at $t = 0$, all interactions are switched off and the particles, now projected onto their free modes, undergo free time evolution, the creation (annihilation) operator at a general time t may be written as

$$\hat{a}_{i\alpha}^{(\dagger)}(x,t) = \Psi(x - x_i, t)\hat{a}_i^{(\dagger)}. \tag{3.2}$$

Accordingly, the density operator is defined as

$$\hat{n}_\alpha(x,t) = \sum_{jk} \hat{a}_{j\alpha}^{\dagger}(x,t)\hat{a}_{k\alpha}(x,t). \tag{3.3}$$

With a definition of a (not yet normalised) density-density correlation function of the type

$$G_{\alpha\beta} = \langle \hat{n}_\alpha(x,t)\hat{n}_\beta(x',t) \rangle \,, \tag{3.4}$$

where the expectation value has to be interpreted as a thermal expectation value for non-zero temperature, it is now possible to evaluate the expected correlation signal for different physical situations. In the following, I will comment on the two instructive examples of a lattice system and a fermionic superfluid without the lattice.

3.2.2 Lattice system

A typical object to investigate, especially in the context of superfluidity, is as elaborated earlier the mean momentum distribution, which can be related to the measured density distribution (in real space) after time of flight (TOF). In a lattice, the exact form of the ladder operators after TOF are determined by the time evolution of the on-site Wannier functions. On the length scales given by the lattice momentum, their envelope function is, after a relatively long TOF, to some approximation constant. On a qualitative level, they can be approximated by a square (in the case of two dimensions) with area W times a phase factor $e^{-iq(x)x_i}$. Here, $q(x)$ defines the correspondence between positions x after time of flight and momenta q, and therefore depends on the exact TOF parameters. With this, the density expectation value is given by:

$$\langle \hat{n}_\alpha(r) \rangle \propto \langle \hat{n}_\alpha(q) \rangle = \frac{1}{W} \sum_{i,j} e^{(i(x_i - x_j)q(x))} \langle \hat{a}^\dagger_{i\alpha} \hat{a}_{j\alpha} \rangle \tag{3.5}$$

This result, i.e. that the first order correlation function and the momentum distribution are related by a Fourier transform/sum, has emerged before in the context of (quasi-) long range order of the condensate phase. It implies that for a condensate where there is (some) long range order and $\langle \hat{a}^\dagger_{i\alpha} \hat{a}_{j\alpha} \rangle \neq 0$ in general, the momentum distribution shows distinct peaks at the lattice momenta (given by the reciprocal lattice), while for a Mott or normal state $\langle \hat{a}^\dagger_{i\alpha} \hat{a}_{j\alpha} \rangle = 0$ for $i \not\approx j$ and the momentum distribution is featureless. Next, consider the corresponding expression for the product of two densities

$$\langle \hat{n}_\alpha(x) \hat{n}_\beta(x') \rangle = \frac{1}{W^2} \sum_{jk,lm} e^{i((x_j - x_k)q(x) + (x_l - x_m)q(x'))} \langle \hat{a}^\dagger_{j\alpha} \hat{a}_{k\alpha} \hat{a}^\dagger_{l\beta} \hat{a}_{m\beta} \rangle , \tag{3.6}$$

where α and β may be indicating the same or different states. For the ease of notation, we now consider only one state and suppress the index in the following. Normal ordering of the operators, using the bosonic (fermionic) commutation (anti-commutation) relation

$$[\hat{a}_j, \hat{a}^\dagger_k]_\mp = \delta_{j,k}, \tag{3.7}$$

yields

$$\hat{a}^\dagger_j \hat{a}_k \hat{a}^\dagger_l \hat{a}_m = \pm \hat{a}^\dagger_j \hat{a}^\dagger_l \hat{a}_k \hat{a}_m + \delta_{lk} \hat{a}^\dagger_j \hat{a}_m. \tag{3.8}$$

The second term, which is always positive, is responsible for a strong autocorrelation peak at zero momentum and will be neglected for now. Assuming a deep lattice where tunnelling is strongly suppressed, the system is well described by Fock states on the different lattice sites with occupation numbers n_j, such that the total particle number N is fixed by $N = \sum_j n_j$. In this case, $\langle \hat{a}_j^\dagger \hat{a}_k \rangle = \delta_{jk} n_j$ and the normal ordered expectation value of the operators evaluates to

$$\langle \hat{a}_j^\dagger \hat{a}_l^\dagger \hat{a}_k \hat{a}_m \rangle = \delta_{jm}\delta_{lk} n_j n_l + \delta_{jk}\delta_{lm} n_{j\alpha} n_{l\beta} + \delta_{jk}\delta_{jl}\delta_{jm} \left(n_j(n_j - 1) - 2n_j^2 \right). \tag{3.9}$$

The first term describes the non-trivial spatial correlations, while the second term corresponds to the correlations of the mean density profiles and will be cancelled in the following by a suitable normalisation. The third term merely adds an offset of $\mathcal{O}(\frac{1}{N})$ and will be neglected.
Inserting equation 3.9 into equation 3.6 and taking the expectation value, we get

$$\langle \hat{n}(x_1, t)\hat{n}(x_2, t)\rangle = \frac{1}{W^2} \sum_{j,l} (e^{i(q(x-x'))(x_j - x_l)} n_j n_l + N^2). \tag{3.10}$$

As a last step, we define the normalised noise correlation by introducing the relative coordinates $d = x - x'$ and $x_{cm} = \frac{(x+x')}{2}$, normalising the above expression as well as integrating out the centre of mass coordinate x_{cm}[4]:

$$g_2 = \frac{\int \langle \hat{n}(x - \frac{d}{2})\hat{n}(x + \frac{d}{2}) dx \rangle}{\int \langle \hat{n}(x - \frac{d}{2})\rangle \langle \hat{n}(x + \frac{d}{2}) dx \rangle} \tag{3.11}$$

Note that this definition of the second order correlation function will be used throughout the remaining part of this thesis for all systems, although it was here introduced in the context of the lattice.
For the case of the deep lattice, this results in:

$$g_2 - 1 = \frac{1}{N^2} \sum_{j,l} e^{iq(d)(x_l - x_j)} n_j n_l = \frac{1}{N^2} \left| \sum_j e^{iq(d)x_j} n_j \right|^2 \tag{3.12}$$

As a first concrete example, let us revisit the above toy model of two atoms at two lattice sites. For this system, $n_1 = n_2 = 1$ while all other occupation numbers are zero. Inserting this into equation 3.12, we get (with the lattice constant a and the plus (minus) corresponding to bosons (fermions))

$$g_2 - 1 = \pm \cos(q(d)a) \tag{3.13}$$

---

[4] This last step might seem unnecessary, since it only cancels the pre factor $\frac{1}{W^2}$ here. However, forfeiting the simplification of a square envelope function of the single-particle wave function, we would have been left with a more complicated expression dependant on x_{cm}.

as expected. Similarly, for a model Mott insulator where $n_j = 1 \; \forall \; j$, the anticipated reciprocal lattice structure obtained already with the naive reasoning above is reproduced:

$$g_2 - 1 = \pm \frac{1}{N^2} \left| \sum_j e^{iq(d)j \cdot a} \right| \tag{3.14}$$

The full power of the noise correlation method becomes even more apparent when you consider a system which exhibits additional complex order. Take for example the idealised case of a perfect Néel ordered state (see figure 3.3). In this system, a balanced two-component gas has arranged itself on the lattice in such a way that the two (pseudo) spin states populate the lattice sites alternately. Calculating the g_2-function for one of the spin components results in peaks at half the lattice momentum, corresponding to a characteristic spacing of two times the lattice constant. The same signature might of course originate from a density wave with a frequency of half the lattice momentum as well. However, if the noise correlation function between the two spin states is recorded as well, the two scenarios can be distinguished by the additional correlation peaks at the lattice momentum in the latter g_2-function. More in general, it was demonstrated numerically that noise correlations are well suited to unambiguously identify antiferromagnetic ordering and its defining properties in a lattice [Bru09].

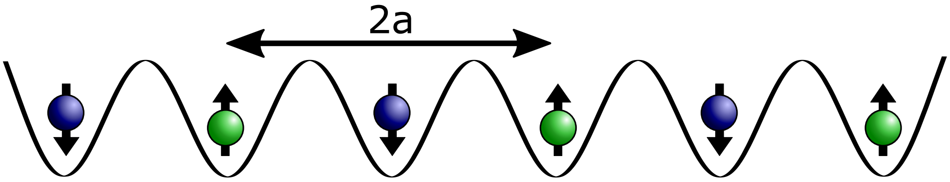

Figure 3.3: Schematic illustration of a state with perfect Néel ordering. When correlating one spin state with itself, a signal corresponding to a lattice with lattice spacing $2a$ is obtained, while when correlating different spin states again correlations of a lattice constant a are recovered. Together this allows to unambiguously identify Néel ordering [Bru09]

3.2.3 Fermionic pairing

The use of noise correlations is not at all restricted to lattice systems. As an example, consider a two-component BCS-type superfluid. While a bosonic BEC might be identified by a pronounced zero-momentum peak, in a BCS phase, naively spoken, the Cooper pairs instead of the individual particles condense. The single-particle density distribution of the fermions in a BCS superfluid differs only very slightly from a Fermi distribution at $T = T_F$ and is therefore experimentally not suited to detect the superfluid

phase. Nevertheless, there exist strong pair correlations in the momentum distribution.
In the easiest case of BCS-type s-wave Cooper pairs, they consist of one spin component at momentum k and the other component at the opposite momentum $-k$, i.e. $|Pair\rangle = |k, -k\rangle$. The spin-spin angular noise correlation function would therefore show a sharp anti-correlation dip at an angle of π for a radius in the vicinity of the Fermi momentum [Alt04, Gre05].

More exotic superfluids with non s-wave pairing are in principle expected to show corresponding signatures.

It is important to note that different methods exist to identify pair condensation, which have been successfully demonstrated already. It is for example possible to project the loosely bound many-body (Cooper) pairs onto deeply bound two-body molecules by a sudden quench in the magnetic field, and subsequently observe the same signature of superfluidity as in the bosonic case [Rie15a]. However, in this case, the information on the nature of the pairing mechanism gets lost.

In addition, pairing can be probed by noise correlations in a pseudogap regime where the fermions are paired, despite not being condensed.

4 Creating and probing an ultracold two-dimensional Fermi gas

In this chapter, the main experimental set-up and the procedure of creating and probing an ultracold two-dimensional Fermi gas in either the single layer of an optical 2D standing wave trap or an optical 2D lattice trap is described. The different parts of the set-up and the general procedures have been previously described in a number of theses. For this reason, this chapter only briefly covers the most important steps and otherwise refers the reader to the respective theses.

For all experiments, both an optimal isolation from the environment and a good optical access is desirable. Therefore, they are conducted in ultra-high vacuum in an octagon experimental chamber with high numerical aperture viewports. An initially hot cloud of ^{6}Li atoms in spin states $|1\rangle$ and $|2\rangle$ is pre-cooled down to a few hundred µK using laser light resonantly interacting with the atoms in a Zeeman slower, and a magneto-optical trap (MOT)[1]. To further reduce the temperature, and increase the phase space density, the atoms are transferred into an off-resonant optical dipole trap and evaporatively cooled into the degenerate regime. During evaporation, a magnetic offset field is applied such that effectively bosonic diatomic molecules form. At the end of evaporation, $\mathcal{O}(10^5)$ molecules at a temperature of a few 10 nK are left. They are transferred into a single layer of an optical standing wave trap. Furthermore, an optical lattice trap may be superimposed. By controlling the different trap depths, the temperature and the interaction strength via the applied offset field, the system of interest is created. It is probed by absorptive imaging of either the in-situ density or momentum distribution. The latter may be obtained by a matter wave focussing technique described below in subsection 4.2.5. Due to the destructive imaging process and the limited lifetime of the ^{6}Li atoms in the different traps, the whole preparation and detection cycle has to be repeated for each individual shot.

4.1 Magnetic fields

Magnetic fields are essential for creating and manipulating a sample of ultracold atoms for several reasons:

---

[1] For the experiments conducted with a $|1\rangle - |3\rangle$ mixture, an additional Landau-Zener sweep transfers the atoms after the pre-cooling from state $|1\rangle$ to state $|3\rangle$ with an efficiency of around 90 %.

- By means of broad Feshbach resonances (e.g. at 832 G for the $|1\rangle - |2\rangle$ mixture [Zür13]), it is possible to tune the interaction strength of the ^{6}Li atoms in a broad range by applying a constant magnetic offset field.
- With a suitable coil configuration, it is possible to create magnetic traps, showing good harmonicity even for relatively large radii. In this experiment, such a trap is used for the matter wave focussing technique described below.
- Due to the magnetic moment μ of ^{6}Li , a magnetic field gradient (e.g. in z-direction) results in a constant force $F_{mag} = -\mu \frac{dB_z(r)}{dz}$ on the atoms. This can be used to compensate gravity and for displacing atoms, especially facilitating the transfer of the atom cloud between different traps.
- Transitions between different hyperfine states correspond to frequencies around $\omega = 2\pi \cdot 80\,\mathrm{kHz}$, and thus may be driven by radio frequency pulses.

In the following, the different magnetic field coils used in this experiment are shortly introduced.

Offset field coils

Tuning an offset magnetic field in the vicinity of the Feshbach resonances at 832 G and 670 G for the $|1\rangle - |2\rangle$ and $|1\rangle - |3\rangle$ mixtures, respectively, allows to tune the scattering length in a wide range and explore the BEC-BCS crossover. Therefore, the coils are required to produce a relatively high magnetic field up to around 1500 G with a high precision. The general design of the coils is described in [Zür09]. The coils were replaced during the course of this thesis, however, and a slightly adapted design was used. Each of the coils consists of 33 windings of a 7.5 mm × 0.46 mm kapton coated copper wire glued to a custom designed water cooled copper heat sink. To optimise the heat conductivity between coil and heat sink, the Kapton coating was removed on the side facing the heat sink and a diamond filled epoxy was used for gluing. The epoxy distinguishes itself by excellent heat conductivity combined with being electrically insulating.

The optimal configuration with two coils to achieve a constant offset field at the position of the atoms is given by the Helmholtz configuration. The offsets coils are however placed slightly further apart, such that the magnetic field within the extension of the atom cloud is still to a good approximation constant but shows a saddle point. The saddle point leads to a small confining potential of $\omega_{rad} \approx 2\pi \cdot 12.1\,\mathrm{Hz}$ (at 692 G[2])in horizontal direction, which is harmonic to a good approximation on a scale up to several mm. In addition, there is an anti-confining potential in axial direction of $\omega_z = 2 \cdot \omega_{rad} \approx 2\pi \cdot 24.2\,\mathrm{Hz}$. The anti-confinement is however negligibly small compared to typical axial confinements, as will be seen below. The exact position of the saddle point is quite sensitive to any

---

[2] The frequency scales as the square root of the magnetic field.

magnetisable material such as for example the current connectors. For this reason, small counter steel blocks are placed in the vicinity of the coils to cancel the aforementioned effects.
The additional radial confinement due to the saddle field improves the radial symmetry of all traps, but more importantly allows for the matter wave focussing technique used for measuring the in-situ momentum distribution, which is explained in subsection 4.2.5. The magnetic field is stabilised by a high precision digital PID loop leading to a relative stability of around 10^{-6}.

MOT coils

On top and bottom of the main chamber (compare figure 4.2), the MOT coils are mounted in an approximate anti-Helmholtz configuration. They consist of four stacked layers of 25 windings of capton coated wire of dimension $1\,\mathrm{mm} \times 5\,\mathrm{mm}$ and are glued to water cooled copper heat sinks. The coils can provide magnetic field gradients up to $85\,\mathrm{G\,cm^{-1}}$ at a current of $70\,\mathrm{A}$. By reverting the current, the direction of the field gradient can be inverted as well. The gradient can be stabilised by a digital PID feedback loop to a relative precision of 10^{-3}. The MOT coils are needed for the creation of the MOT described below, but are also used for pulling the atoms up and down and for tomographic measurements as well.

Radio frequency coils

The internal structure of the ^{6}Li atoms can be manipulated by means of radio frequency (RF) pulses. This has several applications: By long, powerful and thus incoherent pulses an exactly balanced mixture between the two hyperfine states connected by the RF pulse is achieved, which is used in preparing the balanced $|1\rangle - |2\rangle$ mixture, and by an additional Landau-Zener sweep, also a balanced $|1\rangle - |2\rangle$ mixture is created. Furthermore, the transition frequency of an interacting system compared to a non-interacting provides information on interaction effects as well as pairing energies, as will be discussed in detail in the context of the measurements on pairing above the critical temperature. In our experiment, RF pulses are created by a single loop coil placed within the vacuum chamber. Due to the small distance to the atoms, the achievable power at the position of the atoms is increased. For more details on setup and performance of the coils, the interested reader is referred to [Boh12, Heu11].

4.2 Experimental preparation

In this section, the preparation of a quasi-two-dimensional Fermi gas is briefly described.

4.2.1 Experimental control

Each experimental cycle takes around 10 s to 15 s. The timing table for the different subsystems of the experiment is created on an external computer using a LabView interface [Lom08] and sent to an *ADwin pro II* real time controller. The controller has eight analogue inputs as well as 16 analogue and 64 digital outputs, runs on a 300 MHz clock rate and is used for triggering as well as controlling experimental parameters via digital PID feedback loops.

4.2.2 Vacuum system and experimental chamber

A schematic drawing of the vacuum system and the experimental chamber is shown in figure 4.1. To provide optimal isolation from the environment, all experiments are conducted in ultra-high vacuum. Any scattering with thermal background gas would lead to losses, since the ^{6}Li sample is at least six to ten orders of magnitude colder in temperature compared to the lab environment. With the help of several vibration-free getter pump systems, a background pressure of less than 10^{-11} mbar, corresponding to

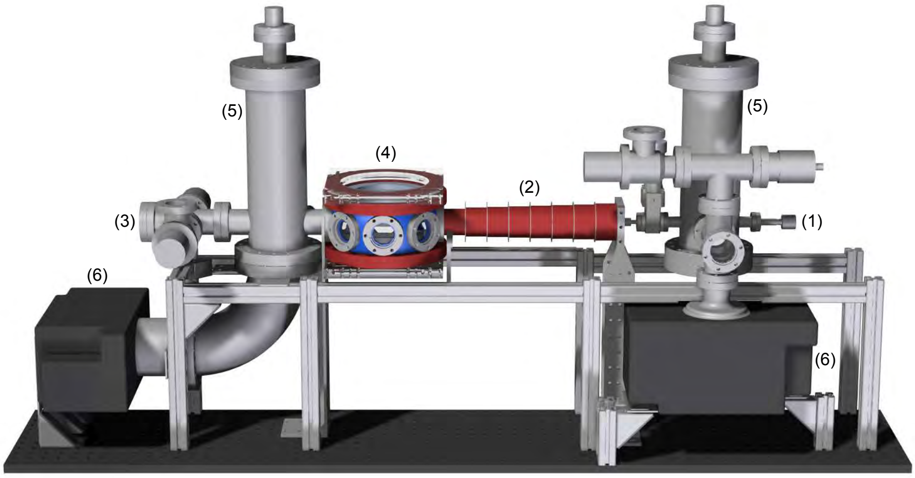

Figure 4.1: Schematic drawing of the vacuum chamber. A small sample of ^{6}Li is evaporated in the oven (1). The hot vapour evades through an aperture and is slowed down in the Zeeman slower (2) by a resonant laser beam entering the chamber through the window (3). The atoms are trapped in a MOT and subsequently in optical dipole traps in the main chamber (4). The ultra-high vacuum is maintained by titanium sublimators in the two towers (5) and by two ion pumps (6). In addition to the pumps, there is a non-evaporable getter coating in the main chamber. Taken from [Rie10].

a lifetime in the MOT of approximately 23 min, is achieved. This is considerably longer than the timescale of individual experimental cycles, such that we are not limited by one-body losses. For more detailed information on the vacuum system, the reader is referred to [Rie10]. The experimental chamber itself is designed such that it offers maximal possible optical access. The spherical octagon has six viewports with a numerical aperture of $NA_{hor} = 0.15$ at the sides and re-entrant viewports with $NA_{vert} = 0.88$ at top and bottom. All viewports have an anti-reflective coating for the wavelengths used in the experiment. The main chamber is schematically drawn in figure 4.2.

The oven is part of the vacuum system as well. Here, a small sample of around 1 g ^{6}Li is heated up to typically 350 °C. The hot lithium vapour leaves the oven at a rate of approximately 10^{16} atoms s^{-1} through a small aperture towards the experimental chamber, leading to a MOT loading rate of roughly 3×10^8 atoms s^{-1}. More details on the oven may be found in [Ser07].

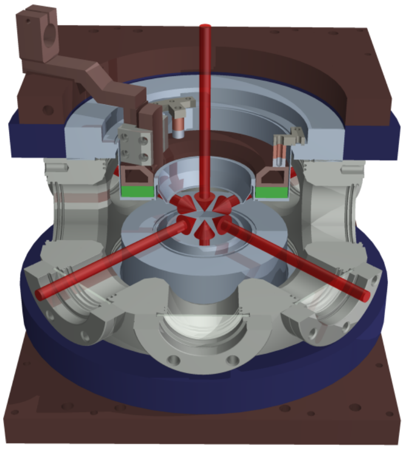

Figure 4.2: Main chamber indicating the orientation of the MOT beams in red and showing the MOT coils in blue as well as the offset field coils in green. In brown, the respective water cooled heat sinks are shown. Optical access is possible in the Zeeman slower axis, three horizontal axes and the vertical axis. Taken from [Wen13].

4.2.3 Resonant pre-cooling

The ^{6}Li vapour escapes the oven at a mean velocity of around 1500 m s^{-1} and is then resonantly pre-cooled and trapped in the experimental chamber using a Zeeman slower and a MOT. The principles of MOT and Zeeman slower are described in detail in many standard text books (see for example [Foo05]).

By driving the lithium D2 transition at around 671 nm with a resonant laser, the atoms

feel a net force in the propagation direction of the laser due to directed absorption and isotropic (spontaneous) re-emission of photons. In the Zeeman slower, this effect is combined with a position dependent magnetic field in order to compensate the Doppler shift during deceleration to slow down (parts of) the atoms to around $50\,\mathrm{m\,s^{-1}}$. Subsequently, these atoms are captured in a MOT, which extends the principle of resonant cooling by shining in lasers from all 3 major axes which are slightly red detuned to offer momentum dependence in absorption, and by an additional magnetic field gradient offering position dependence. The temperature which can be achieved in a MOT is limited due to the photon recoil momentum to the so-called Doppler temperature, which is given for ^{6}Li by $T_{Doppler} = 136\,\mu\mathrm{K}$.
It is important to note that the hyperfine splitting of state $|1\rangle$ and $|2\rangle$ is resolved in resonant cooling, and therefore a superposition of two different frequencies has to be used for resonant cooling. The light is provided by a *Toptica TA pro* tapered amplifier, beat-offset locked to a reference spectroscopy laser. More information on the Zeeman slower is provided in [Sim07], while for detailed information on the MOT the reader is again referred to [Rie10].

4.2.4 Optical dipole traps

Cooling of neutral atoms below the Doppler temperature requires non-resonant techniques. One possibility is evaporative cooling in an optical dipole trap. A far off-resonant laser acts as a conservative potential on the atoms and can be used to trap them. By adiabatically lowering the trap depth, the hottest atoms may evade the trap while the rest of the cloud equilibrates again - now at a lower temperature. With this procedure, neutral atoms can be cooled down into the degenerate regime at the cost of significantly lowering the atom number
The general working principle of an optical dipole trap (ODT) is explained for example in [Gri00]. It can be understood already on a classical level by means of a Lorentz type oscillator model [Sal91]. The electric field of the (far detuned) laser induces a dipole moment in the atom, which oscillates in phase for red detuned and out of phase for blue detuned laser frequencies. This leads to an effective attractive (repulsive) potential for red (blue) detuned laser light. By a more detailed analysis, it can be shown that the effective potential depth scales reciprocally with the detuning, while the scattering rate scales as one over the detuning squared [Gri00]. This means that a conservative potential to any desired approximation may be obtained by increasing the detuning and the intensity at the same time. Here red detuned infrared lasers at a wavelength of around 1064 nm are used. At this wavelength, the scattering rate is already low enough, while the maximum required power of 200 W is still feasible.

3D Crossed Beam Optical Dipole Trap

The 3D Crossed Beam Optical Dipole Trap (CBODT) is created by a 1068 nm *IPG Photonics YLR-200-LP* ytterbium fibre laser yielding up to 200 W. The laser is elliptically focussed and intersected with its own retro-reflection after a polarisation shift of 90°, creating a trap with a depth of up to 1.5 mK. The CBODT is used to evaporatively cool down the molecules into degeneracy, such that we are left with approximately 100 000 molecules at several 10 nK. The trap depth is controlled by regulating the power of the laser with a digital feedback loop. Due to the elliptical focussing, the trap is effectively 'flattened', facilitating the transfer into subsequent two-dimensional traps. For the same reason, the possibility of modulating the position of the trap by two crossed accusto-optical modulators (AOMs), creating an effective time-averaged potential, was implemented. More details on the CBODT may be found in [Boh12] and details on the evaporation scheme are given in [Rie15b].

2D Standing wave trap

At the final step of the evaporation in the CBODT, a molecular BEC has been created, however in three dimensions. In order to reach the quasi-2D regime, the molecules have to be transferred into a single layer of a standing wave trap (SWT).

The quasi-2D regime is reached as soon as all excitations in one of the dimensions are effectively frozen out. This may be achieved by significantly increasing the confinement in one dimension, leading to a large aspect ratio $\omega_x, \omega_y \ll \omega_z$ in this direction, such that all energy scales are much smaller than the first excited state in the z-direction. Here, $\omega_{x,y,z}$ denote the trapping frequencies in the respective directions, and the z-direction is defined to be the direction of strong confinement. The energy scales to be considered are the chemical potential μ, the thermal energy $k_B T$, and in addition the respective interaction energy E_{int}. For zero temperature and neglecting interactions, the simple criterion

$$n_x \hbar\omega_x + n_y \hbar\omega_y < \hbar\omega_z \tag{4.1}$$

leads to the expression for the maximum particle number per spin state of

$$N_{crit} = \frac{1}{2}\frac{\omega_z^2}{\omega_x \omega_y}, \tag{4.2}$$

illustrating the requirement of high aspect ratios. Further efforts of ensuring 2D conditions are described below in some more detail.

The laser creating the CBODT is required to provide high power and thereby deep traps, while a good monochromaticity is not crucial. On the contrary, all two-dimensional traps rely on interference and any fluctuations in wavelength would lead to heating due to fluctuations in the trap geometry. On the other hand, the atoms are already cold when loaded into the 2D traps, such that the requirements for trap depths and therefore the laser power are not that strong. For this reason, both the SWT and the lattice trap use a *Nufern SUB-1174-22* 50 W fibre amplifier, seeded by a low-noise continuous wave single frequency 1064 nm *Innolight Mephisto-S 500 NE* laser showing good noise characteristics [Nei13].

The SWT is created by two elliptically focussed laser beams intersecting and interfering under an angle of around 14° in the vertical plane. This produces a vertical interference pattern with a spacing of approximately 4.4 µm. This spacing is large enough to be able to fill only a single interference maximum from the ODT. Tunnelling between different layers is due to a harmonic oscillator length $l_z \approx 490\,\mathrm{nm}$ completely suppressed. The trap frequencies, including the contribution from the magnetic saddle field, are measured to be

$$\begin{aligned}
\omega_x &= 2\pi \cdot (23.22 \pm 0.06)\,\mathrm{Hz},\\
\omega_y &= 2\pi \cdot (21.04 \pm 0.07)\,\mathrm{Hz},\\
\omega_z &= 2\pi \cdot (6.95 \pm 0.06)\,\mathrm{kHz},
\end{aligned}$$

corresponding to a critical molecule number $N_{crit} \approx 50\,000$, according to equation 4.2. The trap depth is around 500 nK at a laser power of around 3 W.

The mechanical set-up was carefully designed to allow for good interferometric stability, as described in detail in [Boh12, Nei13]. With passive stabilisation, such as encasing the interferometer set-up, a phase drift of $\leq \frac{\lambda}{8}$ over 6 days was measured.

The transfer into a single layer of the SWT is achieved by modulating the ODT trap as mentioned above, such that the aspect ratios of ODT and SWT match better, and subsequently overlaying the two traps. It is not possible to resolve the different layers of the SWT with our imaging setup, thus single layer occupation is probed by means of a RF tomography measurement[3] described again in [Nei13] and [Rie15b]. It is possible to achieve a filling fraction of at least around 90 % in the central layer.

It is important to verify staying in the 2D regime at all times. For the limiting case of weakly interacting fermions at 1400 G, this is done as presented in [Rie15b]. The axial Gaussian width of the cloud after a short time of flight of 3 ms is measured. As long as in axial direction only the ground state is populated, the axial cloud width after TOF is independent of the particle number. As soon as higher trap levels are occupied, the width increases and becomes particle number dependent. By this method, a limit of $N_{crit} \approx 50\,000$ is obtained. Note that a similar method is not possible for stronger interactions, since independent time evolution of the fermions may no longer be assumed. Nevertheless, the obtained N_{crit} is still a valid lower bound, since stronger attractive interactions only lead to occupations of lower lying energy levels. In addition,

---

[3] In simplified terms, the transition frequency between state $|2\rangle$ and $|3\rangle$ is made spatially dependent by an additional magnetic field gradient. Then, transitions between these states are driven by a RF pulse while scanning its frequency.

it has been estimated that additional thermal effects for all temperatures investigated lead to occupations in excited axial trap levels on the one percent level at most [Rie15b].

Optical lattice traps

For the lattice trap, similar requirements concerning interference and laser noise stability have to be met as for the SWT. Therefore, the same combination of fibre amplifier and seed is used for both trap set-ups. A 2D optical square lattice is obtained by superimposing the SWT with two pairs of retroreflected laser beams in the horizontal plane with a relative angle of 90°. In each lattice arm, the incoming and the retroreflected lattice beam interfere under a shallow angle close to 180°, resulting in a standing wave with spacing of $d = \frac{\lambda}{2\cos\phi} = 536\,\mathrm{nm}$. To avoid interference between the two lattice arms and the SWT, the polarisation of the lattice arms is rotated by 90° with respect to each other, while the frequency of the SWT is shifted up by 100 MHz and the frequencies of the two lattice arms are shifted up by 120 MHz and down by 110 MHz, respectively. Note that the polarisations of the SWT and the lattice arm separated by 210 MHz coincide, while the polarisation of the lattice arm close in frequency is shifted by 90°.

Apart from one additional half-wave plate, the two lattice arms are identical. The lattice beams are again elliptically focussed, such that the vertical focal size in the experimental chamber is reduced. Although this reduces the vertical confinement, it is strong enough nevertheless, as it is mostly given by the SWT. The lattice is loaded by adiabatically ramping up the power in the lattice beams within several 10 ms. More details on the lattice setup are presented in [Bec13] and [Bay15], where in addition the calibration of the lattice setup is described in detail.

4.2.5 Matter wave focussing

In general, the systems prepared are probed by measuring either the in-situ density or momentum distribution. An approximation to the momentum distribution is obtained in a typical time of flight experiment. At time $t = 0$, the cloud is released from all traps and the interactions are quenched. The classical trajectory of a particle is then given by

$$x(t) = x_0 + p_0 \cdot t, \tag{4.3}$$

where x_0 and p_0 indicate the in-situ position and momentum. After an - in principle - infinitely long TOF, where the initial position x_0 is negligible, the measured position directly corresponds to the initial momentum[4]. In contrast, when the cloud is released into a harmonic potential with frequency ω, the classical trajectory is given by

$$x(t) = x_0 \cos(\omega t) + \frac{p_0}{m\omega} \sin(\omega t) \tag{4.4}$$

---

[4] This may be compared to wave optics, where different spatial frequencies separate in the far field.

and consequently a mapping of momentum and position is possible already at a finite TOF, i.e. a quarter of the trap period at $t = \frac{2\pi}{4\omega}$[5]. The principle is illustrated in a phase space representation in figure 4.3. It is shown in [Mur14] that this simple classical picture directly translates into a quantum mechanical one, now called matter wave focussing. Thus, by making use of the residual $\omega = 2\pi \cdot 12.1\,\mathrm{Hz}$ harmonic magnetic trapping frequency of the offset fields after a time of flight of around 21 ms, the momentum distribution is mapped onto real space. During time of flight, the interactions are quenched by two mechanisms: First of all, the cloud expands quickly in vertical direction due to its tight confinement. This strongly reduces the interactions by rapidly lowering the density. Furthermore, in some applications, the magnetic field may be quickly ramped (within around 150 µs) to below 600 G where the lithium gas is only weakly interacting. The latter mechanism projects the cloud onto deeply bound molecules and thus cannot be used in all situations.

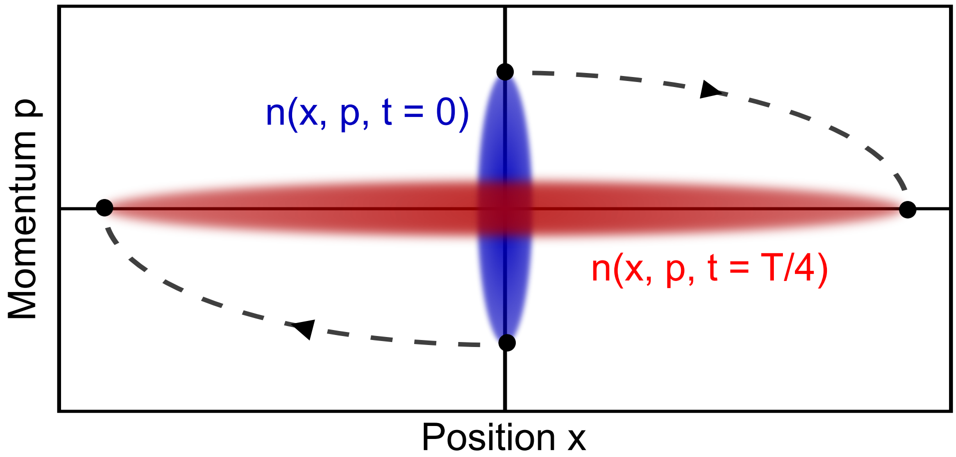

Figure 4.3: Mapping between momentum and configuration space after a TOF of a quarter period in a phase space representation. The dashed line indicates the trajectory of a (classical) non-interacting particle in a harmonic potential. In blue and red, the initial phase space distribution $n(x, p)$ at $t = 0$ and the distribution after a quarter trap period are shown. Adapted from [Mur14].

4.3 Imaging

In the previous section, the creation and manipulation of an ultracold sample of ^{6}Li atoms was explained. What is required in addition is a method to probe the system. This is

---

[5] In optics, the harmonic potential would correspond to a lens, where the focus is brought from infinity to a finite focal length.

done by imaging the atom cloud. The current set-up allows for two different imaging methods. Fluorescence imaging, where the cloud is illuminated by a resonant laser beam and the re-emitted photons are collected at a different axis, was for this thesis merely used for diagnostics. The primary imaging method is absorption imaging, where again the cloud is illuminated by a resonant laser beam, but this time the 'shadow' of the cloud is recorded on the laser axis. Absorption imaging is possible in all four optical axes of the experimental chamber, but for probing a two-dimensional gas, mostly the up-down imaging is used.
During the course of this thesis, a setup and procedure allowing the imaging of both spin states quasi-instantaneously was implemented.
All imaging techniques used in our experiment are destructive and thus the experimental cycle has to be repeated for each single image.

4.3.1 Absorption imaging

The idea behind absorption imaging is quite simple: A sample is illuminated by a laser beam resonant to some internal transition (here it is the D_2 line) of one of the spin states and part of the light is absorbed by the cloud. Therefore, the intensity reduces according to Lambert-Beer's law

$$\frac{dI}{I} = -n(z)\sigma(I)dz, \tag{4.5}$$

where $n(z)$ is the particle density and $\sigma(I)$ the cross section with an intensity dependency on resonance given by

$$\sigma(I) = \sigma_0 \frac{1}{1+\frac{I}{I_{sat}}}. \tag{4.6}$$

In the above formula, $\sigma_0 = \frac{3\lambda^2}{2\pi}$ is the bare scattering cross section for a closed transition at wavelength λ and the saturation intensity I_{sat} is given by $I_{sat} = 25.4\,\mathrm{W\,m^{-2}}$ for ^{6}Li [Geh03].
For very low imaging intensities, saturation of the transition is negligible and with $\sigma(I) = \sigma_0$, equation 4.6 is integrated to be

$$I(z) = I_0 e^{-\sigma_0 \int n(z)dz}. \tag{4.7}$$

Therefore, the column density $n(x, y)$ of a sample is obtained by measuring the intensity $I_t(x, y)$ transmitted through the cloud as well as the intensity of the laser without any atoms $I_0(x, y)$ via

$$n(x, y)\sigma_0 = -\ln \frac{I_t(x, y)}{I_0(x, y)}. \tag{4.8}$$

In practice, the intensities are corrected by dark counts and the reference image is taken within 5 ms in order to cancel out any imaging relics such as interference fringes caused by the imaging optics, which vary on moderate time scales. In order to have a reasonable signal-to-noise ratio for low column density samples, it is however favourable to increase the intensity to roughly the saturation intensity. In this case, corrections to the above formula have to be taken into account and more generally

$$n(x,y)\sigma_0^* = -\ln\frac{I_t(x,y)}{I_0(x,y)} + \frac{I_0(x,y) - I_t(x,y)}{I_{sat}^*} \tag{4.9}$$

applies. Note that the cross section and the saturation intensity have been replaced by effective values σ_0^* and I_{sat}^*, which have to be calibrated individually. I_{sat}^* may differ from the literature value among other reasons due to imperfections in the laser polarisation or a not fully closed or additionally broadened transition [Rei07]. On the other hand, σ_0^* differs from its literature value as soon as the atoms are bound to molecules, effectively reducing the cross section.

For imaging, a beat offset locked *Toptica DL 100* diode laser is used and the images are recorded, with a magnification of slightly above two, on an *AVT Stingray F-145B* CCD camera.

4.3.2 Two-state imaging

With the absorption imaging technique described above, one of the two spin states can be imaged. The full information available on the system is however only recorded by imaging both spin states. In situations where the spin degree of freedom is of no interest, the imaging of both states leads to an increased statistics, while for example for spin-spin correlations, information on both states is essential. The crucial requirement for two-state imaging is that both spin states have to be imaged quasi-instantaneously. This means that the time delay between the two images has to be much smaller than all relevant dynamical time scales, which are the expansion of the cloud during TOF (given by the magnetic trap frequency and the typical momentum scale of the gas, i.e. the Fermi momentum[6]) and the distortion of the cloud due to imaging of the other spin state (given by the momentum transfer during imaging). For our system and parameters, time scales up to a few 100 µs may be considered quasi-instantaneous. To achieve quasi-instantaneous imaging of two hyperfine states, two main requirements have to be met:

- The laser resonance frequency has to be ramped quickly and in a controlled way between the two resonance frequencies being separated by around 80 MHz.

- The camera has to be able to take two images in quick succession.

---

[6] Typical Fermi momenta are given by $p_F = \hbar k_F = 3\times10^{-28}\,\mathrm{kg\,m\,s^{-1}}$ to $4\times10^{-28}\,\mathrm{kg\,m\,s^{-1}}$.

The latter requirement is met by the so-called interline transfer mode of the CCD chip. In normal mode, the camera has a maximum image acquisition rate of 16 Hz, which is of course much too slow. However, the CCD array is build in such a way that only in every second line of the sensor, pixels are illuminated during image acquisition, while every other line is protected by a light-tight mask. Subsequently, instead of reading out the whole chip, only one line is shifted and the previously light-protected pixels are illuminated. Afterwards, the chip is read out normally [And]. This allows for taking two images within approximately 100 µs. More details on the implementation of the interline transfer mode into the experiment may be found in [Ste16].

The frequency of the imaging laser is controlled by a beat offset lock. This means that a small fraction of the laser intensity is branched off and its frequency down converted by mixing it with a reference laser. The resulting RF difference signal is detected on a photodiode and again mixed with an electronic offset frequency source. As before, only the difference frequency is considered and kept constant by a digital PID feedback controlling the error signal, which is obtained by mixing the signal with an - apart from an additional phaseshift - identical copy of itself. In such a setup, the laser frequency is controlled by the RF offset frequency. Here a Direct Digital Synthesiser (DDS) is used to implement the two-state imaging. As described in [Ste16], it is programmed to produce nearly arbitrary frequency sequences. In particular, this is a ramp between the two resonance frequencies of the ^{6}Li hyperfine states within less than 100 µs and an additional Doppler compensation ramp. The latter ramp significantly increases our detection efficiency, since during a usual imaging time of 8 µs, the atoms are accelerated by photon recoil and typically obtain a Doppler shift in resonance frequency of around 10 MHz. This shift is accounted for by adapting the imaging frequency accordingly during imaging by the mentioned additional ramp.

A fast control of the DDS frequency is only meaningful if the laser is capable of adapting its frequency on this time scale. This is achieved by splitting up the feedback signal of the digital PID signal into a low and a high frequency part. The low frequency part is fed into a Piezo element controlling the cavity size of the laser. The response of the Piezo is limited to frequencies below approximately 10 kHz. Therefore, the high frequency part is directly given to the current control of the diode laser capable of much faster response. Since the laser was solely controlled by the piezo element up to now, this has the side effect of a reduced laser line width as well.

5 Imaging and noise characterisation

All results presented in this thesis are obtained by analysing absorption images of two-dimensional atomic clouds. Especially because we want to perform high precision measurements on very dilute clouds (with a column density of around $1\,\mu\mathrm{m}^{-2}$), it is in general important to optimise the signal-to-noise ratio of the imaging process. On the contrary, for the application of noise correlation measurements, the atomic noise is the signal. Therefore, it has to be ensured that the contribution of atomic noise is large compared to all other noise sources. These considerations motivate a proper imaging and noise characterisation. Furthermore, it is also crucial to know the atomic density on an absolute scale for the following reasons: The atomic noise scales non-linearly with the atom density. This is directly obvious for the simplest case of Poissonian density noise of (extremely) dilute thermal gases, but holds more general for other noise scalings as well. Thus, noise characterisation goes hand in hand with a density calibration[1]. Furthermore, the density directly relates to the 2D scattering parameter $\ln(k_f a_{2D})$ via the (local) Fermi wave vector, such that only with a density distribution known on an absolute scale, any 2D phase diagram may be mapped out. Thus, also the camera properties, in particular its gain and quantum efficiency, have to be known exactly in order to translate camera counts into intensities.
In this chapter, first of all the most important camera properties are summarised and the imaging calibration is explained. Thereafter, the imaging noise is studied in some detail, with the application for noise correlation measurements already in mind.

5.1 Camera characteristics

For this thesis, an *ATV Stingray F-145* CCD camera is used for taking absorption images. Its properties are summarised in table 5.1, where the values for gain, quantum efficiency and readout noise are measured for this specific camera as described in [RMP16], while all other characteristics are according to the manufacturer. The readout noise is on the level of nine electrons. For typical absorption images, this is a significant, but far from limiting, noise contribution. All other technical noise contributions, as for example thermal noise, are negligible for the purposes described here. The imaging system has a magnification of 2.14 such that the effective pixel size is $3.01\,\mu\mathrm{m} \times 3.01\,\mu\mathrm{m}$.

---

[1] In principle, it is even possible to use the noise behaviour for the purpose of a density calibration if the exact noise scaling is known, as it is for example for a (hot) thermal gas.

Property	**Value**
Resolution	$1388\,\mathrm{px} \times 1038\,\mathrm{px}$
Pixel size	$6.45\,\mu\mathrm{m} \times 6.45\,\mu\mathrm{m}$
Dynamic range	14 bit
Quantum efficiency	0.373 ± 0.03 (stat) $\pm\, 0.012$ (sys) (@ 671 nm)
Gain	$(0.3206 \pm 0.0002)\,\mathrm{e}^-/\mathrm{ADU}$
Readout noise	$8.7\ e^-$

Table 5.1: Specifications of the *ATV Stingray F-145* CCD camera.

With the gain and the quantum efficiency known, counts on the camera can be directly translated into intensities. With an additional calibration of the saturation intensity, as described in the next section, these intensities then allow for density determination with the (extended) Lambert-Beer formula. For all measured intensities it is important, however, to include an additional (measured) transmission factor of 77 % of the optics between the experimental chamber and the camera.

5.2 Imaging calibration

With the camera characterised, the intensities of absorption and reference image are known. However, to obtain the column density with the extended Lambert-Beer formula (equation 4.9), the effective saturation intensity and the effective cross section remain to be calibrated. To this end, it is assumed that the intensity of the imaging beam is constant within the extension of the atom cloud such that the saturation intensity may be calibrated position independent. For the calibration, atom clouds in the $|1\rangle - |3\rangle$ mixture with a fixed, but a priori unknown, atom number are prepared, and the state $|3\rangle$ imaged with different known intensities of the imaging laser. Assuming the calibration factor α, defined by

$$I^*_{sat} = \alpha \cdot I_{sat}, \tag{5.1}$$

to be known, the obtained optical density $n \cdot \sigma_0^*$ has to be independent of the imaging intensity. Therefore, α is chosen such that the standard deviation of the optical density $n \cdot \sigma_0^*$ in the middle of the cloud, measured for different intensities, is minimised. This is illustrated in figure 5.1. The resulting calibration factor is given by $\alpha = 1.08 \pm 0.06$. The error is estimated by considering the values for α where the obtained optical density increases or decreases monotonously with the imaging intensity. Contributions to the error may originate from a non-homogeneous imaging intensity and additional technical artefacts, as for example interference fringes. The effective saturation intensity is quite close to the literature value as anticipated for a (to very good approximation) closed and

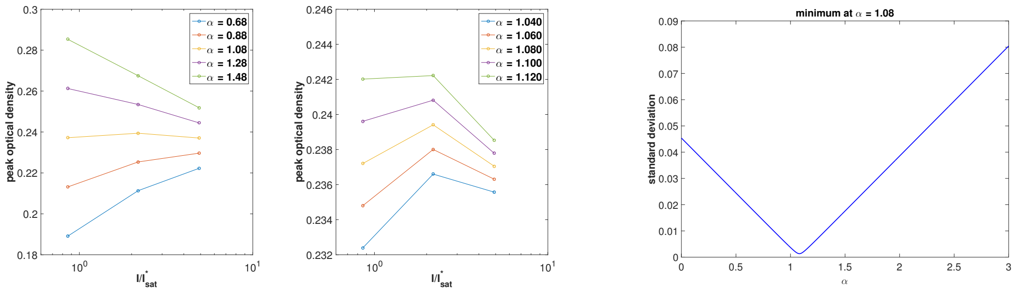

(a) Peak optical densities

(b) Standard deviation

Figure 5.1: Calibration of the effective saturation intensity. An atomic cloud is imaged at different intensities with otherwise fixed parameters. For the best calibration factor α, the optical densities are expected to be independent of the imaging intensity. In (a), the optical densities in the middle of the cloud are shown for different values of α. While there are some small systematic errors, a best calibration value of $\alpha = 1.08$ may be obtained by minimising the standard deviation between the different intensities as shown in (b).

polarisation insensitive optical transition at still moderate imaging intensities.
The calibration up to now is only valid for the third hyperfine state, especially since the optical transitions of the other two experimentally available spin states are not fully closed. Thus, without additional calibration, the measured densities appear lower for these states, since after absorbing an imaging photon, the atoms decay with a significant probability (around 1 % [Bec16]) into a dark state of the system and therefore cannot absorb any further photons. Nevertheless, in figure 5.2 it is shown for the example of the first spin state that it is sufficient to rescale the intensity of the absorption image by a factor given by the total loss into the dark state during the image acquisition time. The same figure illustrates furthermore also the validity of our two-state imaging protocol. For the measurements shown here, a spin-balanced (2D) gas after a fixed TOF is prepared. Thus, the density profiles of both spin states are expected to be identical. However, after imaging the first spin state, the second spin state keeps evolving and may be influenced by scattering processes with the first (now - after imaging - strongly accelerated) state. For this reason, the second spin state has to be imaged quasi-instantaneous, that is, much faster than all the processes described above. Here, around 130 µs lie between the two images[2]. Figure 5.2 shows that the assumption of being quasi-instantaneous is for this delay well fulfilled, as the density profiles are (after the dark state correction) almost identical. A more detailed analysis shows, that the Gaussian width of the clouds varies at most on a 2 % level.

---

[2] To be compared for example to typically 20 ms TOF.

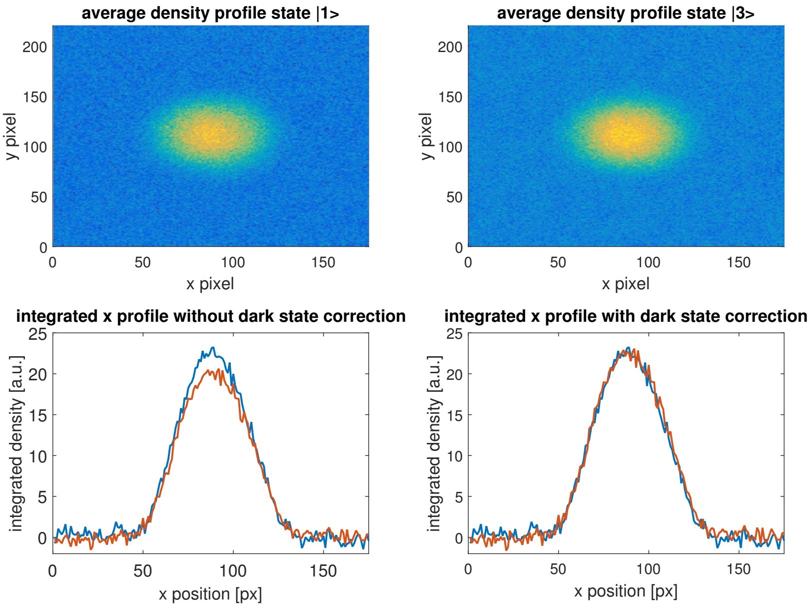

Figure 5.2: Validation of the correction method for dark state losses and the two-state imaging protocol. In the top row, averaged images of the third and first spin state in a spin-balanced gas are shown. The different spin states are imaged within 130 µs. The bottom row shows the integrated density profiles in x-direction before (left) and after (right) correcting the intensities of the absorption images for dark state losses. These profiles show that the contribution of the dark state losses is significant but can be reliably corrected for.

As a last step, the magnetic field-dependent effective cross section has been calibrated in [Rie15b] and the results for the calibration factor β with $\sigma_0^* = \sigma_0/\beta$ are quoted below in table 5.2. The calibration factors are obtained by imaging an atom cloud at a fixed atom number for different magnetic offset fields and assuming the cross section to be given by its literature value for very high magnetic fields ($\mathrm{B} \gtrsim 1000\,\mathrm{G}$).

5.3 Understanding the noise

In a noise correlation analysis, correlations in the atomic quantum noise are studied. Therefore, it is crucial to have a good understanding of all noise sources on the absorption images taken. In particular it is necessary

- to know the atomic densities and their noise on an absolute scale. For this, a

Offset field B [G]	692	732	782	≥ 812
Calibration factor	$1.33 \pm^{0.10}_{0.07}$	$1.37 \pm^{0.11}_{0.09}$	$1.06 \pm^{0.06}_{0.05}$	1

Table 5.2: Calibration of the effective cross section. An atomic cloud with a fixed atom number is imaged at different magnetic offset fields. The magnetic fields given here apply for a balanced $|1\rangle - |2\rangle$ mixture. When working with different mixtures, the calibration factors have to be adapted according to the interaction strength. Taken from [Rie15b].

proper camera and imaging calibration as described above is needed.

- to identify and - if possible - suppress all relevant noise sources except from the atomic noise.
- to find a parameter regime where atom noise is the dominant noise source.

It is important to stress the last point. All additional imaging noise sources are either uncorrelated and therefore mask the atomic correlations or, even worse, correlated in some way and therefore introduce additional spurious correlation signals. Furthermore, for two-dimensional systems, it is far from trivial to work in a regime where atomic noise dominates, since the column densities are relatively low. For these reasons, this section is dedicated to understanding the noise of absorption images.

5.3.1 Imaging noise

As stated before, the atomic density may be calculated from the measured transmission and reference images with the modified Lambert-Beer law

$$n\sigma_0^* = -\ln\left(\frac{I_t}{I_0}\right) + \frac{I_0 - I_t}{I_{sat}^*}, \tag{5.2}$$

where the effective cross section σ_0^* and effective saturation intensity I_{sat}^* are calibrated as described above. The density obtained in this way is of course afflicted with errors as well, resulting from uncertainties on the measured intensities. The interesting quantity to be compared to the atomic quantum noise later on is the uncertainty on the atom number per pixel caused by the imaging. It can be obtained by straight forward Gaussian error propagation on the above Lambert-Beer law. Note, however, that it is not valid to assume the Poissonian 'shot' noise on the intensities, but rather on the primary photo-electron number detected by the CCD, since the photoeffect has to be treated as a stochastic process as well. This means that for the photo-electron power $P = \frac{QIA\tau}{\hbar\omega_0}$, where Q is the quantum efficiency, A the pixel size, τ the integration time and ω_0 the imaging frequency, the noise is given by

$$\delta P_{0/t}^2 = P_{0/t} + \Delta_{0,t}, \tag{5.3}$$

where an additional term Δ, accounting for technical noise which is assumed to be shot noise-limited as well, was introduced. For the noise on the atoms per pixel, δn_{img}, this results in

$$\delta n_{img} = \frac{A^2}{\sigma_0^{*2}} \left[\frac{P_t + \Delta_t}{P_t^2} \left(1 + \frac{P_t}{P_{sat}^*}\right)^2 + \frac{P_0 + \Delta_0}{P_0^2} \left(1 + \frac{P_0}{P_{sat}^*}\right)^2 \right]. \tag{5.4}$$

The first term of the above expression describes the noise caused by the transmission (or absorption) image. In principle, this term could be suppressed by varying either the intensity of the imaging laser or increasing the integration time. Since in the latter case, according to this simple formula the saturation power is increased by the same factor as the transmitted power, increasing the imaging time will always reduce the noise. However, this cannot be done beyond limit for several reasons: For each photon scattered, the atoms receive a momentum kick. In horizontal direction (orthogonal to the imaging laser), this may be well approximated by a random walk and leads to a decrease in spatial resolution, while in vertical direction, the acceleration is directional and it has to be ensured that the cloud remains in the depth of focus of around 400 µm. Furthermore, the imaging frequency changes with the acceleration during imaging by 8 MHz due to the Doppler effect. This can be partially compensated, though, by linearly tuning the imaging frequency during the integration time. Additional effects that limit us in integration time are that the optical transition for imaging state $|2\rangle$ is not fully closed and therefore saturates [Bec16] as well as the general prerequisite that the imaging integration time has to be on a faster time scale than all atomic dynamics. As a tradeoff between all the limitations explained above and a noise as low as possible, usually an integration time of $\tau = 8\,\mu s$ is chosen. For this value, the random walk distance in horizontal direction of 5 µm gives a total imaging resolution of around 6 µm, and the atoms are displaced during imaging by roughly 25 µm in vertical direction, which is still well within the depth of focus.

The second term of equation 5.4 describes the influence of the reference image. Again, some improvement can be made by adjusting the intensity of the imaging laser. More importantly, in this case it is indeed possible to increase the integration time by some extent. The remaining limitations are that the imaging time has to be short enough, such that first of all, imaging relics such as interference fringes do not move significantly, and secondly, the camera does not saturate. As the influence of fringes quickly becomes limiting for an increased imaging time, we usually restrict ourselves to a factor of 1 to 4, at least partly suppressing this contribution to the noise if crucial.

In situations where we are mostly interested in the density profile of the atomic cloud, the relevant quantity characterising the imaging noise is the relative noise $\delta n/n$. This ratio is plotted in figure 5.3 as a function of the atomic density for different imaging intensities (for a reference image acquisition identical to the absorption image). In general, there are two important limits: For very low densities, only very few photons of the imaging beam are scattered and a reliable density determination is not possible. On the other hand, for very high densities, most of the imaging beam is absorbed and very few transmitted photons again result in a high noise. Especially when working at low densities, the influence of varying the imaging intensity is important as well. Similar to before, for very low intensities, too many photons are absorbed while for very high intensities, the relative change in photon number becomes too small. However, there is a large range of intensities with very similar noise ratios in the density regime considered in this thesis. Here we choose to work with an intensity of roughly 0.8 I_{sat}.

The considerations taken above are of special importance for the RF measurements

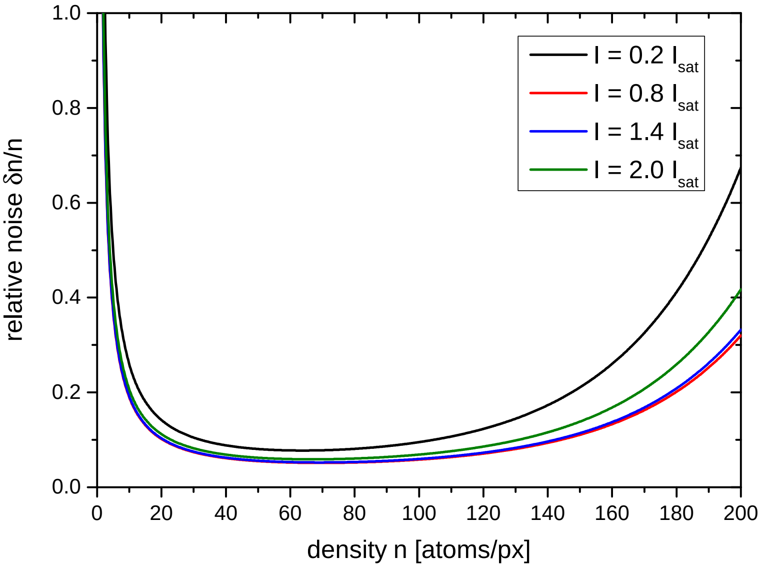

Figure 5.3: Relative imaging noise as a function of the atomic density for different imaging intensities. For both limits of very large and very small densities, the noise contribution increases because too few photons are transmitted or scattered, respectively. Furthermore, too low or high imaging intensities lead to increased noise ratios as well. For the experiments described here, imaging intensities of around 0.8 I_{sat} are used.

of pairing in the normal phase, as described later on, as here the observable is the depletion of atoms in a certain spin state by a radio frequency pulse. For noise correlation measurements, rather the absolute magnitude of the imaging noise is of relevance, as this quantity has to be compared to the atomic noise responsible for the correlations. The atomic noise contribution will be discussed in the following paragraph.

5.3.2 Atomic noise

For each pixel of the CCD, the column integrated atom number n may be obtained as described above. Since the atom number is discrete, it is natural to assume it to be Poissonian distributed. With this assumption, some first statements can be made on whether it is at all possible to observe noise correlations in our two-dimensional quantum gas. To this end, the atomic cloud is modeled by a Gaussian density distribution, normalised to the atom number, with a width dependent on the time of flight and taken from experiment. The atomic noise is assumed to be at shot noise level. The noise on the column-integrated atom number may be obtained by inverting equation 4.9 and plugging the result back into equation 5.4. Finally, it is important to specify the minimum distance of correlations to be taken into account for the result to be meaningful. It is of course desirable to take into account a region as large as possible for the analysis; however, in many situations only in the central region of the atom cloud the atomic noise has a significant contribution. For the lattice system, the relevant distance scale would be the position of the first (Bragg) correlation peak, which may be approximated to be at a radius of

$$r_{corr} = \frac{\hbar}{\lambda m \omega} \sin(\omega t), \tag{5.5}$$

in terms of the matter wave focussing frequency ω. Note that we are interested in momentum space correlations, and thus the above formula holds strictly speaking only for a TOF of a quarter of the trap period. This matter will be discussed in the following section 6.3, where noise correlation measurements for short TOFs are considered. For now, it is for simplicity assumed that the formula holds for any TOF. In figure 5.4, the atomic shot noise and the imaging noise are compared. In particular, also a typical radial noise profile (under the assumption of shot noise behaviour) for an atomic cloud of 50 000 atoms and typical experimental parameters after a time of flight of 1 ms is shown. Here, the imaging noise and the expected position of a lattice correlation peak are indicated as well. In order to observe the lattice peak in a correlation measurement, at least the shaded region has to be taken into account. In an analogue way, also a suitable region of interest for other correlation measurements may be defined.

Since the atomic noise contribution is on a similar level as the imaging noise, a significant reduction of the weight of the correlation signal is expected due to the uncorrelated imaging noise. This is especially true when working in momentum space with a density of 4 atoms/pixel to 6 atoms/pixel at most.

Up to now, it was assumed that the atomic noise is well described by shot noise behaviour.

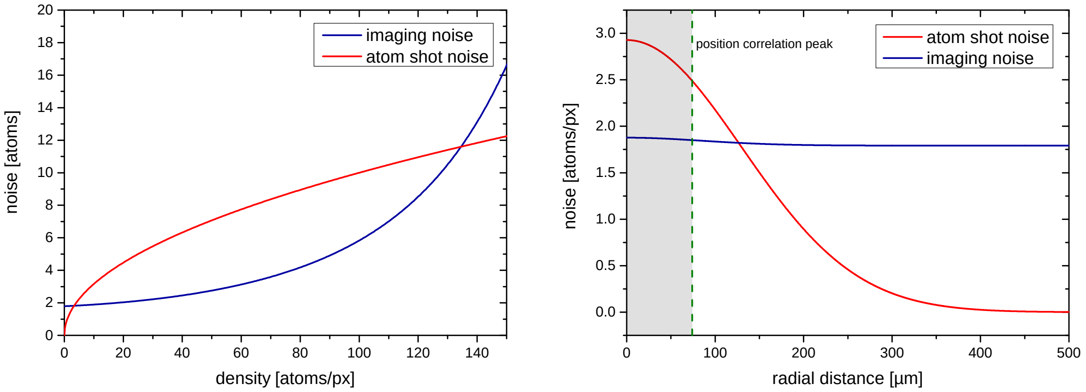

(a) Imaging and atom shot noise contribution

(b) Expected noise profile

Figure 5.4: Comparison of imaging and atomic noise contributions. In (a) the noise contributions are compared as a function of the atomic density. The atomic noise is assumed to be Poissonian distributed and is therefore given by the square root of the atom number per pixel. The imaging noise contribution is calculated according to equation 5.4 with typical experimental parameters, in particular an imaging intensity of 0.8 I_{sat} and a reference image integration time of 8 µs. It can be directly read off that for very low densities, the prerequisite of dominating atomic noise is not given. In (b) the expected noise profiles for a typical atomic cloud after a short TOF of 1 µs is shown. Indicated is the expected distance from the centre of a possible lattice correlation peak after this TOF, which gives the minimum region of interest that has to be taken into account when correlating the noise.

This is in general not completely true due to quantum statistics and interactions. Consider as an example a bosonic thermal cloud in configuration space. In the completely non-degenerate regime with weak interactions, the noise is expected to be slightly above shot noise level due to bosonic bunching. This density dependent bunching factor α_b, with $\alpha_b \gtrsim 1$, may be calculated to be [Hun03]

$$\alpha_b = \frac{-ze^{-2\beta g n}}{\left[1 - \left(1 - \frac{mg}{\pi\hbar^2}\right) ze^{-2\beta g n}\right] \ln\left(1 - ze^{-2\beta g n}\right)} \tag{5.6}$$

in terms of the fugacity $z = 1 - e^{n\lambda_{dB}}$, the interaction strength g, the density n and the unitless temperature factor $\beta = \frac{1}{k_B T}$. On the other hand, in a thermal gas with significant interactions and degeneracy, density fluctuations are expected to be strongly suppressed as discussed in subsection 2.1.5, and the noise levels lie accordingly below shot noise behaviour.

5.3.3 Experimental considerations

With a theoretical description of the expected noise at hand, in this paragraph the experimentally measured noise is presented. Quite in general, for every noise correlation analysis, the noise profile is determined as well, in order to identify suitable regions of interest for the correlations as illustrated above.

The noise profile may be obtained by two different methods: In a straightforward way, a noise map can be calculated by taking pixelwise the standard deviation over a relatively large set of images (typically 100 to 500 images). Afterwards, this noise map is averaged over equidensity lines (assuming here elliptical cloud profiles due to the slight anisotropy of the 2D standing wave trap). However, this method includes contributions from fluctuations in the total atom number as well. For this reason, also a second method can be exploited. By first taking the standard deviation over equidensity lines within every single realisation, and afterwards averaging the radial noise profiles over the set of images, noise contributions from atom number fluctuations are suppressed.

In figure 5.5, the momentum space noise profiles calculated with both methods for a bosonic cloud of around 40 000 molecules are shown. There are several qualitative features to be noticed. First of all, within the central region where there is a significant atomic density, the noise level is, as expected, higher. In regions without any atoms, a flat imaging noise floor is anticipated. The observed increase in noise towards the outer parts of the image may be explained by a reduced imaging intensity and additional imaging relics in these regions. In the region with atoms, both methods calculating the noise give compatible results, showing that the influence of atom number fluctuations is not significant. It should be be noted, however, that this is only true for these sets of images due to additional postselection, where only around 50 % of the images with a similar atom number are kept for further analysis. In regions without atoms, the method of first obtaining a density map by calculating the noise pixelwise gives a slightly lower noise level. This can be explained by the influence of interference fringes on the images, since fringes that are stable from shot to shot only have a significant contribution when calculating the radial noise profile first. Nevertheless, it is to be expected that there is some contribution from unstable fringes even in the second method.

Turning towards a more quantitative analysis of the noise, it has to be kept in mind that the total resolution of the imaging system is on the order of two pixels, and therefore the signal from each atom is significantly spread over several pixels, effectively reducing the atom noise contribution by a factor $\Theta < 1$. This noise suppression can be avoided by re-binning the images into effective pixel sizes with a size larger or similar to the resolution. Increasing the pixel area by a factor A_{bin} reduces both the imaging and the atom noise by a 'geometric' factor of $\sqrt{A_{bin}}$, with the ratio of atomic to imaging noise increasing as Θ approaches 1. The bin size is introduced in a smooth way by applying

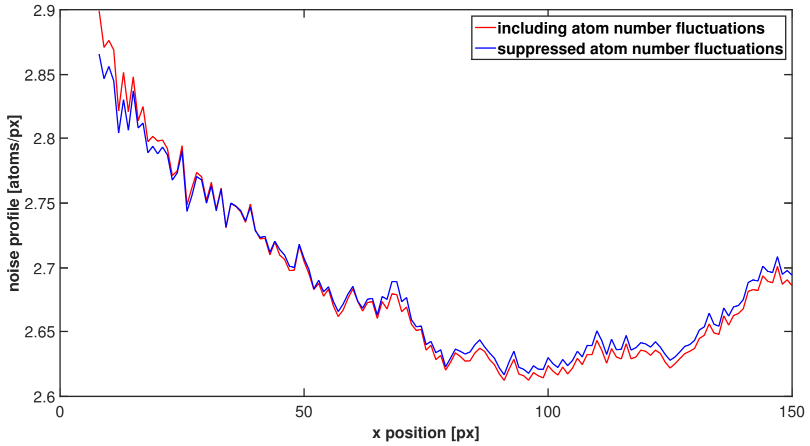

Figure 5.5: Radial noise profiles obtained by two different methods. The blue curve is calculated by first taking the standard deviation on equidensity lines for each individual image and then averaging the noise profiles over a set of images. With this method, the influence of atom number fluctuations may be suppressed at the cost of static fringes strongly influencing the noise levels. The red curve is calculated by first taking the pixelwise standard deviation over a set of images and afterwards taking the mean of this noise map over equidensity lines. This method is influenced by atom noise fluctuations and non-static fringes, but suppresses the contribution from static fringes.

a low-pass filter in Fourier space onto each individual image. Here, the low-pass part of a Butterworth band-pass filter with the functional form

$$F_{low-pass} = \frac{1}{(1 + \frac{k}{k_{low}})^{2n}}, \tag{5.7}$$

in terms of the absolute value of the momentum and the cut-off frequency k_{low}, is utilised, where the order n is chosen to be $n = 5$.

A numerical Fourier transformation shows that the effective pixel size is given by $A_{bin} = \frac{0.63}{k_{low}}$. In figure 5.6, the normalised point spread function of the filter is shown for different effective bin sizes. In addition, the noise profile of the filtered images are plotted as well. Note that for better comparability, the noise profiles are scaled up by their corresponding geometric factors[3]. As expected, the atomic noise contribution increases with an increased bin size, up to approximately 2.5 × 2.5 pixel bins, that is up to the point where the effective pixel sizes are larger than the resolution of around 6 µm.

---

[3] The geometric factors differ slightly from the naive $\sqrt{A_{bin}}$ factor due to the filter point spread function not being a step function.

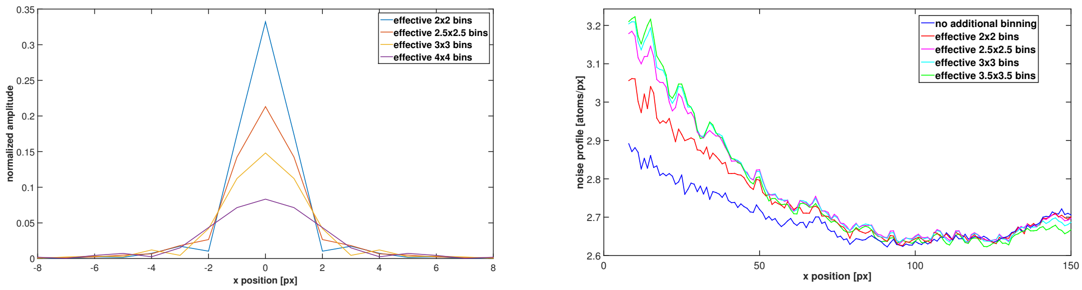

(a) Point spread function

(b) Effect of filtering

Figure 5.6: The effect of low-pass filtering. In (a) the point spread function of the filter used is shown for different effective bin sizes. The smooth filter chosen here has the advantage that the signal is smeared out mostly in the desired main maximum and only with a small fraction in side maxima. In (b) the (scaled up) noise profiles for different bin sizes are shown. Up to a bin size of around 2.5×2.5 pixels, the relative contribution increases, as expected from an imaging resolution limited to around 6 µm.

5.3.4 Measured noise profiles

With these filtering methods at hand, finally the measured noise profiles are compared to the expected profiles. In figure 5.7, the density and noise profiles are displayed for two distinct situations: Once in-situ and weakly interacting (balanced $|1\rangle - |3\rangle$ mixture at $B = 625\,\mathrm{G}$) at a temperature of $T = (90 \pm 5)\,\mathrm{nK}$, and in addition in momentum space and strongly interacting (balanced $|1\rangle - |3\rangle$ mixture at $B = 680\,\mathrm{G}$) at a temperature of $T = (140 \pm 5)\,\mathrm{nK}$ and with a four times longer reference image acquisition time. The temperatures are obtained by fitting a Maxwell-Boltzmann distribution in momentum space to the outer wings of the cloud. The error on the temperature is dominantly given by the ambiguity in choosing the exact fitting region. In particular, it is ensured that the cloud is not superfluid.

The measured noise profiles are compared to the theoretical expectations. To this end, the cloud shape is extracted from the density profiles by fitting a phenomenological model given by the sum of two Gaussians. Subsequently, the density is converted with the measured intensities into expected noise levels. It may be noted that first of all, the imaging noise floor is, as expected, lower for the longer reference image integration time. However, an additional noise source of 2.9 atoms/pixel and 1.83 atoms/pixel had to be quadratically added in the case of the in-situ and momentum space noise profiles, respectively, to raise the theoretical noise level to the observed ones. The additional noise can be attributed to parasitic (interference) structure on the images and the higher contribution for the smaller interaction strength is expected, as the smaller cross section in this case (see table 5.2) leads to an increased influence of the fringes. In both images, the expected total noise is indicated in blue. For the in-situ profile, the bunching factor introduced above is included. In both cases, the observed noise lies significantly below the expected one. For the in-situ distribution, the difference is (apart from the central part) on the few percent level and may be explained by suppressed density fluctuations in the degenerate limit at ultracold temperatures. In addition, a slightly wrong calibration of the effective cross section would have a similar effect. The above arguments, however, can not explain the reduced atom noise in momentum space, where the discrepancy is much larger in addition.

While a full description of the noise observed is not possible, the measured and expected noise levels nevertheless provide a measure for the feasibility of noise correlation measurements in 2D geometries, as in regions with a strongly suppressed atomic noise, also noise correlations are expected to be substantially reduced.

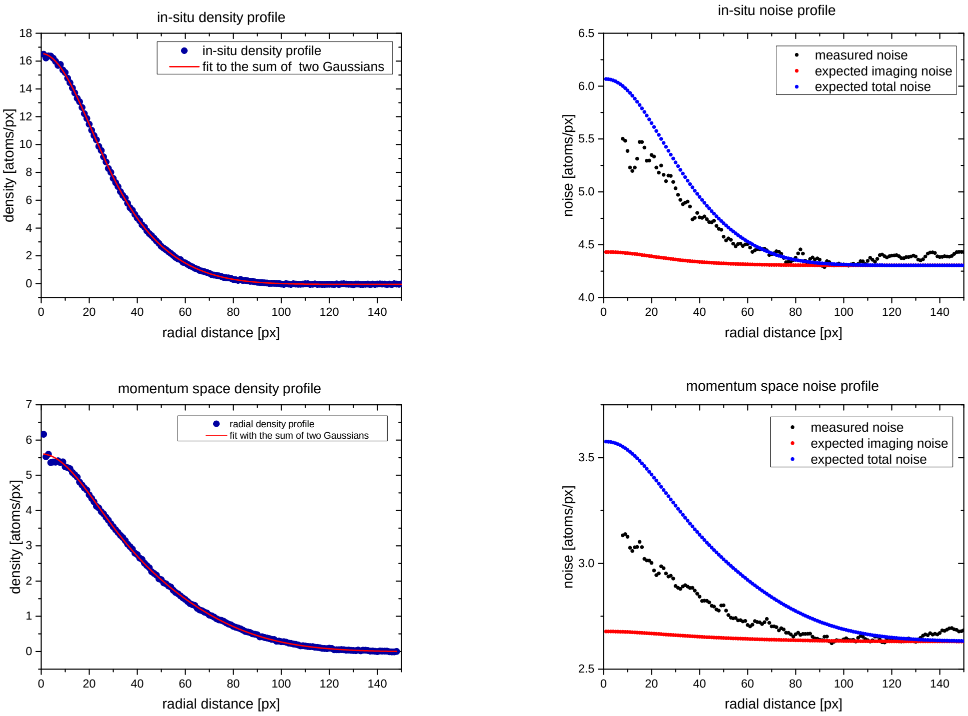

Figure 5.7: Measured density and noise profiles compared to expectations. In the upper line, the results for a weakly interacting spin-balanced gas in the $|1\rangle - |3\rangle$ mixture at $B = 625\,\mathrm{G}$ and a temperature of $(90 \pm 5)\,\mathrm{K}$ measured in-situ are shown. The left hand side shows the obtained density profile with a fit to a phenomenological model given by the sum of the Gaussians. The right hand side shows the measured density profile in black, the expected imaging noise including an additional contribution of 2.9 atoms/pixel in red and the expected total noise including a bunching factor in blue. The deviations from the expected noise level may in principle be explained by the suppression of density fluctuations of a degenerate Bose gas. In the lower line, the results for a strongly interacting spin-balanced gas in the $|1\rangle - |3\rangle$ mixture at $B = 680\,\mathrm{G}$ and a temperature of $(140 \pm 5)\,\mathrm{K}$ measured in momentum space are shown. Again, the density profile and the different contributions to the noise are shown. This time, an additional noise of 1.83 atoms/pixel had to be added. Again, the atomic noise contribution is significantly lower than expected.

6 Noise correlation measurements

In this chapter, the applications of a noise correlation analysis for probing density coherence in an ultracold quasi-2D quantum gas are discussed. In particular, the cases of a bosonic bulk gas above the critical temperature for superfluidity and a thermal gas in a lattice trap are considered. As this thesis is aimed at establishing a general 'toolbox' for identifying various low-temperature states and phases, also the possible applications to systems which are, as of now, not yet realised in our experiment are discussed. Furthermore, the general procedure of the analysis method is sketched at the beginning of this chapter.

6.1 General procedure

This section gives a brief overview over the different steps needed in a noise correlation analysis.

Identifying parameters and taking data In chapter 3, it was motivated that correlations in the density show up as fluctuations in the momentum distribution. Therefore, it is desirable to obtain the true momentum distribution and to this end image the atomic cloud after an appropriate TOF. However, it is important to identify the relevant correlation length scales and ensure a sufficient atomic density (in momentum space) at these scales. For example for the lattice trap used in this experiment, the correlation length in true momentum space is on the order of 1 mm with the typical cloud width one order of magnitude smaller. In these cases, it is necessary to abandon the notion of true momentum space and work at shorter TOFs. The implications have to be checked from case to case, as will be done for the lattice system in the following section 6.3.
After identifying a suitable parameter range, a data set of typically around 500 images is taken and converted into density maps. Such a large image set allows for a strict postselection.

Postselection There are two contributions to the g_2-correlation map: Firstly, those are correlations in the noise of the images that encode the density coherence. In principle, they are present in every single image; however, since they have typically very small amplitudes, an averaging process over many images is necessary to reveal the correlations. Secondly, there are also correlations from the overall cloud envelope. In the ideal limit, where the envelope is exactly the same in every image, its contribution is cancelled out by the normalisation. However, if the envelope changes slightly from shot to shot or non-stable fringes are present, this leads to additional correlation. The same is true for fluctuations in the total atom number.

In general, smooth density variations lead to positive correlations if all derivatives of the density profile have the same sign along the direction of motion, and correspondingly negative correlations when the derivative changes sign. Therefore, a Gaussian cloud moving between the images introduces negative correlations, while a cloud changing its width leads to positive correlations. In addition, a fluctuation in atom number introduces a (to first order) constant offset in the g_2-function. The influence of the cloud fluctuations will be discussed in the following section 6.2.

The parasitic correlations described above may be partially suppressed by carefully centering the images and applying furthermore a strict postselection, keeping only a small subset of typically around 50 images with similar envelopes for the further analysis.

Fourier space filtering In some situations, it is advantageous to apply a (Fourier space) Butterworth band-pass filter on the individual images prior to the calculation of the correlations. It has the functional form

$$F_{butterworth} = \frac{1}{(1+\frac{k}{k_{low}})^{2n}} - \frac{1}{(1+\frac{k}{k_{high}})^{2n}}, \tag{6.1}$$

where k_{low} and k_{high} are the high- and low-pass cutting frequencies and n, chosen again to be $n = 5$, is the order of the filter. As before, the low-pass filter part is included for effectively increasing the bin size. With the additional high-pass filter, low-frequency contributions as for example the cloud envelope may be suppressed. When applying a Fourier space filter, it always has to be ensured that only frequencies well separated from those contributing to the actual noise correlations are cut. Thus, in some situations, it is necessary to replace the high-pass filter by a fit-subtraction protocol, where the envelope functions are fitted to some model and then subtracted.

Calculating the noise and selecting a region of interest At this point, the noise profiles may be calculated and analysed as illustrated in the last section. Together with the expected correlation distance, they allow for a selection of a proper region of interest for the further analysis.

Calculation of the correlation map In the last step, the g_2 noise correlation function is calculated by evaluating

$$g_2 = \frac{\langle ACF(I_1 \cdot I_2)\rangle}{ACF(\langle I_1\rangle)\,\langle I_1\rangle}, \tag{6.2}$$

where ACF denotes the autocorrelation function and $I_{1/2}$ are the images of the two states in momentum space to be correlated (this might be the same or a different spin state) with their 2D indices suppressed. The average is taken over the set of several realisations. The g_2-function as defined above is a function of the difference in momentum $g_2 \equiv g_2(\vec{p}-\vec{p'})$. For a typical inhomogeneous system, therefore a trap averaged correlation function is calculated. This may be avoided, when needed, by correlating only certain momenta. For example, it is possible in a straightforward manner to define a radial correlation function as well.
A direct calculation of the autocorrelation functions of images with N_P pixels includes $\mathcal{O}(\frac{1}{8}N_P^2)$ multiplications, and thus is assosiated with a considerable time effort for large regions of interest. The numerical effort can be somewhat reduced by considering the Wiener-Khinchin theorem, which states that the autocorrelation function is given by the inverse Fourier transform of the product of the individual Fourier transforms of I_1 and I_2. To this, end a zero padding, required by the Fourier transform algorithm, has to be included, such that calculating the autocorrelation function in this way results in $\mathcal{O}(4N_P \cdot \log(4N_P))$ multiplications and can be considerably faster.

6.2 Correlation analysis in a thermal bulk gas

In this section, the application of noise correlation measurements in a 2D thermal bulk gas close to the critical temperature for superfluidity is studied. While the physics of a two-dimensional thermal gas are already well understood, it is nevertheless interesting to study such a system for several reasons:

- Thermal gases can provide a test ground for studying noise correlations, especially since it is possible to suppress the correlations by driving the transition into a superfluid with phase coherence but without density coherence.
- It is experimentally possible to tune the system smoothly from being effectively bosonic to fermionic. Therefore, the transition from bosonic bunching to fermionic anti-bunching may be studied.
- Starting from a bulk system below the temperature marking the onset of pairing (the critical temperature for superfluidity or the crossover temperature for pairing), pairing may be studied by recording spin-spin correlations.

In the following, the feasibility and the limitations of the analysis steps proposed above are discussed.
Consider first the case of a thermal gas, with all correlation length scales (these are in particular the thermal de Broglie wavelength and the healing length) smaller than the inter-particle distance. Such a system constitutes the direct analogy to the original star interferometer developed by Hanbury Brown and Twiss, with the addition that not

only bosonic bunching, but by considering a fermionic gas also anti-bunching, may be studied. As the only scale setting the coherence length is the geometric size of the cloud, the observed correlation length in momentum space is inversely proportional to the cloud size. For our matter wave focussing system and a Gaussian cloud with width σ_{cloud}, this length scale σ_{corr} would be given by

$$\sigma_{corr} = \frac{\hbar}{\sqrt{2}\sigma_{cloud}} \frac{1}{m\omega_{mag}}, \tag{6.3}$$

where m is the mass of ^{6}Li or the ^{6}Li$_2$ molecule, and ω_{mag} the magnetic 'lens' frequency during the TOF. For a typical cloud width of 50 µm to 150 µm, the correlation length is on the 1 µm scale, and therefore smaller than the resolution and pixel size of our imaging system and thus not observable. Such direct 'HBT' type correlations for bosons and fermions have been observed however in ^{3}He and ^{4}He in [Jel07].

In order to observe correlations in our system, coherence on different length scales has to be present in the gas. These scales are in particular given by the interaction energy in form of the healing length, setting the scale above which density fluctuations are suppressed, and the thermal energy in terms of the thermal de Broglie wavelength, setting the scale of phase coherence in the system. Both scales are on the order of 1 µm, resulting in a correlation length on the order of 50 µm which could be observable. To this end, a bosonic thermal gas in the $|1\rangle - |3\rangle$ at around 150 nK is prepared and imaged in momentum space. There are two parameters scanned: Using the magnetic offset field, the interaction strength is varied. Both a system at $B = 630\,\mathrm{G}$, and thus weakly interacting ($a_{3D} \approx 1700\ a_0$), and strongly interacting at $B = 680\,\mathrm{G}$ ($a_{3D} \approx 19500\ a_0$) is realised. For the latter case, after releasing the cloud from the trap, the magnetic field is quickly ramped to $B \lesssim 600\,\mathrm{G}$, where the molecules are only weakly interacting, to avoid momentum redistribution during TOF. Furthermore, the temperature is varied in the range from 130 nK to 154 nK by first preparing the lowest temperature and then placing excitations in the z-direction by resonant shaking of the SWT. During a 1 s wait time, these z excitations are scattered back into pure radial excitations and thermalise, thus increasing the temperature. In figure 6.1, the g_2-map and the radial g_2-profiles for the strongly interacting system at a temperature of 140 nK are shown. The corresponding noise profile was already presented in figure 5.7. Note that it is refrained from using any Fourier space filter here, as the correlations are expected to show up on the few pixel scale. In the g_2-map, a clear autocorrelation peak is visible as each pixel is perfectly correlated with itself. This zero pixel peak will be excluded from further analysis. In addition, there are positive correlations at small momenta. This is visible more directly when looking at the radially averaged profiles. On a scale of around 15 pixels, there are positive correlations. These would correspond to a length scale of around 10 µm in real space and thus approximately meet the expectations, although seeming slightly too large. As a first step to minimise the influence of cloud geometry fluctuations, the g_2-profiles are recorded for different postselection steps, where the mean density map

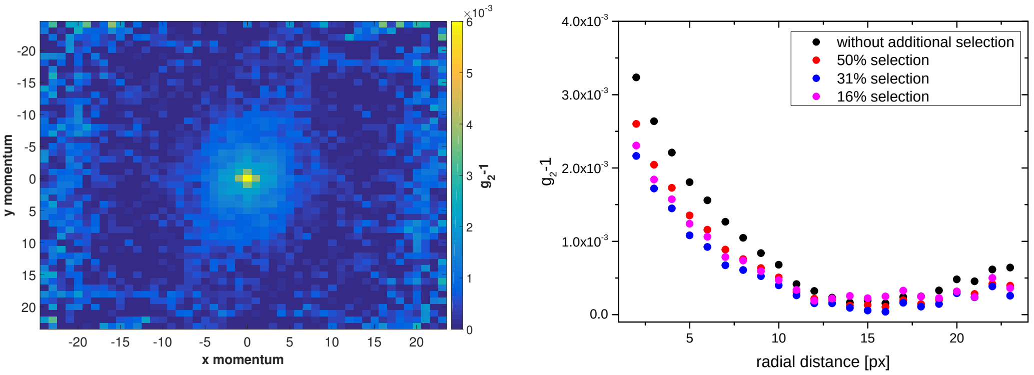

(a) Correlation map

(b) Radial correlation profile

Figure 6.1: Correlation signal obtained from a strongly interacting gas in momentum space slightly above the critical temperature for superfluidity. In (a), the g_2 correlation map is shown. The amplitude of the strong autocorrelation peak of one pixel size, indicating the zero momentum position, is around one order of magnitude larger than any other signal and was excluded here. Around the centre, at small momenta, slightly enhanced correlations are visible. In (b), the radial average of the correlation map is shown for different strict postselections. With increasingly strict selection from keeping all images (black data points), half of them (red), 31 % (blue) to only 16 % (magenta), the correlation amplitude first decreases and then saturates, suggesting that the influence of cloud geometry fluctuations decreases up to a point where it is no longer influencing the observed correlations strongly.

is compared to the individual images and only similar images are selected. Indeed, the correlation amplitude decreases with a more strict selection, but 'converges' at some point. Thus, it is assumed that cloud geometry fluctuation are no longer the dominating source for correlations at this point. For the further analysis, the selection corresponding to the blue data points and keeping 31 % of the images is applied.

In figure 6.2, the radial g_2-profiles are compared for different temperatures and different interaction strengths. The profiles do not differ significantly for the different temperatures. The correlation amplitude decreases slightly with increasing temperature, which could be explained by the slightly lower atomic densities at higher temperatures. Therefore, the imaging noise contribution gains more influence, decreasing the correlation amplitude. Consequently, the relevant quantity to be compared is the width of the g_2-profile, remaining mostly constant. There are two possible explanations for the observed independence of temperature. First of all, the correlations might be given by a (mostly) temperature independent quantity, as for example the interaction scale or even technical relics. Secondly, the temperature change might be too small, as the thermal de Broglie

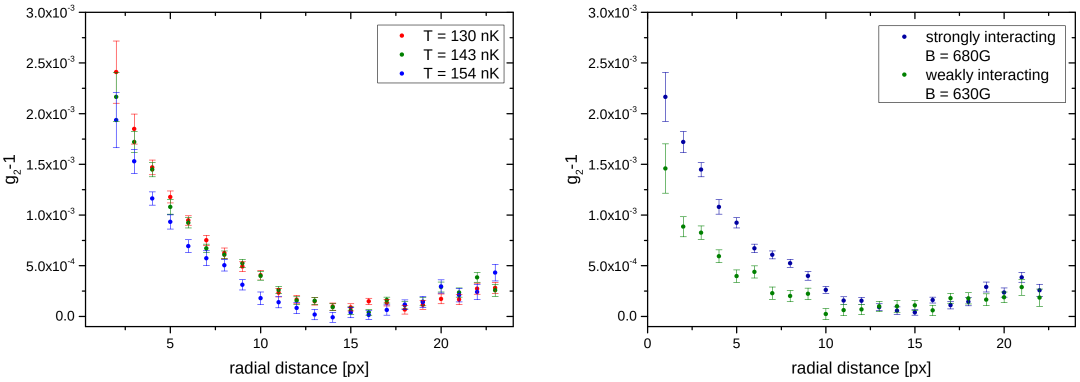

(a) Varied temperature

(b) Varied interaction strength

Figure 6.2: Influence of varying temperature and interaction strength. In(a), the radially averaged correlation map is shown for temperatures in the range of 130 nK to 154 nK, while in(b), the profiles in the weakly (630 G) and strongly (680 G) interacting limit are shown. While the width of the correlation signal does not change significantly with temperature, the cloud imaged with different initial interaction strengths shows slightly different signatures.

wavelength changes only by around 9 %.

The g_2-profiles differ more clearly when comparing the weakly and the strongly interacting case, although, as opposed to the measured profiles, a smaller correlation length for the strongly interacting case had been anticipated.

In the following, it will be argued that all observed correlations can be explained by technical artefacts only, masking any real bunching behaviour. The implications for further noise correlation analyses will be discussed afterwards.

It was concluded from the dependence of the correlation signal for an increasingly strict postselection that the fluctuations in cloud geometry are not the dominant contribution to the observed correlation signal. This can be seen in a different way as well. To this end, first the fluctuations in cloud geometry are characterised by fitting a simple Gaussian model to the individual images and recording the typical fluctuations in the parameters. The standard deviation in atom number is more directly obtained by integrating over the full density profile. With the fluctuations characterised, a test data set is constructed by randomly generating Gaussian clouds with the specified geometry fluctuations. These test data sets do not include any noise, such that any correlations can be attributed completely to the geometry variations. The data sets constructed in such a way are analysed in exactly the same way as real data sets. The results are shown in red in figure 6.3. There are different contributions to the shown profile. Fluctuations

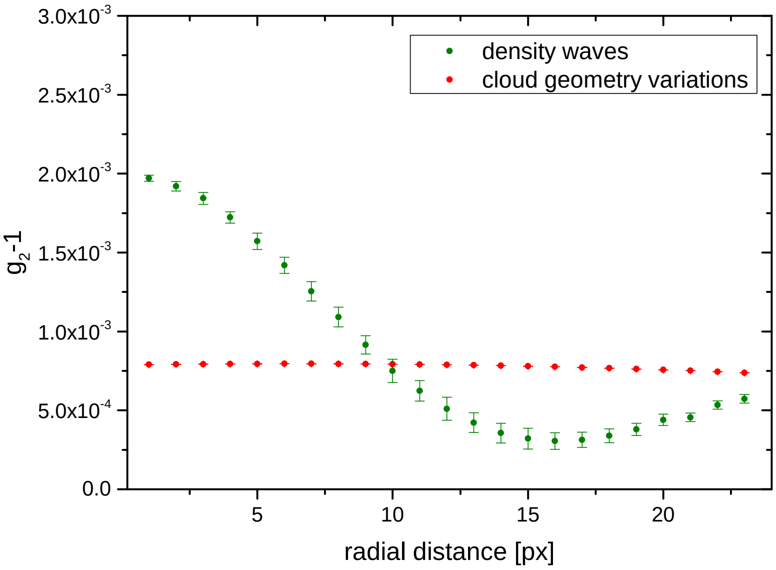

Figure 6.3: Simulated influence of fluctuations in cloud geometry and non-stable interference fringes. Typical fluctuations in cloud geometry from shot to shot are extracted from the data by fitting to a simple Gaussian model. These fluctuations (without any other influences) are simulated to show the correlations signal shown here in red. Only by including in addition interference fringes, modelled by density wave modulations, with period, amplitude and phase varying from shot to shot, a correlation signal similar to the profile observed in the experiment can be reproduced as shown here in green.

δn in atom number n lead to a mostly constant offset as long as the fluctuations are small enough, such that the approximation $(n+\delta n)^2 \approx n^2 + \delta n \cdot n$ holds. This is ensured by the postselection. Despite the images of the atom clouds being centred, fluctuation of the cloud position on a one to few pixels level are possible. When the cloud position moves from shot to shot, the negative correlations between the two slopes lead to a decreased signal around the centre. Finally, variations in the width of the cloud result in positive and position dependent correlations. Including all the fluctuations into the simulation, it can be seen that they cannot explain the observed profile, though, as they merely correspond to a mostly constant offset.

Apart from geometry fluctuations, additional substructure on the density images can result in correlation signals as well. In particular, this includes periodic interference fringes. Their influence is tested by including into the simulation a periodic modulation with a $(10 \pm 1)\,\%$ amplitude, a (30 ± 4) pixels period and a zero position varying by 9 pixels. It is important to include not only static fringes, but allow them to fluctuate from shot to shot, as otherwise no additional correlations show up. The resulting correlation signal for the new simulated test data set is shown in green in figure 6.3. It shares all important features with the correlations measured in the real data set, pointing strongly towards an explanation of the observed signal by interference fringes. To further strengthen this assumption, the real data set is considered again. The cloud envelope and the interference fringes correspond to very low spatial frequencies, while the actual noise correlation signal results from relatively high frequency fluctuations. Thus, the two contributions are reasonably well separated in Fourier space. Therefore, both a high-pass and a low-pass filter is applied to the data. The results are shown in figure 6.4. With a high-pass filter, the overall envelope of the cloud and the influence of fringes can be filtered out, while any noise correlation signal is expected to be only weakly influenced. As already anticipated, the correlation amplitude nearly decreases to zero with the low frequency contributions suppressed. Note that the scale of the correlation signal is the same as before in figure 6.2. On the other hand, by applying a low-pass

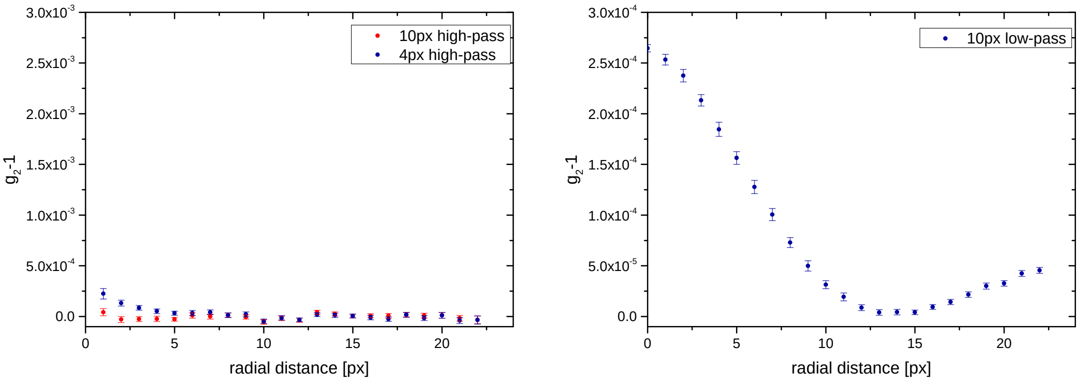

(a) High-pass filter

(b) Low-pass filter

Figure 6.4: Correlation profiles after applying Fourier space filters. On the left hand side the resulting correlations signals after applying a high-pass with cutting frequency of 10 (red) and 4 pixels (blue), respectively, are shown in the same scale as all g_2-profiles before. A high-pass filter is expected to suppress mostly correlations signals from cloud geometry fluctuations and interference fringes. On the other hand on the right side, the correlation signal after applying a (severe) low-pass filter is shown, which in turn is expected to suppress any noise correlation signal. This time the scale is one order of magnitude smaller to account for the ten times smaller effective pixel number.

and thus increasing the pixel size, the noise correlation contributions are expected to be suppressed up to the size of the new effective pixels. Nevertheless, the shape of the correlation signal is observed to be independent of the pixel size. Note however, that the amplitude for the shown low-pass filter is smaller by a factor of 10, consistent with the 10 times larger effective pixel size.

As a further test, only the frequencies corresponding to the interference fringes are filtered out. This allows us to test whether there are additional contributions apart from interference fringes. The frequencies corresponding to the fringes are however not perfectly separated from other long wavelength density variations such that the results have to be treated with care. In figure 6.5, the resulting correlation signal is shown for different interaction strengths. It can be seen that although the correlation amplitude is

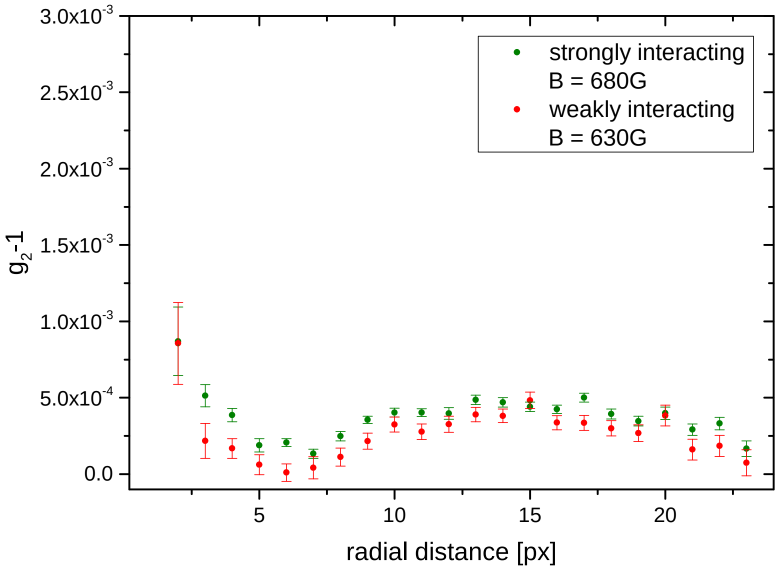

Figure 6.5: Correlation signal after applying a simple fringe removal filter in Fourier space, shown for the weakly and strongly interacting system. This illustrates that there are additional contributions to the correlations signal apart from those fringes well separated from other signals in Fourier space. Furthermore, as the profiles for different interactions match well after applying the filter, the discrepancies noticed above might be explained by additional fringes caused by the rapid ramp in the magnetic field needed for imaging the strongly interacting sample.

decreased, there is some structure left, indicating that also density fluctuations at different scales influence the observed profile. It is interesting to note that after the fringe removal filter, the profiles for the different interactions agree very well, while there was some discrepancy without removing the fringes. This might be explained by additional fringes introduced when quickly changing the magnetic field during TOF in the case of the strongly interacting sample.

All together, these observations suggest that the correlations shown here cannot be attributed to bosonic bunching. In complete analogy, a correlation analysis of a fermionic cloud reveals only (positive) technical correlations, as well. Thus, it is necessary to raise the question whether a noise correlation analysis can succeed at all in our experiment. For the data shown up to now, there are two important limiting factors: First of all, additional correlations showed up, masking all 'real' signals, and secondly, the noise correlations signals are expected to be strongly suppressed due to the small atomic noise. One workaround for the first problem is to restrict yourself to systems where there are discrete correlation lengths. Here, the expected signal would consist of sharp peaks at discrete length scales and thus still be visible above a continuous background of technical correlations. Discrete density correlation lengths are introduced most importantly by optical lattices, representing the main application area of noise correlation measurements, to be discussed in the next section. Nevertheless, interference structure will still be a limiting factor. It originates from the optical elements between the experimental chamber and the camera, and in particular from a selective polariser filtering out the MOT light from the imaging path. Here, some improvements in the experimental setup are possible. In addition, a significant suppression of imaging noise is possible by replacing the CCD camera with a model with higher quantum efficiency. A factor of two in quantum efficiency is feasible with a current generation CCD chip suppressing the imaging noise contribution by nearly a factor $\sqrt{2}$.

Improvements in the imaging technique can be made, especially for a small system, by switching to fluorescence imaging with single-atom resolution. As soon as each atom can be unambiguously identified with high fidelity, the influence of imaging noise is negligible and also technical contributions can be ruled out. As of now, such a high fidelity, spatial and single-atom resolved fluorescence imaging has been demonstrated in our group only for a single atom in a single well potential [Bec16], but nevertheless an extension to at least small many-body systems and TOFs seems feasible in the future.

As soon as the limitations of the imaging system are under control and in addition, also even smaller atom numbers can be detected reliably, there are several application methods for quantum noise correlation experiments in bulk systems. In particular, it would be interesting to study pairing by studying correlations between different spin states in momentum space. A gas of bosonic molecules in momentum space shows trivial pair correlations as for every atom of one spin state, there is at the same position an atom of the same spin state. Thus, this results in an 'autocorrelation' peak at zero momentum [RMP16]. It is important to note that the strong autocorrelation peak, as seen for example in figure 6.1, is not present when correlating two different images (two different spin

states). Nevertheless, there is still a weaker autocorrelation peak even without atoms, as each camera pixel has slightly different characteristics and introduces correlations on the one pixel scale nevertheless.
If it is now possible, on the other hand, to image a Fermi gas in momentum space at temperatures below the onset of (Cooper) pairing, radial correlations are expected to reveal the $|k, -k\rangle$ nature of the pairs by a correlation peak at 180° [Alt04, Gre05]. Imaging a Fermi gas in momentum space is however far from trivial. The usual protocol for imaging in momentum space includes a rapid ramp to $B \lesssim 600\,\mathrm{G}$, and thus projecting the system onto weakly interacting but strongly bound bosonic molecules in order to avoid momentum redistribution during TOF. While the existence of pair correlations is still observable (in the sense that every many-body pair is mapped onto a molecule) [Rie15a], its nature, that is the $|k, -k\rangle$ correlations, are of course not visible anymore. Thus, a different method for quenching interactions during TOF has to be found. The most straightforward method would be to work at very high magnetic fields ($B \gtrsim 1100\,\mathrm{G}$), where the 3D scattering length is mostly given by the background scattering length of around $a_{bg} \approx 2000\ a_0$. More elaborate schemes would involve manipulations in the internal degrees of freedom of the atoms (most prominently radio frequency pulses changing the spin state by transferring energy but only negligible momentum) in order to transfer the system into a weakly interacting ensemble directly before TOF. The matter of fermionic pairing will be discussed in detail in chapter 7.

6.3 Noise correlations in the lattice

In this chapter, the application of noise correlation measurement on systems with a discrete translation symmetry are discussed. Experimentally, such systems are realised by optical dipole traps created by the interference pattern of counter propagating laser beams as discussed before. The biggest advantage of lattice systems for the purpose of a noise correlation analysis is the signature of a discrete 'Bragg' peak in the momentum space correlations as a consequence of the discrete translation symmetry. Noise correlations signatures have already been successfully demonstrated in three-dimensional lattice systems for characterising a Mott insulator state [Föl05]. However, the analysis protocol cannot be directly transferred to a 2D lattice for the reasons given below. As it was experimentally not possible to prepare a 2D molecular Mott insulator during the course of this thesis, this chapter focusses mostly on the development of a noise correlation method rather than a detailed study of lattice physics. Therefore, first some theoretical considerations are made to verify the applicability of noise correlations for short TOF experiments, and afterwards correlations in a thermal gas in the lattice are studied. Nevertheless, at the end of this section, a brief overview over possible next steps towards a strongly correlated Fermi gas in the lattice are briefly discussed with a special focus on the application of noise correlation experiments to probe these systems.

6.3.1 Correlation signal for short TOF experiments

Typical derivations of theoretical expected noise correlation signals assume the following two situations [Föl14, Alt04]:

- A reasonably long time of flight such that real space can be directly mapped onto momentum space.
- An expansion in a flat potential during TOF.

Both assumptions are not met in the experiments described here. When working in full momentum space, the correlation peaks would show up at a radial distance of nearly 1 mm, while the atomic cloud is spread over a few 100 µm only. Therefore, to have significant atom noise, all noise correlation experiments are limited to short TOFs. Furthermore, by virtue of the intended matter wave focussing, the atom cloud expands during TOF in a harmonic potential. For these reasons, it is not directly clear what to expect from these noise correlation measurements described here.
In the following, an adapted expression of equation 3.12 for the g_2-function in a deep lattice will be derived, and it will be shown that for an assumed zero-temperature Mott insulator state, distinct peaks will show up nevertheless. Furthermore, simulated correlation signals (neglecting additional noise sources) are shown for realistic experimental parameters.

Derivation of the noise correlation function

The following derivations are for the ease of notation exclusively in one spatial dimension. However, at least for square lattices, including a second dimension is straightforward. Furthermore, harmonic oscillator units (with respect to the trap frequency ω during TOF) are assumed in this paragraph.

Step 1: Time evolution of the single-particle wave function For a deep lattice, the on-site wave function is well approximated by a Gaussian[1]

$$\phi(x) = \frac{1}{(2\pi\sigma^2)^{\frac{1}{4}}} e^{-\frac{x^2}{4\sigma}} \tag{6.4}$$

in terms of its width σ set by the on-site frequency $\omega_{on-site}$ of the lattice trap.
The time evolution of a Gaussian, shifted at time $t = 0$ by x_0 with respect to the origin (defined to be at the minimum position of the overall trap), may be shown to be

---

[1] In general it is given by a Wannier function.

(compare e.g. [Tha00])

$$\begin{aligned}\phi(x-x_0,t) =& \frac{1}{(2\pi\sigma^2)^{\frac{1}{4}}}\left(\cos(\omega t)+i\frac{1}{2\sigma^2}\sin(\omega t)\right)^{\frac{1}{2}} e^{i\frac{x_0^2}{4}\sin(2\omega t)}\cdot \\ &\cdot e^{-ix_0 x\sin(\omega t)}e^{-a(t)\frac{(x-x_0\cos(\omega t))^2}{2}}, \end{aligned} \tag{6.5}$$

where

$$a(t) = \frac{1}{2\sigma^2}\left[\frac{\sin^2(\omega t)+\cos^2(\omega t)}{\frac{1}{4\sigma^4}\sin^2(\omega t)+\cos^2(\omega t)} - i\frac{(\frac{1}{2\sigma^2})\sin^2(\omega t)\cos^2(\omega t)}{\frac{1}{4\sigma^4}\sin^2(\omega t)+\cos^2(\omega t)}\right] \tag{6.6}$$

$$:= \frac{1}{2\sigma^2}\left[A - i\cdot B\right]. \tag{6.7}$$

Step 2: The density-density operator As a next step, the density operator is computed. It takes in principle the same form as before in chapter 3:

$$\hat{n}(x,t) = \hat{a}^\dagger(x,t)\hat{a}(x,t) = \sum_{jk}\hat{a}_j^\dagger(x,t)\hat{a}_k(x,t), \tag{6.8}$$

$$\text{where}\quad \hat{a}_j^\dagger(x,t) = \phi(x-x_j,t)\hat{a}_j. \tag{6.9}$$

By inserting the single-particle wave function, the density operator turns out to be given by

$$\hat{n}(x,t) = \mathcal{N}\sum_{jk} e^{-\frac{A}{4\sigma^2}\left[(x-\tilde{x}_j)^2+(x-\tilde{x}_k)^2\right]}e^{-i\left[\alpha(x_k^2-x_j^2)+\beta x(x_j-x_k)\right]}\hat{a}_j^\dagger\hat{a}_k, \tag{6.10}$$

$$\text{where}\quad \mathcal{N} = \left(\frac{1}{2\pi\sigma^2}\right)^{\frac{1}{2}}\sqrt{\cos^2(\omega t)+\frac{1}{4\sigma^4}\sin^2(\omega t)}, \tag{6.11}$$

$$\alpha = \frac{\sin(2\omega t)}{4} + \frac{B}{4\sigma^2}\cos^2(\omega t), \tag{6.12}$$

$$\beta = \sin(\omega t) + \frac{B}{2\sigma^2}\cos(\omega t), \tag{6.13}$$

$$\tilde{x}_i = x_i\cos(\omega t), \tag{6.14}$$

and accordingly the density-density operator[2] is computed to be

$$\begin{aligned}\hat{n}(x_1,t)\hat{n}(x_2,t) =& \mathcal{N}^2\sum_{jk,lm} e^{-\frac{A}{4\sigma^2}\left[(x_1-\tilde{x}_j)^2+(x_1-\tilde{x}_k)^2+(x_2-\tilde{x}_k)^2+(x_2-\tilde{x}_m)^2\right]}\cdot \\ &\cdot e^{-i\left[\alpha(x_k^2-x_j^2+x_m^2-x_l^2)+\beta(x_1(x_j-x_k)+x_2(x_l-x_m))\right]}\hat{a}_j^\dagger\hat{a}_k\hat{a}_l^\dagger\hat{a}_m. \end{aligned} \tag{6.15}$$

---

[2] Again, only one spin state is considered for now.

Step 3: Expectation value for a deep lattice Normal ordering of the creation and annihilation operators works as before in equation 3.8. The autocorrelation term will again be neglected for now, since it only contributes to a strong peak at zero momentum, and for concreteness bosonic commutation relations are assumed in the following. Focussing again on a deep lattice, such that the lattice occupations may be described in terms of Fock states and $\langle \hat{a}_j^\dagger \hat{a}_k \rangle = \delta_{jk} n_j$, the expectation value of the normal ordered operator - neglecting a small offset term - is given by

$$\langle \hat{a}_j^\dagger \hat{a}_l^\dagger \hat{a}_k \hat{a}_m \rangle \approx \delta_{jm}\delta_{lk} n_j n_l + \delta_{jk}\delta_{lm} n_j n_l \tag{6.16}$$

as we had already seen in equation 3.9. The second term of the above equation will be cancelled by normalisation, as will be shown below.
With this, the expectation value of the second order correlator is given by

$$\begin{aligned} \langle \hat{n}(x_1,t)\hat{n}(x_2,t) \rangle =& \mathcal{N}^2 \sum_{jl} \Bigg[e^{-\frac{A}{4\sigma^2}\left[(x_1-\tilde{x}_j)^2+(x_1-\tilde{x}_l)^2+(x_2-\tilde{x}_l)^2+(x_2-\tilde{x}_j)^2\right]} \cdot \\ & \cdot e^{-i\beta(x_1-x_2)(x_j-x_l)} + e^{-\frac{A}{2\sigma^2}\left[(x_1-\tilde{x}_j)^2+(x_2-\tilde{x}_l)^2\right]} \Bigg] n_j n_l . \end{aligned} \tag{6.17}$$

Step 4: Noise correlation function To arrive at the noise correlation function as defined in equation 3.11, relative coordinates $d = x_2 - x_1$ and $x = \frac{x_1+x_2}{2}$ are introduced and the centre of mass coordinate is integrated out by means of Gaussian integration. With this, the g_2-function is finally given by

$$g_2 - 1 = \frac{\sum_{jl} e^{-\frac{A\cos^2(\omega t)}{4\sigma^2}(x_j-x_l)^2} e^{i\beta d(x_j-x_l)} n_j n_l}{\sum_{mn} e^{-\frac{A}{4\sigma^2}\cos^2(\omega t)(x_m-x_n)^2} e^{-\frac{A}{2\sigma^2}\cos(\omega t) d (x_m-x_n)} n_m n_n} . \tag{6.18}$$

As a consistency check, consider the correlation signal of an idealised Mott insulator at a TOF of a quarter of the trap period. Thus, a one-to-one mapping of position and momentum space is possible. Indeed, after a quarter period, $\cos(\omega t) = 0$ and $\beta = 1$, such that

$$g_2 - 1 = \frac{1}{N^2}\sum_{jl} e^{id(x_j-x_l)} n_j n_l = \frac{1}{N^2}\left|\sum_j e^{idx_j} n_j\right|^2 = \frac{1}{N^2}\left|\sum_j e^{idaj}\right| \tag{6.19}$$

with the lattice spacing a. Therefore, peaks at the lattice momentum show up as expected. Note that β, setting the overall periodicity of the complex 'Fourier type' sum in equation 6.18, is already for short times well approximated by $\beta(t) \approx \sin(\omega t)$ such that lattice peaks at a general TOF show up at the corresponding lattice momenta after TOF, as expected.

Step 5: Numerical simulations To illustrate that noise correlations for short times of flight are in principle possible, in the following some results of numerical calculations of g_2 according to equation 6.18 for realistic experimental parameters are presented. All simulations assume a perfect Mott insulator at zero temperature and no additional noise sources. They are done in one dimension only, but as mentioned before, this is without loss of generality for a square lattice. The simulations in figure 6.6 look similar to exact momentum space calculation on a qualitative level, except for a rescaling of the lattice momentum and an overall envelope. The envelope can be explained by the additional length scale introduced by the short TOF in the sense that the wave functions of different atoms do not overlap fully for these times and not all atoms can be correlated, correspondingly. The simulations suggest that in order to observe correlation peaks of different orders with sufficient amplitude, a TOF of at least 5 ms is needed. On the other hand, already at 1 ms, in principle first order peaks may be observed, however with the drawback of only around 5 % of the full amplitude.

6.3.2 Experimental noise correlation analysis

In the simulations shown above, unity filling of the lattice with no additional excitations in form of unoccupied or doubly occupied lattice sites where assumed. Including defects results in additional uncorrelated contributions to the correlation function. Thus, the qualitative signature remains exactly the same and only the amplitude of the correlation signal decreases. This motivates considering also a thermal gas of bosonic molecules in the lattice, where remnants of the correlation Bragg peaks are expected to survive.

The possibility of correlations in a thermal gas in the lattice are experimentally tested as follows: A cold, yet non-superfluid gas in the weakly interacting limit at 625 G ($|1\rangle - |3\rangle$ mixture) is prepared in a roughly $20 \cdot E_R$ deep lattice and imaged after 800 µs time of flight. After this TOF, the correlation peaks are expected to show up at 50 µm. A longer TOF would be desirable in terms of correlation amplitude, but is not possible with the current cloud parameters, as otherwise the atomic density at the expected correlation length is too low. A set of 500 images is taken.

The general procedure of image postselection and manipulations as well as the calculation of the correlation map itself is similar to the procedure discussed in detail for the bulk gas system. There is, however, one difference: Since the correlation length is on the same length scale as the cloud envelope, the use of high-pass filtering is limited. In order to at least partially suppress the influence of cloud fluctuations, each image is fitted to a two-dimensional Gaussian model, and the resulting cloud shape subtracted from the data. The results for the correlation map with and without additional image manipulation are shown in figure 6.7. Neither with nor without Fourier space filtering and fit subtraction is any noise correlation peak visible. Even if, despite the low density and the short TOF, a correlation peak is present, it is masked by additional technical correlation signals. Apart from correlations resulting from interference fringes, as stud-

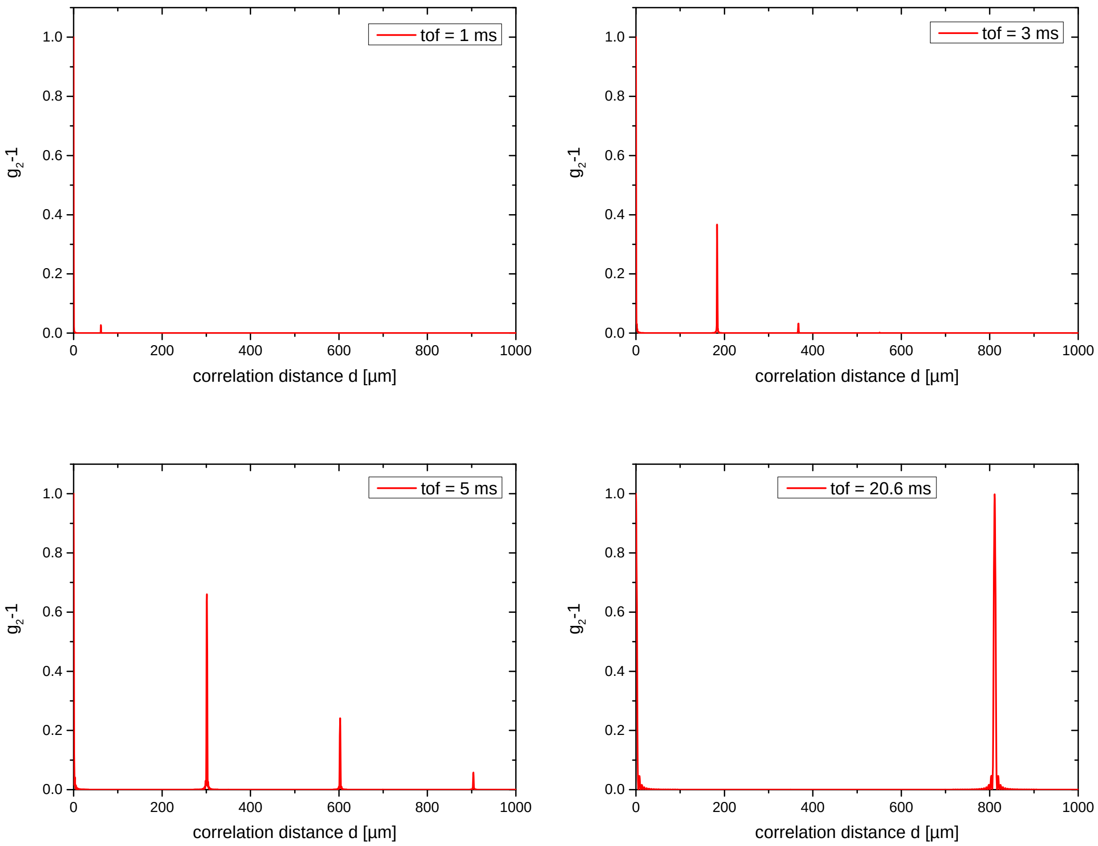

Figure 6.6: Simulation of the correlation amplitudes for different TOFs and a 1D lattice with 150 lattice sites and unity occupation. 150 lattice sites correspond to a 'cloud' size of 80 µm, comparable to a realistic experimental situation. Apart from the restriction to one dimension, all trap parameters are taken from experiment. The simulations show that, as expected, the correlation peaks show up at the respective positions mapping to the lattice momentum after TOF. In particular, the peaks are at smaller distances d for shorter times. In addition, for TOF different from the $T/4$-time, an additional time dependent envelope reduces the height of all peaks with increasing correlation distance. This envelope takes into account that without a true mapping onto momentum space, the wave functions of the different particles do not fully overlap and thus can only partially be correlated.

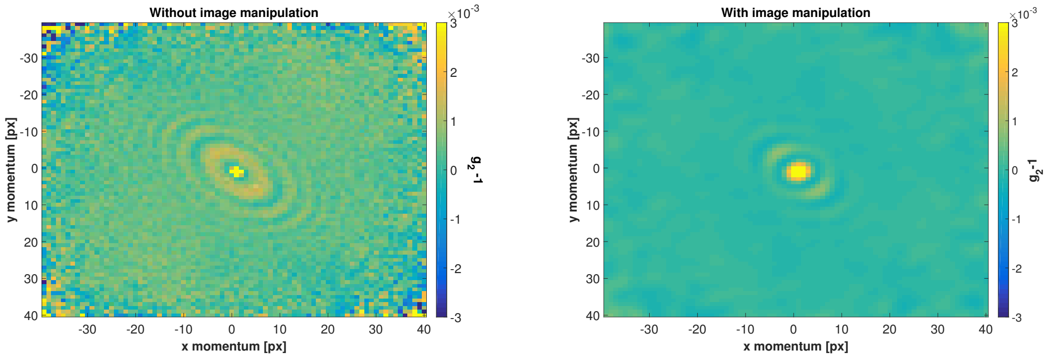

Figure 6.7: Noise correlation maps of a weakly interacting thermal gas in the lattice. On the left hand side, the g_2-signal after postselection but, apart from the centering process, without any image manipulation is shown. On the right hand side, the correlation signal for the same data, this time with a three pixel effective bin size, a 3 pixel high-pass filter applied and the cloud envelope subtracted, is shown. In both cases, additional structure masks any possible signal.

ied before, most importantly, a ring structure around the autocorrelation peak is visible. This structure is not directly related to the lattice system, however. In can be observed also when studying a bulk gas after a short TOF and even in-situ. In particular, the periodicity of the rings is independent of the TOF, although the structure smoothens out significantly after around 2 ms. The ring correlations could be explained by additional substructures on the SWT.

6.3.3 Remarks and outlook

One of the most important reasons for considering the technique of noise correlation experiments is that they allow to observe complex order in a lattice system. As stated already above, the signature of a Mott insulator is also observed when studying a thermal gas, as the origin of the correlation peaks are not the reduced number fluctuations of the Mott insulator, but rather the permutation symmetry of the total wave function [Alt04]. However, if there is additional complex order, as given for example by antiferromagnetic correlations, it would show up by the Fourier transform of the spin structure factor [Alt04]. In the concrete case of antiferromagnetic ordering, this would result in lattice peaks at half the lattice momentum. As the same signature is expected from density waves with a periodicity of twice the lattice constant, it is important to record correlations between different spin states as well. In general, the full information is recorded when correlations between the same spin states, between the two different spin states, and between the perpendicular components of the spins by applying a global $\pi/2$ pulse prior to TOF expansion are obtained [Bru09]. With all three correlation functions at hand, in the 3D phase transition from a fermionic Mott insulator to an antiferromagnetically ordered (AFM) state, even the axis of symmetry breaking might be identified [Bru09]. In two dimensions, a phase transition into an AFM state does not exist. Nevertheless, some antiferromagnetic correlations form at low temperatures (or, more precisely, entropies).

In addition, possible d-wave pairing is expected to be closely related to the question of high-temperature superfluidity in cuprates [Hof02] and may be studied by strongly correlated Fermi gases in a lattice and noise correlation measurements.

The general idea to reach strongly correlated, low entropy Fermi gases is the following: First a molecular Mott insulator is prepared. Here, the motional entropy can be reduced efficiently and the spin entropy is 'trivially' minimised, as all of the spins are paired up into molecules. By simply tuning the magnetic field to the BCS site of the Feshbach resonance, the bosonic Mott insulator is transferred into a fermionic band insulator. However, if the lattice trap is adiabatically transferred into a superlattice with twice the lattice frequency, it seems feasible to tune the system into a fermionic Mott insulator while keeping the low spin entropy, and thus strong antiferromagnetic correlations. For this to work, a more elaborate, since tunable, lattice system has to be implemented. Therefore, it is planned to produce and shape nearly arbitrary optical potentials with the help of a spatial light modulator [Hol14].

7 Fermionic pairing above the critical temperature

In the previous chapters, noise correlations as a toolbox for observing many-body density correlations were explained in detail. One important application is the detection of (many-body) pairing. S-wave Cooper-like pairs, allowing for fermionic superfluidity in our system, could be directly observable by 180° correlations in the radial g_2-function, and even more complex pairing mechanisms would show up by respective signatures. Another major application, where a detection of pairing is of interest, has not been discussed so far: Pairing in the normal phase of a Fermi gas. A so-called pseudogap regime might exist between a crossover temperature T^* and the critical temperature T_C for superfluidity, as motivated in subsection 2.2.3. One measurement scheme would be to observe momentum space pair correlations at different temperatures. In addition to the existence of pair correlations, this method would directly allow to distinguish 'bosonic' dimer pairing and 'fermionic' many-body pairing. However, apart from the technical problems described in the previous chapters, the method has the disadvantage that no information on the pairing energy is obtained, and in addition, very small paired fractions are inherently hard to resolve. Furthermore, pairing can only be probed trap averaged. For these reasons, in this chapter, a different method to probe pair correlations is facilitated, namely RF spectroscopy. Here, the single-particle excitation spectrum is probed spatially resolved, while the existence of true many-body pairing has to be argued more indirectly, such that in an ideal case, RF spectroscopy is combined with noise correlation experiments nevertheless.

This chapter gives an overview over the ongoing measurements aimed at measuring fermionic pairing above the critical temperature. After a short introduction on the basics of RF spectroscopy in section 7.1, some remarks on a mean field description of the pseudogap region are made in section 7.2. Then, in section 7.3, our system and the experimental methods are introduced, while in section 7.4 the (preliminary) experimental results are presented.

7.1 RF spectroscopy

The experimental relevant energy eigenstates $|1\rangle, |2\rangle$ and $|3\rangle$ of ^{6}Li are separated from each other (in the magnetic field range considered here) by roughly $E = h \cdot 80\,\mathrm{MHz}$. Thus, the transition frequencies between the hyperfine states lie well within the radio

frequency range and may be probed by RF spectroscopy. To this end, a RF pulse with an oscillating magnetic field is applied and its frequency scanned. As soon as the frequency is resonant with the energy difference between two hyperfine states, atoms are transferred from one state to another by magnetic dipole transitions, flipping the spin. Thus, the energy difference between the states can be inferred from recording the atom number in one of the states as a function of the applied RF frequency.
The basics of probing pairing with RF spectroscopy are explained in this section.

7.1.1 Coherent RF transitions: Rabi oscillations

For a relatively long RF pulse, the instantaneous oscillating magnetic field may be approximated by a plane wave

$$\vec{B}_{rf}(t) = \vec{B}_0 \cos(\omega_{rf} t). \tag{7.1}$$

Assuming for now a two-spin system without any decoherence and dephasing mechanism, applying the magnetic field rotates the spin with the Rabi frequency

$$\Omega_{ff} \propto \mu_s \vec{B}_0 \vec{e}_s. \tag{7.2}$$

These are the well-known Rabi oscillations. The subscript ff denotes the free-free frequency, indicating that there are no additional interactions present either in the initial or the final state. The Rabi frequency is dependent on the orientation of the magnetic field with respect to the spin axis $\vec{e}_s$ and the magnetic moment μ_s. In the Pashen-Back regime for high magnetic fields, the nuclear and electronic spins decouple completely and μ_s is given by the nuclear magnetic moment, as the RF field drives magnetic dipole transitions between the nuclear spin states. At the fields considered in this thesis, the two spins decouple up to a small admixture of around 1 %. The nuclear magnetic moment is around 2000 times smaller than the Bohr magneton, however, such that the small admixture increases the Rabi frequency considerably. An example of measured Rabi oscillations is displayed in figure 7.1.

Considering in addition the non-resonant Rabi frequency $\Omega' = \sqrt{\Omega^2 + (\Delta\omega_{rf})^2}$, also the lineshape Γ, which takes the form of a Lorentzian of width Ω_{rf}, may be obtained [Her15]. Thus, starting from a non-interacting sample of one hyperfine state by applying an RF pulse of a suitable length and scanning the RF frequency, a spectrum may be recorded by measuring either the depletion of the initial state or the transferred atom number. At the resonance, the RF energy matches exactly the difference in energy E_{ff} between the hyperfine states.

Up to now, a system described completely in terms of its spin degree of freedom was considered. For RF transitions, the spatial degree of freedom can easily be included. In general, the resonant Rabi frequency is proportional to the matrix element between

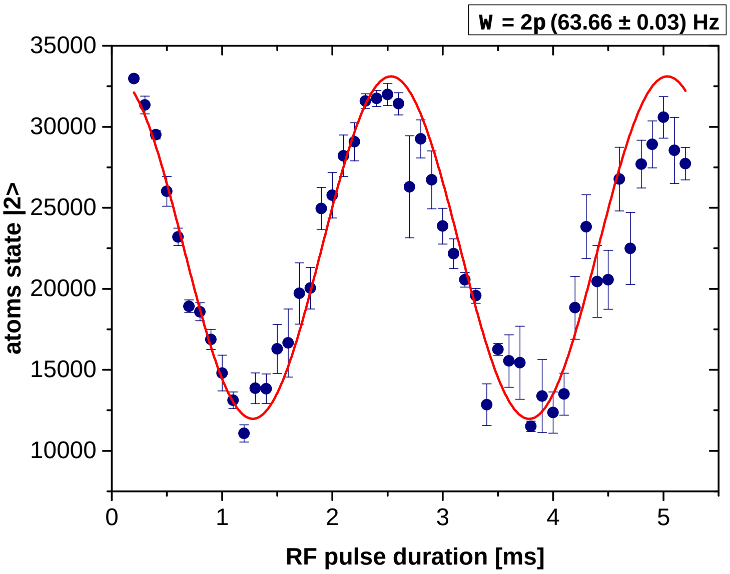

Figure 7.1: Measurement of the Rabi frequency Ω_{ff} for the transition between state $|1\rangle$ and $|2\rangle$. A spin-polarised gas of atoms in state $|2\rangle$ is prepared and a RF pulse of variable pulse duration resonant with the $|1\rangle - |2\rangle$ transition applied. By recording either the remaining atoms in state $|2\rangle$ or the transferred atoms into state $|1\rangle$ as a function of the RF pulse durations, the oscillations are observed. Here, the Rabi frequency is measured to be $\Omega_{ff} = 2\pi(63.66 \pm 0.03)\,\mathrm{Hz}$. In general, the Rabi freqencies have to be measured experimentally because, despite the total RF power being known (here around 1 W), the exact power at the cloud position is a priori unknown.

initial state $|\Phi_i\rangle$ and final state $|\Phi_f\rangle$, given in terms of the operator $\hat{RF}$ describing the RF transitions,

$$\Omega \propto \langle \Phi_f | \, \hat{RF} \, | \Phi_i \rangle \, . \tag{7.3}$$

The single-particle wave function separates into a spatial wave function, describing the external degree of freedom, and a pure spin function as considered up to now,

$$\Psi_{i/f} = |\Psi_{spatial,i/f}\rangle \, |\Phi_{spin,i/f}\rangle \, . \tag{7.4}$$

Since the momentum transfer of the RF photon on the atoms is negligible, the spatial part of the wave functions is mostly unaffected by the operator $\hat{RF}$ and consequently

$$\Omega \propto \Omega_{ff} \, \langle \Psi_{spatial,f} | \Psi_{spatial,i} \rangle \, , \tag{7.5}$$

i.e. the Rabi frequency is modified by the wave function overlap. In addition, the external degrees of freedom can lead to an energy shift ΔE of the initial (or final) state. Consequently, also the resonance frequency of RF transition energy shifts to

$$E_{rf} = E_{ff} + \Delta E. \tag{7.6}$$

Consider for example the case where the initial state is bound with a binding energy E_B, while the final state remains unaltered. Comparing the resonance frequency ω_{rf} of this system with the one obtained from a sample without the bound (ω_{ff}) state, the binding energy may be directly obtained from equation 7.6 by

$$E_B = \pm\hbar \cdot (\omega_{rf} - \omega_{ff}). \tag{7.7}$$

Here, the + sign applies to the case where the final state has a higher energy than the initial state, while the − sign holds otherwise.
Thus, RF spectroscopy provides a tool to probe the energy levels of a system by recording the single-particle excitation spectrum.

7.1.2 Probing an interacting system with RF spectroscopy

The above equation 7.6 offers a possibility to measure pairing energies. However, it is not possible to coherently drive Rabi oscillations between initial and final state in a strongly interacting system, as interactions lead to a quick decoherence. Nevertheless, a transition rate may be obtained by considering linear response and Fermi's golden rule, where a negligible population of the final state is assumed. For the case of the initial state being a mixture of state $|1\rangle$ and $|3\rangle$, driving the $|2\rangle - |3\rangle$ transition[1] and neglecting the effect of final state interactions, this leads to a transition rate

$$\Gamma(\omega) = \pi\Omega^2 \sum_k A_{|3\rangle}(\vec{k}, \eta_k - \omega) f(\eta_k - \omega) \tag{7.8}$$

in terms of the Fermi function f, and the spectral function $A_{|3\rangle}(\vec{k}, E)$ of the interacting state $|3\rangle$. The spectral function has to be calculated in general by a suitable many-body theory. The Fermi function ensures that only the occupied part of the spectral function is taken into account. In the special cases of either two-body pairing (dimers) or zero-temperature BCS many-body pairing in two dimensions, the transition rate takes the form [Som12]

$$\Gamma(\omega) \propto \frac{1}{\omega^2}\Theta(\omega - \omega_{th}), \tag{7.9}$$

with $\omega_{th} = E_{th}/\hbar$ and the threshold energy given by $E_{th} = E_B$ in the two-body pairing limit, and, as will be shown in section 7.2, also in BCS theory. The lineshape of the

---

[1] Other mixtures and transitions are described analogously.

transition is highly asymmetric, as expected for a bound-to-free transition.
With the above considerations, the onset of pairing can be observed by a shift of the threshold frequency. Up to now, the effects of final state interaction were not considered, however.

7.1.3 Final state interactions

There are different types of final state interactions possible. As the following considerations are not restricted to a fixed spin configuration, the states will be labelled $|a\rangle, |b\rangle, |c\rangle$ for now. We start from a strongly interacting system of two spin states ($|a\rangle - |b\rangle$) and drive the transition to a third one ($|b\rangle \rightarrow |c\rangle$). State $|c\rangle$ is in general interacting with the other two states. The interactions between $|b\rangle$ and $|c\rangle$ do not shift the transition frequency if the transition can be considered coherent[2] [Zha12]. However, a three-component gas in the final state leads to three-body losses. Therefore, the cloud is always imaged directly after applying the RF pulse such that the losses are negligible. The most crucial impact have interactions between state $|a\rangle$ and $|c\rangle$, though.
A suitable model to describe final state interactions is given by a Fermi polaron model [Zha12, Sch12, Nga12]. A polaron quasi-particle is given by a single impurity of state $|c\rangle$ emerged in a 'sea' of $|a\rangle$ particles. As a finite, yet small number of particles is transferred into state $|c\rangle$, and in addition the $|b\rangle - |c\rangle$ interactions do not directly influence the transition frequency, an approximate validity of the model is expected. Nevertheless, small deviations might still result from the effects of the $|a\rangle - |b\rangle$ interactions. The zero-momentum spectral function of the Fermi polaron in two dimensions is split into two branches. These is a broad (and thus short-lived) repulsive polaron with a positive energy for negative (and small positive) $\ln(k_F a_{2D})$, as well as a narrower attractive polaron for positive (and small negative) $\ln(k_F a_{2D})$ [Sch12]. Here, the appropriate interaction parameter is calculated by considering the Fermi wave vector corresponding to state $|a\rangle$ and the 2D scattering length describing the $|a\rangle - |c\rangle$ interactions. The polaron energies may be obtained by a T-matrix approach [Sch12]; here we are however interested in systems with relative weak final state interactions. Thus, the energy shifts are correspondingly small and it is sufficient to consider perturbative results obtained for small $|1/\ln(k_F a_{2D})|$.
The repulsive polaron energy E_+ in the limit $E_B/E_F \rightarrow \infty$ is given by [Nga12]

$$E_+ = \frac{2 \cdot E_F}{\ln(E_B/E_F)}. \tag{7.10}$$

---

[2] It was stated before that it is not possible to drive coherent Rabi oscillations. Nevertheless the single excitation into state $|c\rangle$ is still to a good approximation coherent.

On the other hand, the attractive (zero-momentum) polaron energy E_- is given by the integral equation [Zha12]

$$E_- = E_F \cdot \int_0^1 \frac{-2du}{-\ln(E_B/E_F) + \ln\left[\sqrt{\left(1 - \frac{E_-}{2E_F}\right)^2 - u} + \left(1 - \frac{E_-}{2E_F} - \frac{u}{2}\right)\right]}. \tag{7.11}$$

The energy shifts due to a final state polaron quasi-particle are shown in figure 7.2.

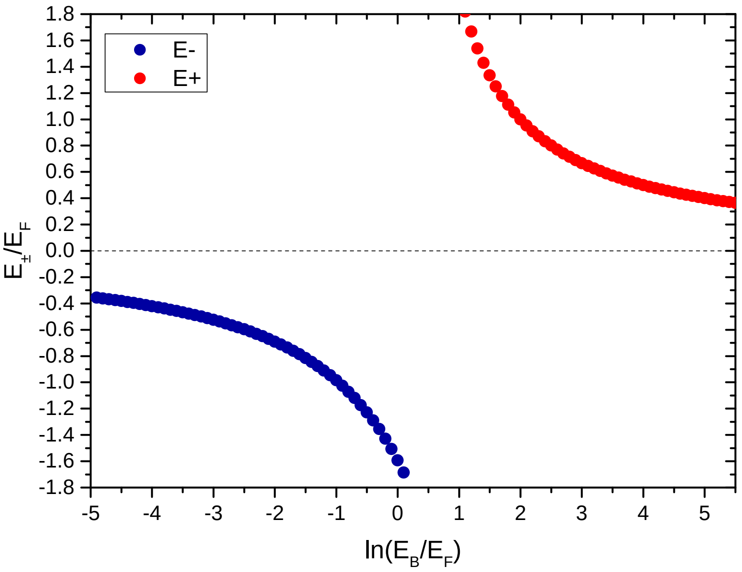

Figure 7.2: Energy shifts E_+ (red) and E_- (blue) of the repulsive and attractive polaron, respectively. The energy shift in units of the local Fermi energy is shown as a function of the logarithm of the (final state) two-body binding energy in units of the local Fermi energy. In the limit of weak final state interactions, $\ln(E_B/E_F)$ becomes large and the polaron shift is small. Note that the quasi-particle spectral weights of either the attractive or repulsive polaron are large ($\gtrsim 90\,\%$) for the final state interactions considered in this thesis [Sch12].

Apart from the above considerations, final state interactions also influence the observed lineshapes. For example, due to a small positive (3D) final state scattering length, there exists a deeply bound (up to several 100 kHz) dimer final state. The additional bound-bound transition is completely separated in frequency from the bound-free transition.

Nevertheless, due to the dimer state, the lineshape of the recorded transition is altered. The effect was calculated for the case of an initial dimer state in [Lan12] and results in logarithmic corrections of the form:

$$\Gamma_C(\omega) \propto \frac{\Omega^2}{\omega^2 \left[\ln^2(\omega/E_B') + \pi^2\right]} \tag{7.12}$$

in terms of the final state dimer energy E_B'. The above lineshape is valid for frequencies larger than any other energy scales. In particular, the logarithmic corrections have the effect that the threshold energy does not coincide with the maximum of the lineshape anymore, which is shifted slightly away. While the above formula is, strictly speaking, not valid when approaching the BCS limit, it can be used at least in the crossover region to extract the threshold energy.

In addition to the final state interactions, it is important to keep in mind that the free-free peak, which serves as a reference to compare the bound-free peak to, is also affected by interactions. In an interacting system of $|a\rangle - |b\rangle$, the $|b\rangle \to |c\rangle$ free-free transition acquires a so-called clock shift. In a general interacting system, the clock shifts are given by the first momentum of the transfer rate $\Gamma(\omega)$

$$\langle\omega\rangle = \frac{\int_{-\infty}^{\infty} d\omega \Gamma(\omega) \cdot \omega}{\int_{-\infty}^{\infty} d\omega \Gamma(\omega)}. \tag{7.13}$$

The clock shift can be evaluated assuming mean field interaction, where this so called Hartree shift gives a measure for the shift in energy of one of the particles due to the mean field of all others. For fermions with attractive mean field interactions, the Hartree term is evaluated to be

$$\langle\omega\rangle = g \cdot n_{|a\rangle} \tag{7.14}$$

in terms of the density $n_{|a\rangle}$ of state $|a\rangle$ and the interaction parameter

$$g = \frac{\hbar}{2m} \frac{\ln(k_F a_{2D})}{\ln(k_F a_{2D}) + \pi^2}. \tag{7.15}$$

As a consequence, the measured free-free frequency in an interacting system is shifted with respect to the frequency obtained in a non-interacting system.

7.2 Remarks on a mean field treatment

Utilising RF spectroscopy, it becomes possible to probe the pseudogap region experimentally. From a theoretical point of view, there is no complete theory describing pairing in the normal phase. Nevertheless, in order to get some intuition and to have a reference

to compare to, it is instructive to consider mean field predictions for pairing.
A pseudogap region is not directly included in BCS mean field theory as it only describes pairing in the superfluid phase. Nevertheless, a first approximation for the threshold RF energy E_{th} needed (in addition to the bare transition energy $E_{ff} = \hbar\omega_{ff}$) to drive the bound-free transition can be obtained from zero-temperature mean field theory, resulting in

$$E_{th} = \min_k \left(\sqrt{\eta_k^2 + \Delta^2} + \eta_k - \mu \right), \tag{7.16}$$

with $\eta_k = \frac{k^2}{2m} - \mu$ and $\Delta^2 = 2E_B E_F$. The origin of this formula is illustrated in figure 7.3 The minimum in equation 7.16 is obtained (independent of μ) by setting $k = 0$,

$$E_{th} = \sqrt{\mu^2 + \Delta^2} - \mu = E_B, \tag{7.17}$$

which is in particular independent of density and thus constant in the trap. It is important to note that in BCS theory, the minimum of the energy gap is at $k = k_F$ for $\mu > 0$. This is however not the case for the threshold energy (compare to this end again to figure 7.3). The important difference is that the energy gap refers to placing an elementary excitation within the system, while in RF spectroscopy, a particle is removed and then projected onto a free state.
Extending the BCS mean field theory to finite temperatures results in a temperature dependent gap to be obtained by numerically solving the mean field equations [Bab98]

$$-\frac{1}{g} = \frac{1}{V} \sum_{\vec{k}} \frac{1}{2E_{\vec{k}}} \tanh \frac{E_{\vec{k}}}{2T} \tag{7.18}$$

and

$$n = \frac{1}{V} \sum_{\vec{k}} \left(1 - \frac{\eta_{\vec{k}}}{E_{\vec{k}}} \tanh \frac{E_{\vec{k}}}{2T} \right). \tag{7.19}$$

Assuming mean field theory to be (partially) valid even in the strongly interacting regime, a first estimate of the crossover temperature T^* can be obtained. To this end, it is assumed that the BCS crossover temperature, lying significantly above the observed critical temperature for superfluidity in the crossover region, rather gives the onset of pairing [Lev15, Bab98], while quantum fluctuations lower the temperature for phase coherence (as motivated in subsection 2.2.3). Compare to this end again figure 2.6a, where an estimate for T^* is included in the theory phase diagram by means of the Thouless criterion. With these assumptions and the above equations 7.18 and 7.19, the temperature dependence of the gap can be estimated as plotted in figure 7.4 This results in particular in $\Delta(T) \equiv 0$ for $T \geq T^*$ and the ratio $\Delta(T)/\Delta(0)$ smoothly increasing to 1 for $T < T^*$.

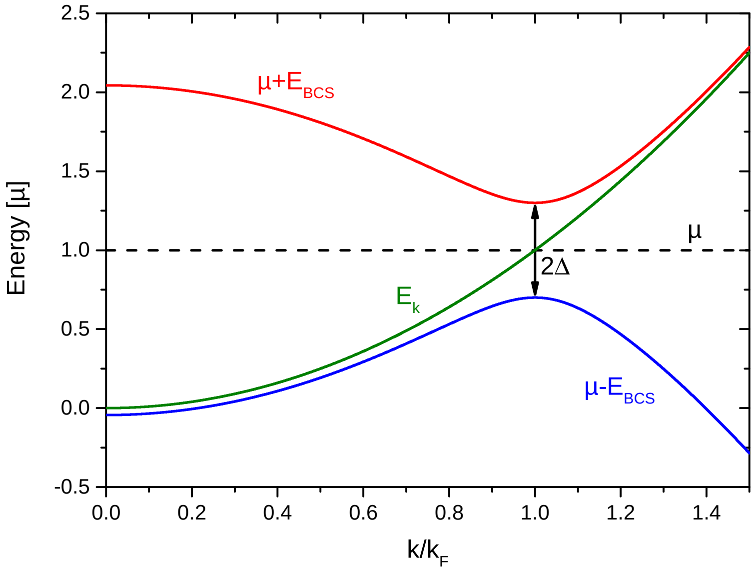

Figure 7.3: Dispersion relations in BCS theory ($\Delta = 0.3E_F$) and for free particles. Shown in green as a reference is the dispersion relation of a free Fermi gas given by $E_k = \frac{k^2}{2m}$. The curves in blue and red give the energy $\pm E_{BCS} = \pm\sqrt{\eta_k^2 + \Delta^2}$, relative to the chemical potential, for removing and adding a single fermion to the system, respectively. The energy gap in BCS theory is given by the minimum energy needed to place an excitation in the system. Thus, it is given by the minimum difference between the lower (blue) dispersion relation and μ. On the other hand, in RF spectroscopy, the removed particle is projected onto a free state and E_{th} is given by the minimum difference between the blue and the green curve, where the latter now corresponds to the final state dispersion relation shifted down by the free-free transition energy.

Consequently, the energy threshold measured in RF spectroscopy becomes temperature dependent. In addition, when decreasing the temperature starting from $T > T^*$, at the onset of pairing the gap changes from zero to a finite value.

A direct problem of the method illustrated here is that, as the onset of pairing is now at a distinct temperature T^* where the gap becomes different from 0, this would imply a second order phase transition rather than the anticipated crossover [Bab98]. The phase transition is however expected to be 'smoothed out' by including quantum fluctuations into the theory.

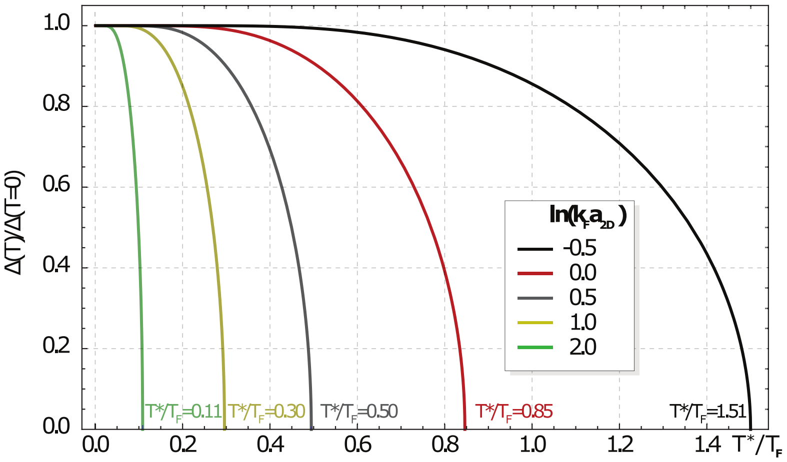

Figure 7.4: Temperature dependence of the gap. The results are obtained by solving the gap equations for different interaction strengths. Assuming that the obtained critical temperature for superfluidity rather marks the onset of pairing, T^* is identified with T_C. Taken from [Vog13].

The mean field results given here describe in principle only the superfluid gapped phase and include the pseudogap predictions presented above only in a very indirect way. In addition, mean field theory is not expected to be accurate in two dimensions. Thus, a good agreement with experimental results is not expected. Nevertheless, especially as the bosonic limit of $E_{th} = E_{dimer}$ is (trivially) covered by mean field theory, it provides at least a suitable reference to compare to.

7.3 System and methods

Prior to presenting experimental results in section 7.4, this section gives an overview over the relevant parameters in our system and the methods applied.

7.3.1 Energy scales

There are several energy scales in our system to be considered. In particular, they are both global and local scales. Global energy scales are parameters of our system and do not vary within the atomic cloud. Most importantly, those scales are thus density independent. In addition there are local, density dependent, scales. For them, the local density approximation is applied, mapping the system locally onto a homogeneous system with the respective local parameters. This is possible as long as all correlation length scales are smaller than the typical variation in trap geometry, which is well given in our system.

The global energy scales are the thermal energy k_BT, set by the temperature of the cloud in thermal equilibrium, and the two-body dimer binding energy E_B[3]. The latter scale is of importance as the gap, at least in mean field theory, directly depends on the binding energy. Going beyond mean field theory, an indirect dependence (via the scattering length setting E_B) should still be given. At least for a molecular gas, pairing is expected as long as $k_BT/E_B \lesssim 1$.
Local energy scales are the local Fermi energy E_F (or equivalently T_F or k_F), given directly by the density, and the interaction energy set by $\ln(k_Fa_{2D})$.
Well above the resonance, one of the scales can be eliminated, as the quasi-2D binding energy approaches the 2D binding energy $E_B = E_Fe^{-2\ln(k_Fa_{2D})}$ (compare figure 2.1). The energy scales can be combined into a relative temperature T/T_F and the interaction scale $\ln(k_Fa_{2D})$ and the $\{T/T_F, \ln(k_Fa_{2D})\}$ phase diagram may be explored. Note however, that the same point in the phase diagram can be reached at different magnetic fields by adapting density and temperature appropriately.

7.3.2 Spatially resolved RF spectroscopy

As explained above, both Fermi temperature and interaction parameter are density dependent and vary within a single realisation as a function of the distance from the cloud centre. In particular, when setting the interaction strength such that in the middle of the cloud, the system is to be considered fermionic and $\ln(k_Fa_{2D}) \gtrsim 0.5$, when probing the outer regions of the cloud, the system changes character and becomes effectively bosonic as $\ln(k_Fa_{2D})$ decreases with decreasing density. In particular, in the outer wings of the cloud, the density is always low enough for the system to be fully described by few-body physics alone. Thus, a two-body bound state exists and is populated as long as $k_BT \lesssim E_B$. Consequently, trap averaged spectra are not well suited to study the onset of pairing and spatially resolved spectra have to be considered. To this end, cloud profiles $n(V)$ are recorded by averaging over equipotential lines V of the cloud with $(n_{RF}(V, \omega))$ and without $(n_{ref}(V))$ applying a (homogeneous) RF pulse with frequency ω. Since both spin states are recorded, the second, not probed, spin state can be used as a reference. These profiles are then compared for different RF frequencies and a two-dimensional response map

$$I(V, \omega) = n_{ref}(V) - n_{RF}(V, \omega) \tag{7.20}$$

is obtained. The V axis may then be translated into different tuples of T/T_F and $\ln(k_Fa_{2D})$.

---

[3] The change in horizontal trapping frequency influencing also E_B is negligible within the extend of the cloud.

7.3.3 Experimental considerations

As a last step, before studying measured data, a few additional remarks on experimental considerations are in order.

Frequency resolution When approaching the BCS regime for large $\ln(k_F a_{2D})$, the pairing pseudogap region is expected to decrease as it has to vanish completely in the BCS limit. Thus, advancing far in the fermionic regime requires a good frequency resolution to be able to resolve small threshold energies. One fundamental limit to the frequency resolution Δf is the time-bandwidth limit, corresponding to the duration of the RF pulse Δt. The limit is dependent on the exact pulse shape, but may be approximated by $\Delta t \cdot \Delta f \approx 0.5$, leading for example to an energy uncertainty of $\Delta E = h \cdot 250\,\mathrm{Hz}$ for a 2 ms pulse typically used for the measurements described in this thesis. The resolution can be improved by using longer pulse durations. This results however automatically in trap averaging as soon as the image duration becomes comparable to (a quarter of) the inverse of the radial trap frequency, that is, already at a few ms. Spatially resolved RF spectroscopy is thus possible only at the cost of a relatively high frequency uncertainty. Giving up spatial sensitivity does not improve the resolution by a large extend, as inhomogeneous broadening caused by a position dependent threshold energy takes over and limits the resolution. Note in addition, that the pulse duration is a major, yet not the only, factor setting the resolutions. Other influences, as for example the pulse power (and thus the Rabi frequency), have to be considered as well.

Temperature and scattering length Temperature is controlled in our system by resonant shaking in z-direction as explained before in section 6.2, in addition to adjusting the final parameters of the evaporative cooling. The scattering length is set as before by adjusting the magnetic offset field.

Thermometry Previously, an estimate of the temperature was obtained by modelling the thermal wings of the cloud in momentum space by a Boltzmann distribution. As the measurements presented here rely more strongly on an accurate temperature determination, and in addition probing the gas in momentum space is due to low particle numbers not always possible, this procedure is extended. As described in [Boe16], the estimate for the temperature is obtained by fitting a set of model equations of state to certain regimes of the cloud profile. To this end, the central region of the cloud is described by a Thomas-Fermi profile and the very low density region by a Boltzmann distribution. In addition, a more elaborate reference equation of state obtained by a virial expansion to second order is used to describe the low density regions. For all these model equation of states, a harmonic trap with the experimentally determined trap frequencies was assumed.

Modelling the spectra The spectra obtained by RF spectroscopy are modelled in the BEC and crossover region by considering equation 7.12, convoluted in addition with a Gaussian to account for all additional broadening mechanisms as well as the finite RF pulse length. In many situations, the observed lineshapes are mostly symmetric around the maximum (at least in some range around it), however, such that the peaks are well modelled by a phenomenological lineshape given by a Gaussian.

7.4 Experimental results

In this section, experimental results on pairing in the normal phase of the strongly interacting quasi-2D Fermi gas are presented. In subsection 7.4.1, the methods to reach the interesting regions of the phase diagram are shown. Thereafter, in subsection 7.4.2, the two limiting regimes of bosonic two-body pairing and mostly unpaired fermions relatively far on the BCS side are discussed. Finally, in subsection 7.4.3, the main results of many-body pairing in the normal phase are presented.

7.4.1 Accessing the phase diagram

In order to access different points in the phase diagram of the local parameters T/T_F and $\ln(k_F a_{2D})$, the radially resolved RF response is measured. Different radial distances from the centre correspond to a different trap potential, different densities and consequently different distinct points in the phase diagram. Thus, for each profile a certain 'path' in the phase diagram is mapped out. This mapping is illustrated in figure 7.5. In addition, by heating, varying the magnetic offset field, or changing the parameters for evaporative cooling, different paths are probed. This is illustrated in figure 7.6. In all the plots, each colour represents one set of parameters, while the different points of one colour correspond to different radii. For an increasing radius away from the central part of the cloud towards the outer wings, the relative temperature T/T_F increases, while $\ln(k_F a_{2D})$ decreases.

First of all, the heating mechanism is considered by resonantly shaking the ODT for a variable length (with otherwise fixed experimental parameters) as explained above. Due to the heating, the temperature is increased and in addition the density is lowered. Thus, the paths are shifted towards lower $\ln(k_F a_{2D})$ and higher T/T_C.

Varying the final trap depth in the evaporation process has a larger effect. As the density is reduced by evaporating further, $\ln(k_F a_{2D})$ is reduced in this way. It is interesting to note that the minimum T/T_F changes only very slightly, indicating that the evaporation efficiency is already relatively low in this regime.

In order to access the whole phase diagram, the magnetic field has to be varied. Most importantly, the offset field determines a_{2D} but, due to the different interaction strengths, also the density is varied. Together, varying the magnetic field changes mostly $\ln(k_F a_{2D})$, while T/T_F is varied most effectively by considering different radii.

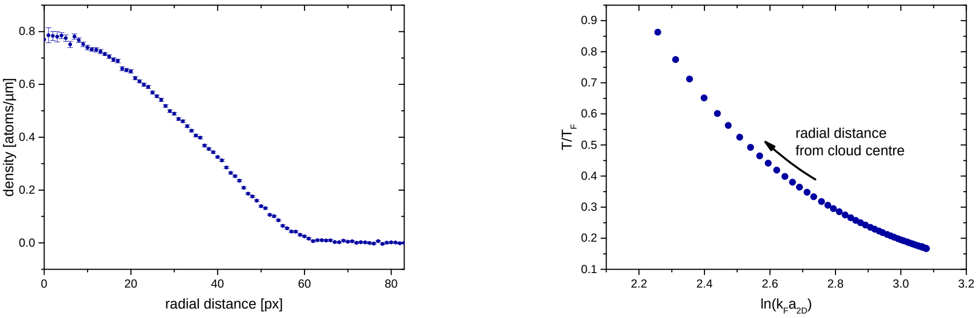

(a) Radial density profile

(b) Local parameters

Figure 7.5: Accessing the phase diagram by locally probing the system. In (a), the radial density profile of an atomic cloud prepared at typical experimental parameters is shown. For each distinct radial distance, the cloud has a certain density. With the global temperature and offset magnetic field, the density translates into a $\{T/T_F, \ln(k_F a_{2D})\}$ tuple as shown in (b). Each data point corresponds to a certain radius. At a constant offset field and temperature, increasing the radius and thus decreasing the density results in a lower $\ln(k_F a_{2D})$ and higher T/T_F.

7.4.2 Limiting regimes

Before studying pairing in the parameter range, where a pseudogap regime is anticipated, the two limiting regimes are considered. First of all, a system at an interaction parameter of $\ln(k_F a_{2D}) \lesssim 0$ is studied. Far in the BEC regime, the threshold energy is fully given by the two-body binding energy and only above $\ln(k_F a_{2D}) \gtrsim 0$ significant deviations are expected. On the other hand, far in the BCS regime, T^* and T_C have to coincide. In addition, due to the finite resolution of the spectroscopy method, already at an earlier point, the pairing energy cannot be resolved anymore. These limits are interesting to study, as they allow to probe the validity of the spectroscopic method and help to understand systematic effects.

BEC limit

As a first example, a sample in the crossover regime at $\ln(k_F a_{2D}) \lesssim 0$ and 670 G, at a temperature of $T = 51\,\mathrm{nK}$ is considered. In this regime, the system is still mostly bosonic and the threshold energy is expected to be mostly given by the two-body bound state $E_{th} = E_B$. The locally resolved RF spectrum is presented in figure 7.7. A strongly asymmetric peak with a threshold energy of around $(10 \pm 1)\,\mathrm{kHz}$ can be seen. The threshold energy is obtained by fits to the model introduced in section 7.3.3 and is compatible with

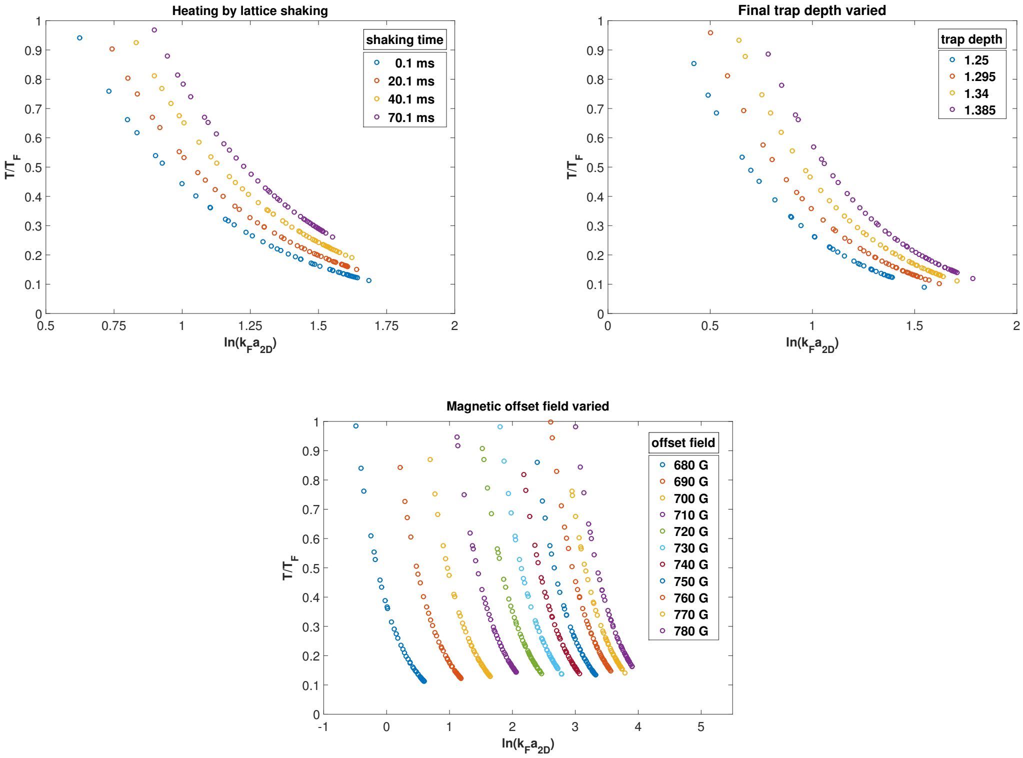

Figure 7.6: In this plot, the experimental methods to access different regimes of the phase diagram are presented. Starting from a cloud at 700 G, a final trap depth in the evaporation process of 1.35 (in arbitrary units) and the lowest possible temperature, these parameters are varied one by another. The different colours indicate different parameter sets, while the different points of each colour correspond to different radii within the cloud. In the first plot, the effect of resonant heating by trap shaking for a variable time is shown. The second plot shows the influence of changing the final evaporation trap depth, while in the third plot, the effect of changing the magnetic offset field is presented. Together, these methods allow for accessing the different regions of the phase diagram.

the two-body dimer energy of 11.1 kHz. The peak position is mostly constant throughout the cloud, while fading out on the outside of the cloud, as also the initial state density fades out. The residual density dependence of the peak position can be attributed to final state interactions, as considered in more detail below. Because the thermal energy is one order of magnitude smaller than the binding energy, no significant population of the free-free peak is expected.

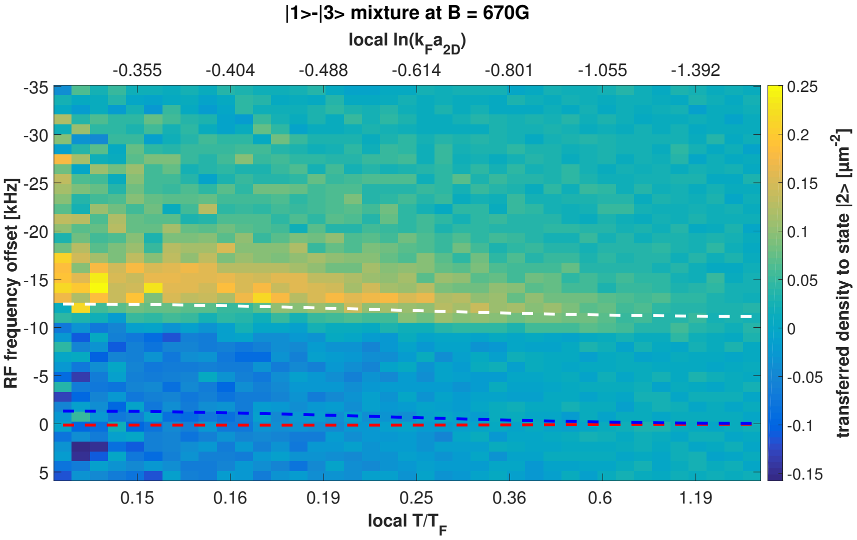

Figure 7.7: Spatially resolved RF spectrum at 670 G. Shown is the transferred density into the previously unoccupied state $|2\rangle$ as calculated by equation 7.20. Each line of the map corresponds to a certain RF frequency offset (relative to the free-free transition), while each column corresponds to a certain radial distance from the cloud centre (in units of the pixel size, i.e. 3.01 µm). Each radius translates to a $\{T/T_F, \ln(k_F a_{2D})\}$ tuple as illustrated above. The peak, with a maximum at around 14 kHz, can be attributed to the bound-free transition ($E_B = h \cdot 11.1\,\mathrm{kHz}$). Indicated in white is the frequency corresponding to the dimer binding energy, including the (small) Hartree (shown in red) and repulsive polaron shift (shown in blue) discussed in more detail below. Note that the temperature is too low to have a significant population of initially free atoms.

Since the observed threshold is mostly constant within the trap, also trap averaged spectra can be taken. In order to be able to introduce significant heating while keeping a good signal, the particle number as well as the RF pulse duration is slightly increased. As a consequence, the interaction parameter in the centre of the cloud is now given by $\ln(k_F a_{2D}) = 0.1$. The resulting spectra are shown in figure 7.8. Depicted is the total remaining atom number in state $|3\rangle$ as a function of the frequency of the applied 4 ms RF pulse. The frequency is again measured relative to the bare $|2\rangle - |3\rangle$ transition. In the left plot, data at a temperature of $T = (33 \pm 3)\,\mathrm{nK}$ are shown. This is significantly above the critical temperature T_C; nevertheless, the gas is almost fully paired as $k_B T/E_B \approx 0.06$. Only for a higher temperature of $(70 \pm 6)\,\mathrm{nK}$, there is some weight in the free-free peak. In addition to the measured data in blue, the spectra are modelled

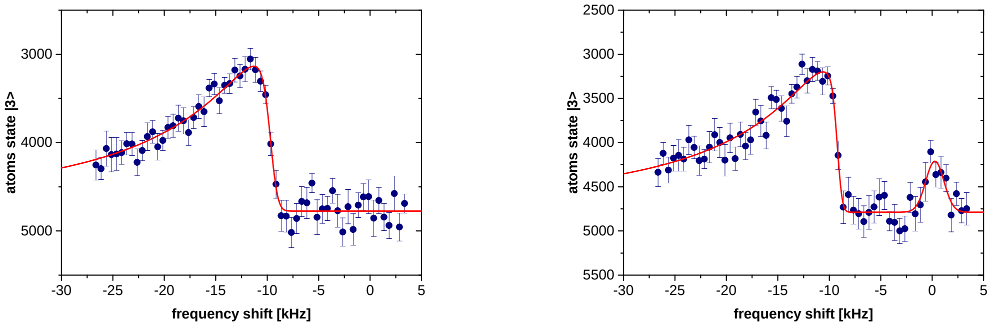

(a) Without heating

(b) With heating

Figure 7.8: Pairing in the crossover regime. Shown are the remaining atoms is state $|3\rangle$ as a function of the applied RF frequency. The frequency is given relative to the bare $|2\rangle - |3\rangle$ transition frequency. Note the inverted axis of the ordinate. At the lower temperature $T = (33 \pm 3)\,\mathrm{nK}$ in (a), (nearly) all atoms are paired up, while there is also significant weight in the free-free peak at the higher temperature $(70 \pm 6)\,\mathrm{nK}$ in (b). The model introduced in section 7.3.3 is fitted to the data to describe the bound-free peak, while a simple Gaussian model is sufficient to describe the free-free peak. The obtained threshold energy is compatible to the two-body dimer binding energy.

by the fit model described in section 7.3.3 for the bound-free and a simple Gaussian lineshape for the free-free peak as shown in red. The fitted model describes the data well.

The above results show that the observed pairing gap, even at slightly positive interaction parameters, can be explained by considering only two-body correlations. The crossover temperature for the onset of pairing remains undetermined here, as it is not possible to reach high enough temperatures in a controlled way.

BCS limit

In addition to the BEC (or more precisely the crossover) regime, also a system more in the BCS limit is studied. To this end, both a system in the $|1\rangle - |3\rangle$ mixture at 740 G and in the $|1\rangle - |2\rangle$ mixture at 930 G is prepared. The initial state interaction parameter of $\ln(k_F a_{2D}) \approx 3$ is in both cases comparable, and the two-body binding energy is with 40 Hz too small to be resolved. Consequently, a single peak at zero offset frequency is anticipated, especially as the bound state is expected to be thermally depleted in any case. For both systems, the spatial response map is shown in figure 7.9. Despite the

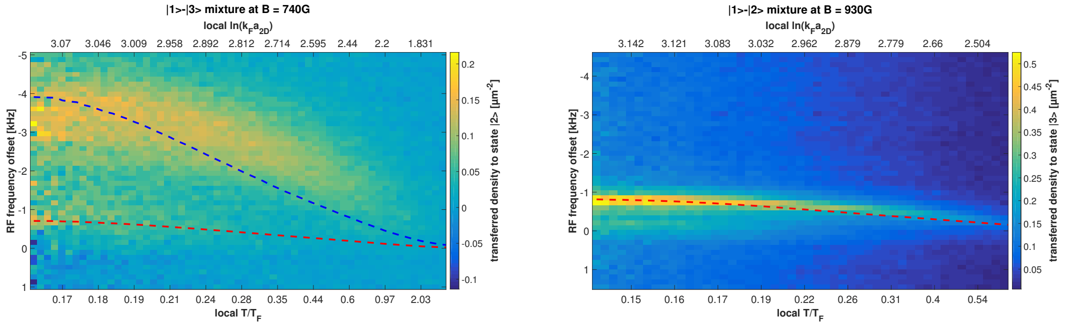

Figure 7.9: Spatially resolved RF spectra in a regime where the two-body binding energy is no longer resolved. Shown is again the transferred density into the final state as a function of the RF frequency and the radial distance from the cloud centre, which in turn also gives the local parameters $\ln(k_F a_{2D})$ and T/T_F. The dimer binding energy is given by $E_B = h \cdot 40\,\mathrm{Hz}$ and a temperature of 71 nK was set. On the left hand side, a spectrum at 740 G in the $|1\rangle - |3\rangle$ mixture is shown. Indicated in red is an initial state Hartree shift and, in blue, in addition a repulsive polaron final state shift. On the right hand side, a spectrum at 930 G in the $|1\rangle - |2\rangle$ mixture is shown. Indicated, again in red, is the Hartree shift.

initial state being comparable, the spectra look quite different. The 670 G data shown previously was taken in the $|1\rangle - |3\rangle$ mixture. This choice was adequate because the final state (2D) interaction effects, quantified by the interaction parameter $\ln(k_F a_{2D})$ in terms of the final state scattering length, are small. On the contrary, at 740 G the interaction parameter is considerably larger ($\ln(k_F a_{2D})$ of ≈ -3 instead of ≈ -10), such that final states have to be taken into account. In addition, also the initial state is, even if unpaired, strongly interacting which is accounted for by including a Hartree shift. In red in figure 7.9, this mean field shift is indicated. It matches well with the small fraction of atoms transferred at an offset frequency of around -1 kHz near the centre of the cloud. In addition, in blue, the repulsive polaron shift, describing final state effects, is drawn on top of the Hartree shift. At least to some approximation, it describes the the centre position of the dominant peak structure. Together, this suggests a picture of initially free, yet strongly interacting, fermions transferred mostly into a final state repulsive polaron, with some small fraction also transferred into a free final state. While it it of course not possible to describe all implications of the final state interactions by the simple polaron model considered here, nevertheless the model provides a measure of the influence of final state interactions compared to the initial-state interactions of interest. As a conclusion for 740 G, the $|1\rangle - |3\rangle$ mixture is not well suited to study initial-state effects.

In the $|1\rangle - |2\rangle$ mixture on the other hand, final state interactions are negligible at 930 G, as the attractive polaron shift is close to zero. Thus, in figure 7.9 the single peak is well described by the free-free transition, if the initial state mean field shift is included.

In this section, the limiting regimes and in addition final state effects where discussed. Both the limit of mostly bosonic pairing and the limit of unpaired fermions are well understood, allowing us to advance further into the strongly correlated fermionic regime. Below, first results in the many-body pairing regime in between the limits are presented. In order to minimise the effect of final state interactions, the regime up to around $\ln(k_F a_{2D}) = 1.5$ is studied in the $|1\rangle - |3\rangle$ mixture, while for larger interaction parameters, the $|1\rangle - |2\rangle$ mixture is employed.

7.4.3 The many-body regime

In the following figure 7.10, spectra in the $|1\rangle - |3\rangle$ mixture for magnetic fields of $B = 690\,\mathrm{G}$ and $B = 700\,\mathrm{G}$ and in the $|1\rangle - |2\rangle$ mixture for $B = 852\,\mathrm{G}$ and $B = 892\,\mathrm{G}$ are displayed. Together, they cover a range between $\ln(k_F a_{2D}) \approx 0.5$ and $\ln(k_F a_{2D}) \approx 2.5$, corresponding to a range of dimer binding energies between $E_B = h \cdot 1.64\,\mathrm{kHz}$ and $E_B = h \cdot 130\,\mathrm{kHz}$. The temperatures in the range of 50 nK to 80 nK are chosen such that it is ensured that the system is not superfluid. Indicated in the spectra are appropriate Hartree and polaron energy shifts in addition to the two-body dimer binding energies. All the specta are taken in a regime where at least in the central region of the cloud, the system has to be considered clearly fermionic, in the sense that the chemical potential is expected to be larger than zero [Lev15]. Nevertheless, on the outside of the cloud, the system always has to approach the few-body limit, since the density approaches zero. Thus, any pairing peak has to approach the dimer binding energy. Whether the bound state is still populated in this limit depends on the temperature (or more precisely the ratio of thermal to binding energy $k_B T/E_B$), however. In all the spectra, a strong and density dependent peak is visible. It can be attributed to the bound-free peak. In addition to the bound-free peak, at least in the middle of the cloud, an additional free-free peak can be seen. In general, the recorded signal, given by the transferred atom density, fades out towards the outside of the cloud as the initial-state density decreases as well. Because the free-free peak has, at the parameters chosen here, in general a smaller weight, its signal decreases below the noise level at an earlier point, explaining its absence in the outer regions of the cloud.

The upper two plots show spectra taken for a system in the $|1\rangle - |3\rangle$ mixture. Indicated in red are the expected mean field shifts of unpaired atoms due to strong interactions in the initial state. In blue, the polaron shift in addition to the Hartree shift is shown. Finally, in white, also the dimer binding energy is added. While above, in figure 7.9, for the BCS limit the polaron shift was able to explain the strongest peak, this is not the case anymore for these spectra. The upper left spectrum corresponds to an offset field of 690 G. It was taken at a temperature of 70 nK and the two-body bound state

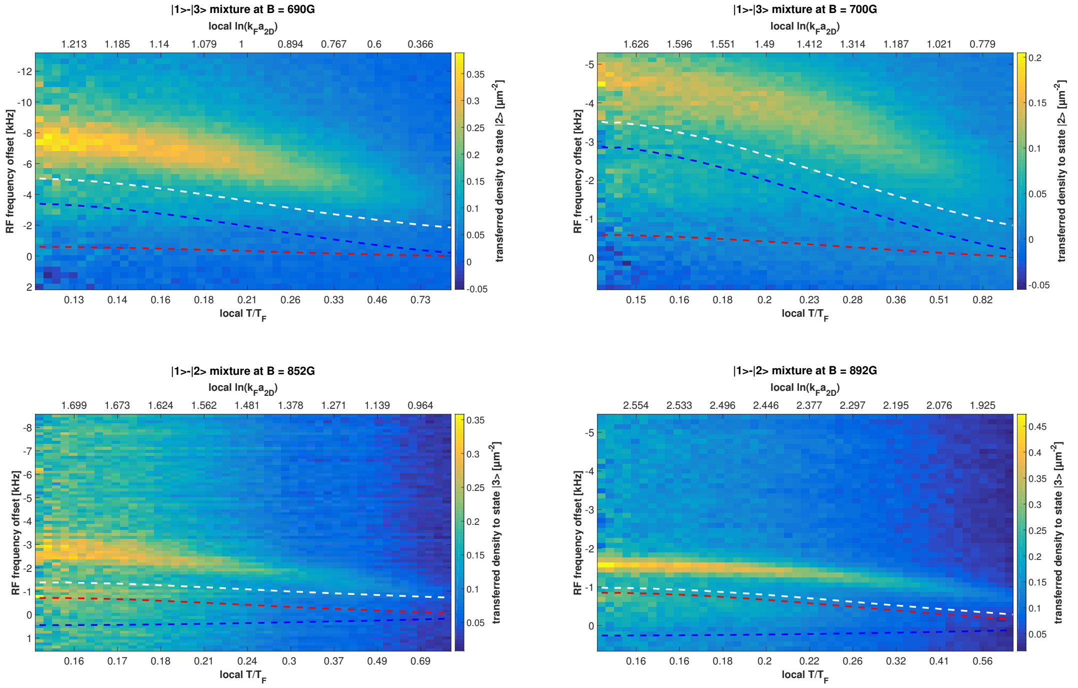

Figure 7.10: Spatially resolved spectra in the many-body regime. In the upper line, spectra in the $|1\rangle - |3\rangle$ mixture at 690 G and 70 nK as well as 700 G and 64 nK are shown. The two-body binding energies are given by $E_B = h \cdot 1.64\,\mathrm{kHz}$ and $E_B = h \cdot 646\,\mathrm{Hz}$, respectively. The red dashed line indicates the initial Hartree shift, for the blue line, the final state repulsive polaron energy is added, and finally for the white line also the shifted dimer energy is considered. In the lower line, spectra in the $|1\rangle - |2\rangle$ mixture at 852 G and 80 nK as well as 892 G and 81 nK, with the two-body binding energies respectively given by $E_B = h \cdot 664\,\mathrm{Hz}$ and $E_B = h \cdot 129\,\mathrm{Hz}$, are shown. The 852 G spectrum corresponds to initial state interactions, comparable to the 700 G spectrum. Again in red the Hartree shift and in blue the Hartree shift in addition to the - now attractive - polaron shift is indicated. In white, the dimer binding energy in addition to the Hartree shift is given.

has an energy of $h \cdot 1.64\,\mathrm{kHz}$. There is some increased signal at the polaron energy corresponding to the blue line, which might indicate a free-free transition, although an unambiguous assignment is not possible. The strong bound-free peak has a maximum slightly above the white line, indicating the shifted two-body binding energy. Assuming the threshold formula of section 7.3.3 to be valid, the obtained E_{th} is however still mostly compatible with two-body pairing. Thus, seen here is pairing clearly above the critical temperature, albeit not significantly exceeding the dimer binding energy. On the one hand, this seems reasonable as the thermal energy is still slightly smaller than the dimer binding energy and in a few-body limit, the dimers would be expected to persist. On the other hand, a $\ln(k_F a_{2D})$ of significantly larger than zero indicates also a pair size larger than the inter-particle spacing, such that additional many-body effects would not be too surprising. However, as should be pointed out again at this point, in the extreme limit of a BCS superfluid, again simply the two-body dimer energy is expected as the threshold frequency.

The above considerations motivate studying also larger interaction parameters. Thus, in figure 7.10, also a spectrum at 700 G, with a dimer binding energy of 600 Hz, is shown. Both a bound-free and a free-free peak can be seen. Here, the blue polaron line describes the free-free peak only very roughly. This is surprising as the model seemed to fit both for weaker (690 G) and stronger (740 G) final state interactions. Taking again the polaron energy as a reference, the observed bound-free threshold energy is still mostly compatible with the dimer binding energy, while when relying on the measured free-free peak as a reference, deviations from the two-body result by around 1 kHz can be noted. In general, the interpretation of this spectrum is hard, as the final state interactions are already the biggest contribution to the observed energy shifts. However, by considering the $|1\rangle - |2\rangle$ mixture instead, final state interactions can be reduced. In particular, the final state 3D scattering length becomes negative and the final state can be described by a weakly bound attractive polaron. The lower two spectra in figure 7.10 are taken in the $|1\rangle - |2\rangle$ mixture. Note that the initial scattering length of the $B = 852$ G system matches the $B = 700$ G one, again supporting a 650 Hz two-body bound state. As before, the Hartree shift is indicated in red, while in blue the Hartree shift in addition to the attractive, and thus positive, polaron frequency shift is indicated. The free-free peak coincides with the initial state mean field shift alone. Thus, it is assumed that there is no significant transfer into the polaronic final state. The white line indicates the two-body binding energy in addition to the Hartree shift. When comparing the spectra at 700 G and 852 G, it is clearly visible that both peaks in the $|1\rangle - |3\rangle$ system are shifted further towards negative offset frequencies compared to the $|1\rangle - |2\rangle$ system. Attributing this to the shift due to the repulsive polaron, rather the frequency difference between the free-free and the bound-free peak should be considered. Comparing similar tuples of $\{T/T_F, \ln(k_F a_{2D})\}$, it is observed that they match within the uncertainty introduced by the fact that it is not possible to compare two exact same tuples of local parameters. It should be pointed out again that the spectrum at 700 G has to be treated with care, as it is not obvious what to take as a reference for unpaired transition frequencies in regions where no free-free peak is visible. Nevertheless, both the spectra at 700 G and 852 G point towards a pairing peak in the normal phase of the gas beyond two-body and mean field physics, in particular, as the thermal energy in both cases is already a factor 2.5 larger than the dimer binding energy, yet slightly smaller than the observed energy 'gap' in the middle of the cloud. This argument is even stronger for the 892 G spectrum, where the two-body dimer energy of around 130 Hz would be barely resolvable[4]. Again, the free-free peak is well described by the Hartree shift alone. Compare to this end again figure 7.9, where the mean field shift was able to describe the only peak. Here, a second bound-free peak clearly above any mean field predictions can be seen.

7.4.4 Conclusions

In the above section, RF spectra for a strongly interacting Fermi gas in the normal phase were shown. In the limiting cases of very strong interactions in the crossover regime and of very small dimer energies more on the BCS side, the system is well described by an effectively bosonic or respectively strongly interacting unpaired fermionic system, as presented above. In addition, in between the limits, deviations from the mean field results for the energy threshold could be observed.

In order to unambiguously map out the pseudogap region and characterise its properties, further analysis has to be done. In particular, up to now no direct statements on the energy (pseudo-)gap could be made as the RF spectroscopy probes the energy gap at zero momentum (see again figure 7.3).

Nevertheless, already with the results presented in this thesis, some preliminary statements can be made. First of all, pairing in the normal phase was shown in a regime which is clearly fermionic, with $\ln(k_F a_{2D}) \gtrsim 1.5$. Compare for this again [Lev15], where it is motivated that a pseudogap regime, without ambiguity, is only expected for $\ln(k_F a_{2D}) \gtrsim 1$[5]. In order to quantify the properties of the pairing observed, a phase diagram where the observed pairing threshold is compared to the two-body binding energy could be drawn. For example, a figure of merit F could be defined by

$$F = \frac{E_{th} - E_{MF}}{E_B}, \tag{7.21}$$

where E_{MF} denotes the mean field Hartree and polaron shifts. For further analyses, the crossover temperature T^* has to be defined in a suitable fashion. Note that for a crossover instead of a phase transition, there will always remain some ambiguity in the definition. In particular, a suitable measure for the existence of pairing has to be found. To this end, it might be instructive to study additional spectra, where some heating is introduced.

In conclusion, the findings presented here provide first promising results and in addition a good basis for further experiments on the quest to understand fermionic many-body pairing.

---

[4] It is nevertheless approached in the few-body limit on the outside of the cloud as expected.

[5] It is stated as well that a temperature of $T/T_F \lesssim 0.2$ has to be reached, which is consistent with the observations made here.

8 Conclusion and outlook

In this thesis, two different methods to probe many-body correlations in a strongly correlated quasi-two-dimensional atomic Fermi gas were explored with their respective applications.

Noise correlation experiments provide a very general method to probe density coherence. It became apparent, however, that an application to two-dimensional dilute systems, as studied in our group, is not directly possible. For neither of the systems considered in this thesis it was possible to unambiguously observe density-density correlations, as all correlations present could be explained by shot to shot variations in the density profile alone. Although the noise correlation experiments presented in this thesis clearly pointed out its limitations, the general method is too promising to be discarded lightly. Most of the interesting low-entropy phases and systems of strongly interacting fermions in a lattice distinguish themselves by many-body density correlations and entanglement. Thus, they could be directly probed by noise correlation measurements. It is important to keep in mind to this end that noise correlations effectively probe the exchange symmetry of the particles.

In particular, it was also possible in this thesis to motivate that, despite all limitations, noise correlation experiments could work after all, assuming some changes to the setup. The noise analysis revealed the presence of atomic noise at least on the order of the imaging noise in an adequate region of interest, and the applicability of noise correlation methods to short time of flight experiments was shown by a direct calculation of the expected correlation signal. Together, this yields the promise of detecting noise correlations with a higher quantum efficiency camera and by improving the optical imaging path in order to reduce parasitic structure on the images.

In addition, in our group a second experiment is concerned with few-body physics (for details, see for example [Mur15a, Bec16]). In this experiment, it is possible to deterministically prepare a few-fermion system in a single or double well. As pointed out before, as of now, spatially resolved imaging with single-atom resolution is possible for a single particle in a single well [Bec16]. However, extending this method to few-body systems and a finite TOF seems feasible [Bec16]. This opens up the possibility to study also the building blocks of correlations in a lattice. For example, in a double well potential, the simple toy model discussed already in chapter 3 can be realised. Even more interestingly, the exchange symmetry of the particles can be changed at will by adapting the interaction strength, and thus, a system with bosonic and fermionic symmetry as well as consisting of distinguishable particles can be prepared and could be probed by noise correlation measurements. Due to the single-atom resolution, effects from imaging noise would be almost eliminated.

In addition to the noise correlation analysis, also a second method to study many-body pair correlations was applied. With the help of RF spectroscopy, fermionic pairing in the normal phase of a strongly interacting Fermi gas was probed. As it was possible to spatially resolve the RF response, the density dependence of the binding energy could be observed and access to distinct points in the $\{\ln(k_F a_{2D}), T/T_F\}$ phase diagram was granted. Because furthermore, strong final state effects could by avoided by exploiting the possibility to choose different initial states, a large range of interactions could be probed. While a detailed determination of the crossover temperature is still subject to ongoing analysis, pairing above the critical temperature in the strongly correlated regime with $\ln(k_F a_{2D})$ up to around 2.5 could be shown. Furthermore, indications of a pairing energy larger than the two-body dimer energy were presented. While the analyses on fermionic many-body pairing are ongoing and not yet completed, already now a preliminary phase diagram can be extracted and is shown in figure 8.1. As a function of the relative temperature T/T_F and the interaction strength $\ln(k_F a_{2D})$, the pairing energy in units of the two-body binding energy, according to equation 7.21, is shown. The threshold energy E_{th} is, as a first approximation, obtained by a Gaussian fit to the bound-free peak, while the mean field energy shift E_{MF} is estimated from the Hartree shift and the repulsive polaron shift (for the data in the $|1\rangle - |3\rangle$ mixture). The difference between threshold energy and mean field shift is normalised to the calculated two-body binding energies. To account for the limited resolution of around $\Delta f = 200\,\text{Hz}$, as soon as $E_B < 2 \cdot \Delta f$, it is normalised rather to twice the resolution instead. The gray circles indicate the probed $\{T/T_F, \ln(k_F a_{2D})\}$ tuples, while in the colour scale, the interpolated results are shown. It can be seen that for low temperatures and $\ln(k_F a_{2D} \approx 2)$, there is a region of the phase diagram where the pairing energy exceeds the dimer energy by a factor of around 3, clearly pointing towards many-body effects. As expected, the relative pairing energy decreases for larger temperatures, approaching the few-body limit of 1. Also, by decreasing the interaction parameter, the same limit of 1 is approached, because also in the BEC limit, the threshold energy is given by the two-body binding energy, $E_{th} = E_B$. It should be noted that the repulsive polaron cannot fully describe the final state interactions, and thus, data extracted in the $|1\rangle - |3\rangle$ mixture (the three data sets with $\ln(k_F a2D) < 1.5$) have to be treated with care. In turn, when approaching the BCS limit, any pseudogap region has to vanish. Furthermore, the pairing energies decrease, such that they are not resolved anymore. Consequently, the relative pairing energy approaches zero for $\ln(k_F a_{2D} \gtrsim 3)$.

The phase diagram comprises the RF spectroscopy results obtained in this thesis, and a clear region of many-body pairing above the critical temperature for superfluidity for strongly interacting fermions can be seen. In possible next steps towards a more detailed understanding of the pseudogap regime, the threshold energy has to be determined more precisely, and the mean field energy shifts have to be included in a more elaborate way.

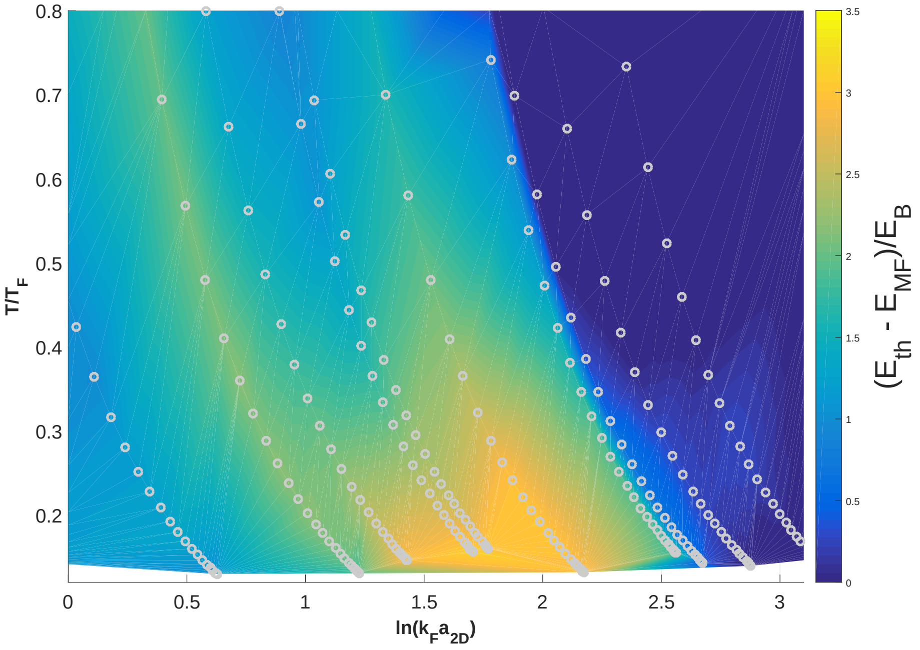

Figure 8.1: Preliminary phase diagram showing the pairing energy of strongly interacting fermions. Shown is the threshold energy E_{th} obtained by a Gaussian fit to the bound-free peak, relative to the mean field energy shifts E_{MF} given by the Hartree and the (repulsive) polaron shift. The energy is normalised to the two-body dimer energy E_B. Indicated in gray are the measured data points, while the colour scale interpolates between the results. Pairing energies significantly larger than the two-body result are obtained in a regime of strong interactions.

Furthermore, a measure for the crossover temperature T^* has to be found and included in the phase diagram.

As pointed out in this thesis, understanding many-body pairing correlations is an important step towards a description of strongly correlated quasi-2D systems. The results presented here, together with ongoing further analyses, could provide valuable insight to this end.

Bibliography

[Alt04] E. Altman, E. Demler, M. D. Lukin, *Probing many-body states of ultracold atoms via noise correlations*, Physical Review A **70**(1), 013603 (2004).

[Alt10] A. Altland, B. D. Simons, *Condensed matter field theory* (Cambridge University Press, 2010).

[And] *CCD Sensor Architecture*, `http://www.andor.com/learning-academy/ccd-sensor-architectures-architectures-commonly-used-for-high-performance-cameras`, accessed: 2016-09-28.

[And95] M. H. Anderson, J. R. Ensher, M. R. Matthews, C. E. Wieman, E. A. Cornell, *Observation of Bose-Einstein Condensation in a Dilute Atomic Vapor*, Science **269**(5221), 198–201 (1995).

[And97] M. R. Andrews, C. G. Townsend, H.-J. Miesner, D. S. Durfee, D. M. Kurn, W. Ketterle, *Observation of Interference Between Two Bose Condensates*, Science **275**(5300), 637–641 (1997).

[Ash76] N. W. Ashcroft, D. N. Mermin, *Solid state physics* (Brooks/Coole Thomson Learning, 1976).

[Bab98] E. Babaev, H. Kleinert, *Crossover from Weak-to Strong-Coupling Superconductivity and to Normal State with Pseudogap*, arXiv preprint cond-mat/9804206 (1998).

[Bar57] J. Bardeen, L. N. Cooper, J. R. Schrieffer, *Microscopic theory of superconductivity*, Physical Review **106**(1), 162 (1957).

[Bau14] M. Bauer, M. M. Parish, T. Enss, *Universal equation of state and pseudogap in the two-dimensional Fermi gas*, Physical review letters **112**(13), 135302 (2014).

[Bay15] L. Bayha, *A Strongly Interacting Fermi Gas in a Two-Dimensional Optical Lattice*, Master thesis, University Heidelberg (2015).

[Bec13] J. H. W. Becher, *A two dimensional optical lattice for ultracold fermions*, Bachelor thesis, University Heidelberg (2013).

[Bec16] J. H. W. Becher, *Towards Spin and Site-Resolved, Single-Atom Imaging of ^{6}Li Atoms in a Multiwell Potential*, Master thesis, University Heidelberg (2016).

[Ber72] V. Berezinskii, *Destruction of long-range order in one-dimensional and two-dimensional systems possessing a continuous symmetry group. ii. quantum systems*, Soviet Journal of Experimental and Theoretical Physics **34**, 610 (1972).

[Blo08] I. Bloch, J. Dalibard, W. Zwerger, *Many-body physics with ultracold gases*, Reviews of Modern Physics **80**(3), 885 (2008).

[Blo12] I. Bloch, J. Dalibard, S. Nascimbene, *Quantum simulations with ultracold quantum gases*, Nature Physics **8**(4), 267–276 (2012).

[Boe16] I. Boettcher, L. Bayha, D. Kedar, P. Murthy, M. Neidig, M. Ries, A. Wenz, G. Zuern, S. Jochim, T. Enss, *Equation of state of ultracold Fermions in the 2D BEC-BCS crossover region*, Physical review letters **116**(4), 045303 (2016).

[Boh12] J. E. Bohn, *Towards an ultracold three-component Fermi Gas in a two-dimensional optical lattice*, Diploma thesis, University Heidelberg (2012).

[Bra95] C. C. Bradley, C. Sackett, J. Tollett, R. G. Hulet, *Evidence of Bose-Einstein condensation in an atomic gas with attractive interactions*, Physical Review Letters **75**(9), 1687 (1995).

[Bro54] R. H. Brown, R. Q. Twiss, *A new type of interferometer for use in radio astronomy*, The London, Edinburgh, and Dublin Philosophical Magazine and Journal of Science **45**(366), 663–682 (1954).

[Bro56a] R. H. Brown, R. Twiss, *The question of correlation between photons in coherent light rays*, Nature **178**(4548), 1447–1448 (1956).

[Bro56b] R. H. Brown, R. Q. Twiss, *Correlation between photons in two coherent beams of light*, Nature **177**(4497), 27–29 (1956).

[Bru09] G. M. Bruun, O. F. Syljuåsen, K. G. L. Pedersen, B. M. Andersen, E. Demler, A. S. Sørensen, *Antiferromagnetic noise correlations in optical lattices*, Physical Review A **80**(3), 033622 (2009).

[Dav95] K. B. Davis, M.-O. Mewes, M. R. Andrews, N. Van Druten, D. Durfee, D. Kurn, W. Ketterle, *Bose-Einstein condensation in a gas of sodium atoms*, Physical review letters **75**(22), 3969 (1995).

[Din96] H. Ding, T. Yokoya, J. Campuzano, T. Takahashi, M. Randeria, M. Norman, T. Mochiku, K. Kadowaki, J. Giapintzakis, *Spectroscopic evidence for a pseudogap in the normal state of underdoped high-Tc superconductors*, Nature **382**, 51–54 (1996).

[Eag69] D. Eagles, *Possible pairing without superconductivity at low carrier concentrations in bulk and thin-film superconducting semiconductors*, Physical Review **186**(2), 456 (1969).

[Fel11] M. Feld, B. Fröhlich, E. Vogt, M. Koschorreck, M. Köhl, *Observation of a pairing pseudogap in a two-dimensional Fermi gas*, Nature **480**(7375), 75–78 (2011).

[Föl05] S. Fölling, F. Gerbier, A. Widera, O. Mandel, T. Gericke, I. Bloch, *Spatial quantum noise interferometry in expanding ultracold atom clouds*, Nature **434**(7032), 481–484 (2005).

[Föl14] S. Fölling, *Quantum noise correlation experiments with ultracold atoms*, Quantum Gas Experiments: Exploring Many-Body States **3**, 145 (2014).

[Foo05] C. J. Foot, *Atomic physics*, Vol. 7 (Oxford University Press, 2005).

[Fox06] M. Fox, *Quantum optics: an introduction*, Vol. 15 (OUP Oxford, 2006).

[Geh03] M. E. Gehm, *Preparation of an Optically-Trapped Degenerate Fermi Gas of ^{6}Li : Finding the Route to Degeneracy*, Dissertation, Duke University (2003).

[Gio08] S. Giorgini, L. P. Pitaevskii, S. Stringari, *Theory of ultracold atomic Fermi gases*, Reviews of Modern Physics **80**(4), 1215 (2008).

[Gre02] M. Greiner, O. Mandel, T. Esslinger, T. W. Hänsch, I. Bloch, *Quantum phase transition from a superfluid to a Mott insulator in a gas of ultracold atoms*, nature **415**(6867), 39–44 (2002).

[Gre03] M. Greiner, C. A. Regal, D. S. Jin, *Emergence of a molecular Bose–Einstein condensate from a Fermi gas*, Nature **426**(6966), 537–540 (2003).

[Gre05] M. Greiner, C. Regal, J. Stewart, D. Jin, *Probing pair-correlated fermionic atoms through correlations in atom shot noise*, Physical review letters **94**(11), 110401 (2005).

[Gri00] R. Grimm, M. Weidemüller, Y. B. Ovchinnikov, *Optical dipole traps for neutral atoms*, Advances in atomic, molecular, and optical physics **42**, 95–170 (2000).

[Had09] Z. Hadzibabic, J. Dalibard, *Two-dimensional Bose fluids: An atomic physics perspective*, in R. Kaiser, D. Wiersma (Ed.), *Nano Optics and Atomics: Transport of Light and Matter Waves* (Enrico Fermi summer school, IOP Press, 2009).

[Her15] I. V. Hertel, C.-P. Schulz, *Atoms, Molecules and Optical Physics 2* (Springer, 2015).

[Heu11] S. Heupts, *A new radio frequency setup to manipulate spin mixtures of fermionic atoms*, Bachelor thesis, University Heidelberg (2011).

[Hof02] W. Hofstetter, J. I. Cirac, P. Zoller, E. Demler, M. Lukin, *High-temperature superfluidity of fermionic atoms in optical lattices*, Physical review letters **89**(22), 220407 (2002).

[Hol14] M. Holten, *Hamiltonian engineering in ultracol atom experiments using a spatial light modulator*, Bachelor thesis, University Heidelberg (2014).

[Hun03] C.-L. Hung, *In situ probing of two-dimensional quantum gases*, Dissertation, University of Chicago (2003).

[Jel07] T. Jeltes, J. M. McNamara, W. Hogervorst, W. Vassen, V. Krachmalnicoff, M. Schellekens, A. Perrin, H. Chang, D. Boiron, A. Aspect, *et al.*, *Comparison of the Hanbury Brown–Twiss effect for bosons and fermions*, Nature **445**(7126), 402–405 (2007).

[Joc03] S. Jochim, M. Bartenstein, A. Altmeyer, G. Hendl, S. Riedl, C. Chin, J. H. Denschlag, R. Grimm, *Bose-Einstein condensation of molecules*, Science **302**(5653), 2101–2103 (2003).

[Ket08] W. Ketterle, M. W. Zwierlein, *Making, probing and understanding ultracold Fermi gases*, in W. K. M. Inguscio, C. Salomon (Ed.), *Ultracold Fermi Gases* (Enrico Fermi summer school, IOP Press, 2008).

[Kos73] J. M. Kosterlitz, D. J. Thouless, *Ordering, metastability and phase transitions in two-dimensional systems*, Journal of Physics C: Solid State Physics **6**(7), 1181 (1973).

[Lan12] C. Langmack, M. Barth, W. Zwerger, E. Braaten, *Clock shift in a strongly interacting two-dimensional Fermi gas*, Physical review letters **108**(6), 060402 (2012).

[Leg80] A. J. Leggett, *Diatomic molecules and Cooper pairs*, in *Modern trends in the theory of condensed matter*, 13–27 (Springer, 1980).

[Lev15] J. Levinsen, M. Parish, *Strongly interacting two-dimensional Fermi gases*, Annual Review of Cold Atoms and Molecules: Volume 3 **3**, 1 (2015).

[Lom08] T. Lompe, *An apparatus for the production of molecular Bose-Einstein condensates*, Diploma thesis, University Heidelberg (2008).

[Mer66] N. D. Mermin, H. Wagner, *Absence of ferromagnetism or antiferromagnetism in one-or two-dimensional isotropic Heisenberg models*, Physical Review Letters **17**(22), 1133 (1966).

[Mur14] P. Murthy, D. Kedar, T. Lompe, M. Neidig, M. Ries, A. Wenz, G. Zürn, S. Jochim, *Matter-wave Fourier optics with a strongly interacting two-dimensional Fermi gas*, Physical Review A **90**(4), 043611 (2014).

[Mur15a] S. Murmann, *Few-particle quantum magnetism with ultracold atoms*, Dissertation, University Heidelberg (2015).

[Mur15b] P. Murthy, I. Boettcher, L. Bayha, M. Holzmann, D. Kedar, M. Neidig, M. Ries, A. Wenz, G. Zürn, S. Jochim, *Observation of the berezinskii-kosterlitz-thouless phase transition in an ultracold fermi gas*, Physical review letters **115**(1), 010401 (2015).

[Nei13] M. Neidig, *A new radio frequency setup to manipulate spin mixtures of fermionic atoms*, Master thesis, University Heidelberg (2013).

[Nga12] V. Ngampruetikorn, J. Levinsen, M. M. Parish, *Repulsive polarons in two-dimensional Fermi gases*, EPL (Europhysics Letters) **98**(3), 30005 (2012).

[Nob] *The Nobel Foundation*, `https://www.nobelprize.org/nobel_prizes/physics/laureates/2001/`, accessed: 2016-08-28.

[Nor11] M. R. Norman, *The Challenge of Unconventional Superconductivity*, Science **332**(6026), 196–200 (2011).

[Pes95] M. Peskin, D. Schroeder, *An introduction to quantum field theory* (1995).

[Pet02] C. J. Pethick, H. Smith, *Bose-Einstein condensation in dilute gases* (Cambridge university press, 2002).

[Pet04] D. Petrov, C. Salomon, G. V. Shlyapnikov, *Weakly bound dimers of fermionic atoms*, Physical review letters **93**(9), 090404 (2004).

[Reg04] C. Regal, M. Greiner, D. S. Jin, *Observation of resonance condensation of fermionic atom pairs*, Physical Review Letters **92**(4), 040403 (2004).

[Rei07] G. Reinaudi, T. Lahaye, Z. Wang, D. Guéry-Odelin, *Strong saturation absorption imaging of dense clouds of ultracold atoms*, Optics letters **32**(21), 3143–3145 (2007).

[Rie10] M. G. Ries, *A magneto-optical trap for the preparation of a three-component Fermi gas in an optical lattice*, Diploma thesis, University Heidelberg (2010).

[Rie15a] M. Ries, A. Wenz, G. Zürn, L. Bayha, I. Boettcher, D. Kedar, P. Murthy, M. Neidig, T. Lompe, S. Jochim, *Observation of pair condensation in the quasi-2D BEC-BCS crossover*, Physical review letters **114**(23), 230401 (2015).

[Rie15b] M. G. Ries, *A Two-Dimensional Fermi Gas in the BEC-BCS Crossover*, Dissertation, University Heidelberg (2015).

[RMP16] R. F. Rosa-Medina Pimentel, *Towards Detection of Noise Correlations in a System of Ultracold* ^{6}*Li Atoms*, Bachelor thesis, University Heidelberg (2016).

[Sak11] J. J. Sakurai, J. Napolitano, *Modern quantum mechanics* (Addison-Wesley, 2011).

[Sal91] B. E. Saleh, M. C. Teich, B. E. Saleh, *Fundamentals of photonics*, Vol. 22 (Wiley New York, 1991).

[Sch12] R. Schmidt, T. Enss, V. Pietilä, E. Demler, *Fermi polarons in two dimensions*, Physical Review A **85**(2), 021602 (2012).

[Sch13] F. Schwabl, *Quantenmechanik* (Springer-Verlag, 2013).

[Ser07] F. Serwane, *The setup of a Magneto Optical Trap for the preparation of a mesoscopic degenerate Fermi gas*, Diploma thesis, University Heidelberg (2007).

[Sim07] P. Simon, *Apparatus for the preparation of ultracold Fermi gases*, Diploma thesis, University Heidelberg (2007).

[Som12] A. T. Sommer, L. W. Cheuk, M. J. Ku, W. S. Bakr, M. W. Zwierlein, *Evolution of fermion pairing from three to two dimensions*, Physical review letters **108**(4), 045302 (2012).

[Ste16] T. Steinle, *Implementation of Simultaneously Imaging two Hyperfine States of Ultracold* ^{6}*Li Atoms in a Magnetic Field*, Bachelor thesis, University Heidelberg (2016).

[Tha00] B. Thaller, *Visual quantum mechanics*, Vol. 1 (Springer Science & Business Media, 2000).

[Vog13] E. Vogt, *Collective modes and polarons in two-dimensional fermi gases*, Dissertation, University of Cambridge (2013).

[Wen13] A. N. Wenz, *From Few to Many: Ultracold Atoms in Reduced Dimensions*, Dissertation, University Heidelberg (2013).

[Wes04] S. Wessel, F. Alet, M. Troyer, G. G. Batrouni, *Quantum Monte Carlo simulations of confined bosonic atoms in optical lattices*, Physical Review A **70**(5), 053615 (2004).

[Wil90] F. Wilczek, *Fractional statistics and anyon superconductivity*, Vol. 5 (World Scientific, 1990).

[Zha12] Y. Zhang, W. Ong, I. Arakelyan, J. Thomas, *Polaron-to-polaron transitions in the radio-frequency spectrum of a quasi-two-dimensional Fermi gas*, Physical review letters **108**(23), 235302 (2012).

[Zür09] G. Zürn, *Realization of an Optical Microtrap for a Highly Degenerate Fermi Gas*, Diploma thesis, University Heidelberg (2009).

[Zür12] G. Zürn, *Few-fermion systems in one dimension*, Dissertation, University Heidelberg (2012).

[Zür13] G. Zürn, T. Lompe, A. N. Wenz, S. Jochim, P. Julienne, J. Hutson, *Precise characterization of Li 6 Feshbach resonances using trap-sideband-resolved RF spectroscopy of weakly bound molecules*, Physical review letters **110**(13), 135301 (2013).

[Zwi03] M. W. Zwierlein, C. A. Stan, C. H. Schunck, S. M. Raupach, S. Gupta, Z. Hadzibabic, W. Ketterle, *Observation of Bose-Einstein condensation of molecules*, Physical review letters **91**(25), 250401 (2003).

[Zwi04] M. Zwierlein, C. Stan, C. Schunck, S. Raupach, A. Kerman, W. Ketterle, *Condensation of pairs of fermionic atoms near a Feshbach resonance*, Physical Review Letters **92**(12), 120403 (2004).

Danksagung

Ich möchte mich herzlich bei allen bedanken, die diese Arbeit möglich gemacht haben und mich während dieses Jahres und auch während des ganzen Studiums unterstützt haben:

- Bei Selim, für die Aufnahme in die Gruppe und die Chance, Teil dieses spannenden Experiments zu sein. Für die tolle Betreuung und Unterstützung das ganze Jahr über.
- Bei der gesamten Ultracold Gruppe, für die fantastische Zeit, spannende Diskussionen, für die Geduld, mir das Experiment und alles drum herum zu erklären, aber auch für unzählige Kicker-Duelle und Pizza/Falafel/Käspätzle Abende.
- Bei allen, die diese Arbeit Korrektur gelesen haben.
- Bei Matthias Weidemüller für die freundliche Übernahme der Zweitkorrektur.
- Bei meiner Familie, meinen Freunden und natürlich Hannah; für alles.

Erklärung

Ich versichere, dass ich diese Arbeit selbstständig verfasst und keine anderen als die angegebenen Quellen und Hilfsmittel benutzt habe.

Heidelberg, den 21.10.2016

....

(Unterschrift)